ANALYSIS OF PAD COMPLIANCE UNDER FRETTING FATIGUE

DANILO RANGEL DE SOUSA RESENDE

MASTERS DISSERTATION
GRADUATE PROGRAM IN MECHANICAL SCIENCES

FACULTY OF TECHNOLOGY

UNIVERSIDADE DE BRASÍLIA

UNIVERSIDADE DE BRASÍLIA
FACULTY OF TECHNOLOGY
GRADUATE PROGRAM IN MECHANICAL SCIENCES

ANALYSIS OF PAD COMPLIANCE UNDER FRETTING FATIGUE

DANILO RANGEL DE SOUSA RESENDE

Advisor: PROF. DR. JOSÉ ALEXANDER ARAÚJO, ENM - PCMEC/UNB

MASTERS DISSERTATION
GRADUATE PROGRAM IN MECHANICAL SCIENCES

PUBLICATION PCMEC.DM - XXX/AAAA
BRASÍLIA-DF, APRIL 12, 2024.

UNIVERSIDADE DE BRASÍLIA
FACULTY OF TECHNOLOGY
GRADUATE PROGRAM IN MECHANICAL SCIENCES

ANALYSIS OF PAD COMPLIANCE UNDER FRETTING FATIGUE

DANILO RANGEL DE SOUSA RESENDE

MASTERS DISSERTATION SUBMITTED TO THE GRADUATE PROGRAM IN MECHANICAL SCIENCES FROM THE FACULTY OF TECHNOLOGY OF THE UNIVERSIDADE DE BRASÍLIA, AS PART OF THE REQUIREMENTS NECESSARY TO OBTAIN THE DEGREE OF MASTER OF SCIENCE IN MECHANICAL SCIENCE.

APPROVED BY:

Prof. Dr. José Alexander Araújo, ENM - PCMEC/UnB
Master's advisor

Prof. Dr. Fabio Comes de Castro, ENM - PCMEC/UnB
Internal Jury

Prof. Dr. Jesús Vázquez Valeo, Universidad de Sevilla
External Jury

BRASÍLIA, APRIL 12, 2024.

CATALOGRAPHIC SHEET
DANILO RANGEL DE SOUSA RESENDE
ANALYSIS OF PAD COMPLIANCE UNDER FRETTING FATIGUE
2024, 109p., 201x297 mm
(PCMEC/FT/UnB, Master of Science in Mechanical Science, Graduate Program in Mechanical Sciences, 2024)
Masters Dissertation - Universidade de Brasília
Faculty of Technology - Graduate Program in Mechanical Sciences

BIBLIOGRAPHIC REFERENCE

DANILO RANGEL DE SOUSA RESENDE (2024) ANALYSIS OF PAD COMPLIANCE UNDER FRETTING FATIGUE. Masters Dissertation in the Graduate Program in Mechanical Sciences, Publication Number xxx/AAAA, Graduate Program in Mechanical Sciences, Universidade de Brasília, Brasília-DF, Brazil, 109p.

RIGHTS SECTION

_____

DANILO RANGEL DE SOUSA RESENDE
danilo.rsr98@gmail.com

Acknowledgments

The academic path is a challenging choice, however, of great reward. I thank all the professors who impacted me during my undergraduate studies in mechanical engineering and my master's degree in mechanical sciences. Especially, I would like to thank Prof. Alex, my advisor since 2019, and Profs. Fabio and Doca who had a great impact during my postgraduate studies at the University of Brasília.

Moreover, the greatest and longest-standing gratitude goes to my parents, João David and Maria, for my incredible raising and unconditional support for all my decisions that brought me to this point of success where I am today. I also thank my aunt Lucia, my sister Victoria, and all my brothers Guilherme, Davi, and Arthur, who are my family and have always supported me in any circumstance. A special thanks to my forever girlfriend, fiancée, and future wife Victoria, who is a blessing in my life and is always by my side.

I dedicate this work to all of them, especially to my brother Guilherme, who passed early but certainly is proud of my journey and watching over me wherever he is. All my friends, those I consider brothers and sisters from other mothers, those who accompanied me during undergraduate studies, and also those who shared with me the day-to-day of the master's degree. Know that I am always grateful for the companionship.

I am a happy guy and all of these is because of you all. Thank you so much.

Danilo, Brasília,
April 12th, 2024.

Abstract

Title: Analysis of pad compliance under fretting fatigue

Fretting fatigue is a contact problem of great importance to the aerospace industry. Along the years, a series of experimental campaigns have been carried out, however, not many of them carried about the deformation from the pad and how it could impact the life estimates. One of the reasons for not much effort being put into the deformation effect is that the well known Cattaneo-Mindlin and subsequent analytical solutions for the contact between two cylinders do not account for lateral deformation of any cylinder. In this study, the pad deformation variation was put into focus by systematically estimating the fretting fatigue lives for different pad overhangs, i.e. the distance between the contact surface and the apparatus that holds the pad. The same variation of pad overhang was carried in experimental tests with Al 7075-T651 alloy. The estimates were taken using finite element analysis and theory of critical distances. They represented well the trend that with the increase of the pad deformation the fretting fatigue life decreases. Estimates with the undeformable analytical solution can significantly over-estimate the lives up to 37%. The proposed methodology for estimating life have shown average errors of less than 18%.

Keywords: Fretting fatigue; life estimation; pad deformation;

Resumo

Título: Análise da deformação da sapata sob fadiga por fretting

A fadiga por fretting é um problema de contato de grande importância para a indústria aeroespacial. Ao longo dos anos, uma série de campanhas experimentais foram realizadas, no entanto, poucas delas se preocuparam com a deformação da sapata e como ela poderia impactar as estimativas de vida. Uma das razões para não se dedicarem muito ao efeito de deformação é que as conhecidas soluções analíticas de Cattaneo-Mindlin e subsequentes para o contato entre dois cilindros não consideram a deformação lateral de nenhum dos cilindros. Neste estudo, a deformação da sapata foi colocada em foco, estimando sistematicamente as vidas totais em fadiga por fretting para diferentes tamanhos de balanço da sapata, ou seja, a distância entre a superfície de contato e o aparato de suporte da sapata. A variação do balanço da sapata foi realizada em testes experimentais com liga de Al 7075-T651. As estimativas foram feitas usando análise de elementos finitos e teoria das distâncias críticas. Elas representaram bem a tendência de que, com o aumento da deformação da sapata, a vida útil de componentes sob fadiga por fretting diminui. As estimativas com a solução analítica indeformável podem superestimar as vidas úteis em até 37%. A metodologia proposta mostrou erros médios menores que 18%.

Palavras-chave: Fadiga por fretting; estimativa de vida; deformação da sapata;

Contents

List of Figures ..... **vii**

List of Tables ..... **x**

List of Abbreviations ..... **xi**

List of Symbols ..... **xii**

1 Introduction **1**

1.1 Context 1

1.2 Motivation 4

1.3 Objectives 4

1.3.1 General objective 4

1.3.2 Specific objectives 5

2 Metal fatigue and fracture mechanics **6**

2.1 Fatigue 6

2.1.1 Stress-life curves $(\boldsymbol{\sigma} - \boldsymbol{N})$ 6

2.1.2 Strain-life curves $(\boldsymbol{\varepsilon} - \boldsymbol{N})$ 7

2.2 Multiaxial fatigue criteria 8

2.2.1 Critical plane approach 9

2.2.2 Smith-Watson-Topper fatigue parameter 10

2.2.3 Theory of Critical Distances 11

2.2.4 Variable critical distance length 14

2.3 Fracture mechanics 16

2.3.1 Stresses in the neighborhood of a crack 16
2.3.2 Crack propagation 18

3 Contact mechanics between cylinders 21
3.1 Superficial stresses 21
3.1.1 Normal loading 22
3.1.2 Tangential loading 23
3.1.3 Remote bulk fatigue load effects 26
3.2 The cyclic stress field within the contact region 28

4 Materials and experimental campaign 30
4.1 Material - 7075-T651 Aluminum alloy 30
4.1.1 Monotonic Properties 31
4.1.2 Fatigue properties 31
4.2 Testing Rig 33
4.3 Experimental campaign 36
4.3.1 Fretting fatigue tests 36
4.4 Microscopic analysis 40
4.4.1 Contact surface measurements 40
4.4.2 Crack and fracture surface measurements 43

5 Stress analysis and life estimate for different pad overhang 45
5.1 Finite Element Method Analysis 46
5.1.1 Fretting fatigue FEM in ABAQUS 46
5.2 Search of critical point 53
5.3 Iterative TCD line method 54
5.3.1 Relation between $\boldsymbol{L}$-$\boldsymbol{N_f}$ 55
5.3.2 Relation between SWT-$\boldsymbol{N_f}$ 56
5.3.3 The line method associated with FEM stresses 56
5.3.4 Iterative algorithm to estimate life 58

6 Results and discussion 60

6.1 Pad deformation 60

6.2 Hotspot Position 62

6.3 Life estimates for different pad overhangs compared to experimental life . . . 64

7 Conclusions 68

7.1 Future works 69

List of Figures

1.1 Fretting scar in a non-lubricated contact (NYE LUBRICANTS, 2023). 1

1.2 Press-fitted shaft fretting scar (LACZKO, 2023). 2

1.3 Aircraft accidents (NTSB, 1989, 2019) 4

2.1 Stress-life (S-N) curves from bending tests of an aluminum alloy. The stress scale is linear, but the number of cycles is plotted on a linear scale (left) and on a logarithmic scale (right). (DOWLING, 2013) 7

2.2 Strain-life curve (ε-N) of RQC-100 Steel. (DOWLING, 2013, p. 749) 8

2.3 Cauchy's tetrahedron. (CASTRO, 2011) 9

2.4 Schematic of the point method at the extreme edge of contact. 12

2.5 Schematic of the line method at the extreme edge of contact. The angle θ is positive clockwise (ERENA GUARDIA et al., 2022) - adapted. 13

2.6 Schematic of the area method at the extreme edge of contact. 14

2.7 Log-log $L - N_f$ curve example for variable critical distance 15

2.8 Crack Propagation modes (DOWLING, 2013) 16

2.9 Crack and $2D$ stress element 16

2.10 (a) Dominance zone of the Stress Intensity Factor. (b) Dimensions for the limitations of LEFM application. (DOWLING, 2013) - Adapted 18

2.11 Crack growth rate as a function of ΔK 19

2.12 Fatigue phases in a circular section test specimen 20

3.1 Contact between two elastically deformable bodies under normal, P, and tangential loading, Q. 22

3.2 Contact slip and stick zones for a partial slip fretting configuration 23

3.3 Superficial pressure and shear stress distribution for a typical loading configuration, $Q/fP = 0.6$, $\sigma_B/fp_0 = 0$. 24
3.4 Tangential loading Q variation with time t (HILLS; NOWELL, 1994) - Adapted . 25
3.5 Variation of surface shear stresses at different moments of cyclic tangential loading. Q/fP ranging from ± 0.6 27
3.6 Effect of the remote bulk fatigue load on the shear stresses shown in Figure 3.5 for σ/p_0 varying between ± 0.6. 28

4.1 Tensile and fatigue test specimen (PINTO, 2022) 31
4.2 $\sigma - \varepsilon$ diagram for Al 7075-T651 (PINTO, 2022) 32
4.3 Stress amplitude vs final lives curves Pinto (2022) 32
4.4 Schematic of the four actuators fretting fatigue rig (ALMEIDA et al., 2022). . . . 34
4.5 Four actuator testing rig high temp apparatus close-up (ALMEIDA et al., 2022). . 35
4.6 Schematic of the Pad and Specimen contact overhang. 36
4.7 Test Specimen and Pad for a fretting fatigue experiment, dimensions on the Appendix. 37
4.8 a) Well aligned and b) mis-aligned contact pressure mark between pad and specimen contact in pressure film (PINTO, 2022). 37
4.9 Example of small resonance on FF test. 39
4.10 Image results from test FF-20-03 39
4.11 Contact surface and points 40
4.12 Line profiles of the contact surface 42
4.13 Crack and fracture surfaces 43
4.14 Example of inclination measurement 44

5.1 Pad overhang schematics for 3 different overhang sizes 45
5.2 Part dimensions and positioning 47
5.3 Step evolution graphic 48
5.4 Interaction viewport from ABAQUS 50
5.5 Load and boundary conditions schematics 50
5.6 a) Global mesh and b) Refined contact mesh 52
5.7 Example of the SWT stresses in the contact surface and hotspot location 54

5.8 Curves of SWT in terms of initiation life for different initiation lengths. (RESENDE, 2023) 55

5.9 TCD line method with FEM schematic 57

5.10 Example of $\sigma_n(t)$ along $2L_G$ when $t = t(Q = Qmax)$ and$\theta = 2°$. 57

5.11 Flowchart of iterative method for fretting fatigue method 59

6.1 a) Pressure distribution over the full contact; b) Close-up of the contact limit . . . 61

6.2 Maximum SWT for each element on the Contact surface 63

6.3 Estimated lives for different pad overhangs 64

List of Tables

3.1 Surface shear stresses for the contact region during the time variation of tangential loading 26

4.1 Chemical composition of Aluminum alloy 7075-T651 (% of mass) 30

4.2 Mechanical properties of the Al 7075-T651 (PINTO, 2022) 31

4.3 Main properties for Al 7075-T651 in the literature 33

4.4 Fretting fatigue Experimental results 38

4.5 Microscopic results from the contact zone 41

5.1 Load application process 51

6.1 Bending moment for different pad overhang lengths 60

6.2 Maximum SWT at surface hotspot 62

6.3 Estimate and experimental lives results 67

List of Abbreviations

Acronyms

Al 7075-T651	Aluminum alloy 7075-T651
CNPq	Conselho Nacional de desenvolvimento científico e tecnológico
FF	Fretting fatigue
FS	Fatemi-Socie fatigue parameter
LEFM	Linear elastic fracture mechanics
NASA	National Aeronautics and Space Administration
NIMS	Japanese National institute of material science
SIF	Stress intensity factor
SWT	Smith-Watson-Topper Fatigue Parameter
TCD	Theory of Critical Distances
TS	Test Specimen
UnB	Universidade de Brasília

List of Symbols

Latin Symbols

a	In fracture mechanics: Crack length	$[mm]$
a	in fretting: Contact semi-width	$[mm]$
B	Fatigue remote Load	$[N$ or $N/mm]$
b	Fatigue strength exponent	-
C	Paris' law coefficient	$[\frac{mm/ciclo}{(MPa\sqrt{m})^m}]$
c	Fatigue ductility exponent	-
c	in fretting: Stick zone semi-width	$[mm]$
D	Diameter	$[mm]$
d	derivative	
$dxdy$	$2D$ element in x and y directions	-
E	Elasticity modulus	$[MPa]$
$E*$	Equivalent Elasticity modulus	$[MPa]$
e	in fretting: Stick zone displacement	$[mm]$
F	Geometric factor	-
f	Friction coefficient	-
$g(x)$	Tangential displacement in relation to x	$[mm]$
h	height	$[mm]$
$h(x)$	Normal interpenetration displacement in relation to x	$[mm]$
L	Critical distance characteristic length	$[\mu m$ or $mm]$
l	length	$[mm]$
K	Stress intensity factor	$[MPa\sqrt{m}]$
K_{Ic}	Fracture toughness	$[MPa\sqrt{m}]$
m	Paris' law exponent	-
$\boldsymbol{n}$	normal direction vector	-
N	Fatigue life cycles	-
P	Normal pressure load	- $[N$ or $N/mm]$
$p(x)$	Surface shear stress distribution	$[MPa]$
p_0	Maximum normal pressure	$[MPa]$

Q	Tangential loading	- [N or N/mm]
$q(x)$	Surface shear stress distribution	[MPa]
R	Loading Ratio	-
$R*$	Equivalent Radius	-
r	Radial coordinate	[mm]
t	time	[s]
$\boldsymbol{t}$	Stress vector	[MPa]
th	thickness	[s]

Greek Symbols

Δ	Range/variation	-
ε	Strain	-
ε'_f	Fatigue ductility coefficient	-
θ	Line inclination/crack orientation or Cauchy's angle	[º]
μ	Rigidity modulus	[MPa]
ν	Poisson's Ratio	-
σ	Stress	[MPa]
$\boldsymbol{\sigma}$	Cauchy's Stress Tensor	[MPa]
σ_u	Ultimate strength	[MPa]
σ_y	Yield Strength	[MPa]
σ'_f	Fatigue ductility coefficient	[MPa]
τ	Shear stress	[MPa]

subscripts

1 e 2	In contact bodies *fretting*
a	Amplitude
B	Remote fatigue stress
eq	Equivalent
f	final or total
G	Guessed value
i	Initiation
I	For mode I
II	For mode II
n	Normal
p	Propagation
pa	Plastic deformation

s	Static
t	Tangential
th	Threshold
xx	Direction x over plane x
yy	Direction y over plane y
xy	Direction x over plane y
∞	Infinite life loading (fatigue limit)

Superscripts

$'$	Adhesion and displacement length for unloading stage
^{est}	Estimated
^{exp}	Experimental

Chapter 1

Introduction

1.1 Context

Fretting is a superficial contact damage that mechanical joints and connections suffer due to small tangential relative displacements (HILLS; NOWELL, 1994). Some examples are riveted and bolted connections, dovetail joints found in jet engines' disk-blade coupling, press-fitted shaft assemblies and energy conductor cables and their anchoring devices. This damage often leads to the nucleation of small cracks close to the edge of the contact surface. When in the presence of a fatigue load, being it due to the centripetal forces of a engine, to the atmospheric pressure difference between land and cruise height or to bending load in a shaft, these small cracks tend to propagate and become what is known as fretting fatigue. Figure 1.1 shows the scar of and non-lubricated contact and Figure 1.2 shows a press-fitted shaft that suffered from fretting due to an irregular contact.

Figure 1.1: Fretting scar in a non-lubricated contact (NYE LUBRICANTS, 2023).

Fretting fatigue is a multiaxial phenomenon and can be divided between initiation and propagation phase, although, recent observations had shown that for high-cycle fatigue ($>10^5$ cycles), the initiation phase comprehends the most of a component life (ERENA GUARDIA et al., 2022). Cheng et al. (1994) used micromechanics to model the initiation phase of the crack but for a quantitative analysis it requires a difficult determination of physical properties. Looking for

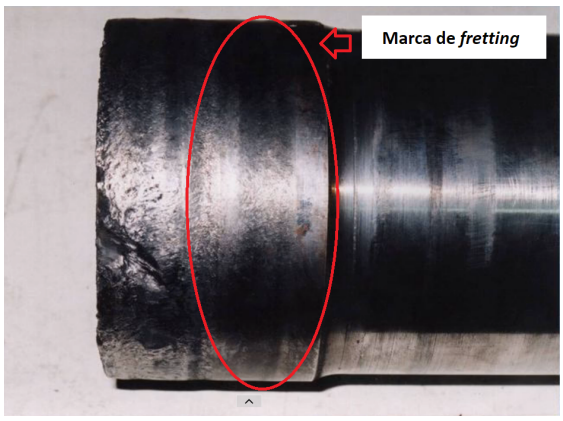

Figure 1.2: Press-fitted shaft fretting scar (LACZKO, 2023).

a simpler approach, Szolwinski and Farris (1996) were capable to evaluate not only initiation life but also the crack direction applying the Smith-Watson-Topper (SWT) fatigue parameter (SMITH; WATSON; TOPPER, 1970), which was first used to analyze multiaxial fatigue by SOCIE (1987), where he implemented a critical plane approach to the parameter, which was created to evaluate the presence of average stress in uniaxial fatigue.

Lamacq, Dubourg, and Vincent (1997), using an aluminum alloy, proposed a theoretical model to predict the inclination angle and the location of the initiation crack in fretting, and subsequently, Lamacq and Baietto (1999) correlated this with the tensile and shear stress fields. Following works, such as Neu, Pape, and Swalla (2000) and Ruiz and Chen (1986), implemented other parameters such as the multiaxial Fatemi-Socie (FS) parameter (FATEMI; SOCIE, 1988), obtaining reasonable results in terms of fatigue life and crack propagation direction.

Models considering a process zone in order to account for the high stress gradient were implemented to fretting, using Theory of Critical Distances (TCD) methodology proposed by Taylor (1999). In these theories the stresses were accounted in a material point, line or area/volume related to a critical distance from the location of maximum stress (or fatigue parameter), the hotspot, as a form to account for fretting high stress gradients (NOWELL; DINI; HILLS, 2006; ARAUJO; NOWELL, 2002). With life estimates within an acceptable range, Araujo and Nowell (2002) tested out two procedures, one taking the average stresses and fatigue parameter along a path that starts from the hotspot with its length related to the critical distance depth from the contact surface, and another taking the averages inside volume with its size related to the critical distance. These two procedures when used in a 2D configuration average the stresses of a line and of an area, respectively. The length of the line and the area radius were determined by the best fit to experimental data. In recent developments, the Modified Wohler Curve Method combined with TCD has been applied to provide fatigue lives, showing good agreement when compared to experimental bases (ARAÚJO; SUSMEL; TAYLOR, et al., 2007). Araújo, Almeida, et al. (2017) calculated the average normal and shear stresses over a line varying in inclination with the contact surface, and this average was applied to critical plane criteria to also examine

crack propagation direction. As novelty, studies were also able to pair the TCD with Artificial Neural Networks (ANN), first for Aeronautical Aluminum alloys (OLIVEIRA; JÚNIOR, et al., 2022; OLIVEIRA; CARDOSO; JÚNIOR; ARAÚJO, 2023) and after applied the Aluminum trained ANN to other materials such as Titanium (OLIVEIRA; CARDOSO; JÚNIOR; DOCA, et al., 2024).

Recent works also have been using the TCD concepts but adding a variable critical distance which is dependent of the life estimate. This process is made via an iterative model. Araújo, Susmel, Pires, et al. (2017), introduced this methodology for fretting and the present author along with Erena Guardia et al. (2022) applied it only for the initiation life and used Extended Finite Element analysis to account for the propagation life.

The present work proposes using this variable critical distance approach with SWT fatigue parameter to evaluate the impact of the pad stiffeness in the fretting fatigue life estimates, in other words, to account for the pad deformation in fretting fatigue. These deformations are accounted by Finite Element Method analysis where different pad overhang distance are applied. Studies from the University of Seville analyses the effect of rolling of the pad on previous test campaigns by measuring fretting scar and implementing a rotation to the FEM analysis (ERENA et al., 2022; VANTADORI et al., 2023). The rolling effect is due to the deformation of the pad and also compliance of the machine device that supports the pad. These effects generate a difference between the fretting fatigue tests and the laterally undeformable fretting fatigue analytical solution, often used as benchmark. This analytical solution was first described by Cattaneo (1938) and Mindlin (1949), for what is know as The Cattaneo-Mindlin problem and after by Hills and Nowell (1994), where they calculated the stresses below the contact surface for cylindrical-plane contact. The differential proposed by the present study is to quantify and validate by means of a controlled experimental campaign the effect of pad compliance. This is done by conducting fretting fatigue tests systematically varying the pad overhang, the distance between the support base and the contact surface, considering at first, the machine support to be sufficiently rigid. Although the overhang length should be minimized, in some test an amount of overhang is needed in order to fit a high temperature device or an optical measurement equipment, both often used in the test carried out at the University of Brasília.

This document comprehends, the Chapters 2 and 3 in which the literature review is given, visiting the main theories of fatigue and fracture mechanics and also the mechanics of cylindrical contact of fretting fatigue, respectively. The Chapter 4 gives a thorough view of the material properties as well as the machinery and specimen pad geometries used to perform the experimental campaign and its results. After that, Chapter 5 presents the methodology applied to analyze the deformation of the pad and Chapter 6 summarizes life estimates comparison with experiments and discuss the results. At last, Chapter 7 summarizes the conclusions plus the suggestions of future work. What follow are the bibliographic References and Appendix area.

1.2 Motivation

Over the years, aircraft and engine manufacturers have been focused in increasing the reliability of life estimates in components under fretting fatigue, such as riveted/bolted connections and blade-disk couplings of jet-engines. Fretting studies date as back as 1950, and fretting fatigue gained attention from the work of Waterhouse (1984). It has been pointed as a possible cause for riveted joint cracks that lead to a fuselage explosive decompression in the Aloha Airlines Flight 243. Another well-known accident is the left engine failure of the Southwest Airlines Flight 1380, in which Metallurgical examinations showed some fretting contact damage (NTSB, 1989, 2019). Each one of these failures (Figure 1.3) resulted in one fatality.

Different factors, as for the rigidity of the material and of the testing rig, the size difference, and the alignment between test specimen and pad, may interfere in the proper study of this phenomenon and result in inconsistent results and component life estimates, hence, a focus must be given to some of the possible geometric variation that each study or researcher may use. In summary, a more precise model to estimate the life of components are a great step to the reliability of this vital industry.

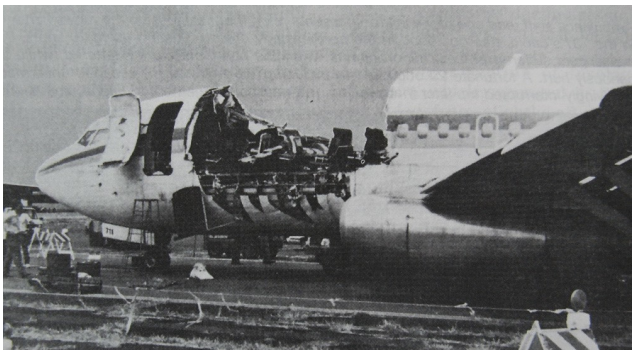

((a)) Aloha Air Flight 243 fuselage

((b)) SWA Flight 1380 Fan Cowl

Figure 1.3: Aircraft accidents (NTSB, 1989, 2019)

1.3 Objectives

1.3.1 General objective

This work has as objective to propose and to validate a hybrid methodology between Finite Element Method (FEM) and the Theory of Critical Distance (TCD) to predict the life of components under fretting fatigue phenomenon based on the Smith-Watson-Topper fatigue parameter. The validation process consist in carrying out a batch of experiments where the rigidity of the fretting contact is systematically changed, by means of the overhang of the pad, distance between the testing rig and the contact.

1.3.2 Specific objectives

The specific objectives are:

- To perform the FEM analysis of an entire cycle of fretting fatigue.
- To extract the stresses from FEM analysis and implement a code to find the superficial hotspot of the method.
- To implement an iterative routine to find the critical distance and to estimate the life of a fretting fatigue analysis.
- To compare different pad overhang stiffness.
- To validate the methodology with experimental data.

Chapter 2

Metal fatigue and fracture mechanics

This chapter is focused on the presentation of the basic theory regarding fatigue and fracture mechanics of metallic materials. Among the topics covered are Fatigue and material Stress-Life curves, the fatigue damage criteria used in the present work, fracture mechanics, and crack propagation.

2.1 Fatigue

Over the years, the fatigue behavior of many materials have been characterized through equations and models. Some of the earliest fatigue studies date back to Wilhelm Albert (1838). Another pioneer was Wohler (1855, 1870), who conducted bending tests on railway axles. Wöhler's method correlated the nominal stress amplitude experienced by a test specimen (TS) with the number of cycles until failure of the component analogous to a railway axle.

For fatigue, experimental data are often taken in uniaxial tests (tension or compression) or bending tests without the application of mean stress, called fully reversed loading tests (Load Ratio, $R = -1$). The presence of mean stress gained more attention around 1970, when Smith, Watson, and Topper (1970) created a relationship capable of assessing the mean stress.

These experimental data can be plotted in the form of stress-life curves or strain-life curves.

2.1.1 Stress-life curves $(\boldsymbol{\sigma - N})$

Basquin (1910) related fatigue data with a linear equation on a logarithmic scale (log-log), and thus defined the following relationship:

$$\sigma_a = \sigma'_f (2N_f)^b \tag{2.1}$$

where σ_a is the stress amplitude, σ'_f and b are, respectively, the fatigue strength coefficient and exponent, and N_f is the fatigue life. The value 2 in the life term exists as a way to account for the number of reversals in non-symmetric loading. Examples of stress-life curves, coincidentally for Al 7075-T6, are given in Figure 2.1. Note that around 10^7 cycles, a sort of plateau is reached. This plateau is common in metallic materials and is called the fatigue limit amplitude, σ_{-1} (typically between 35 to 50% of the ultimate/maximum stress). There are materials that do not reach stabilization, and 10^6 or 10^7 cycles are often defined as the fatigue limit life.

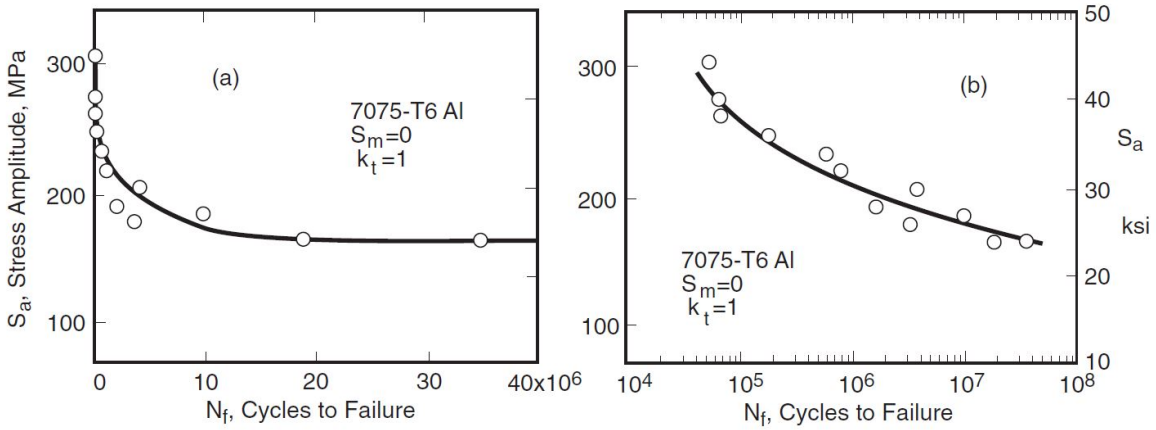

Figure 2.1: Stress-life (S-N) curves from bending tests of an aluminum alloy. The stress scale is linear, but the number of cycles is plotted on a linear scale (left) and on a logarithmic scale (right). (DOWLING, 2013)

2.1.2 Strain-life curves $(\varepsilon - N)$

The strain-based approach is analogous to the stress-based one. However, for determining the strain curve, a plastic component, ε_{pa}, is considered in addition to an elastic one, ε_{ea} (DOWLING, 2013). This plastic component is determined by measuring the half-width of a mean cycle of stress-strain hysteresis. Thus, we have the strain amplitude, ε_a, as:

$$\varepsilon_a = \varepsilon_{ea} + \varepsilon_{pa} \tag{2.2}$$

where:

$$\varepsilon_{ea} = \frac{\sigma_a}{E} = \frac{\sigma'_f}{E}(2N_f)^b \qquad \text{e} \qquad \varepsilon_{pa} = \varepsilon'_f(2N_f)^c \tag{2.3}$$

This way, combining the elastic and plastic components we have:

$$\varepsilon_a = \frac{\sigma'_f}{E}(2N_f)^b + \varepsilon'_f(2N_f)^c \tag{2.4}$$

where we introduce the new material properties ε'_f and c, respectively, as the coefficient and exponent of fatigue ductility. This equation is well regarded as the Basquin-Coffin-Mason

Equation.

Figure 2.2 provides an example of a strain-life curve for RQC-100 steel. Note that the data points are plotted for elastic, plastic, and total strain.

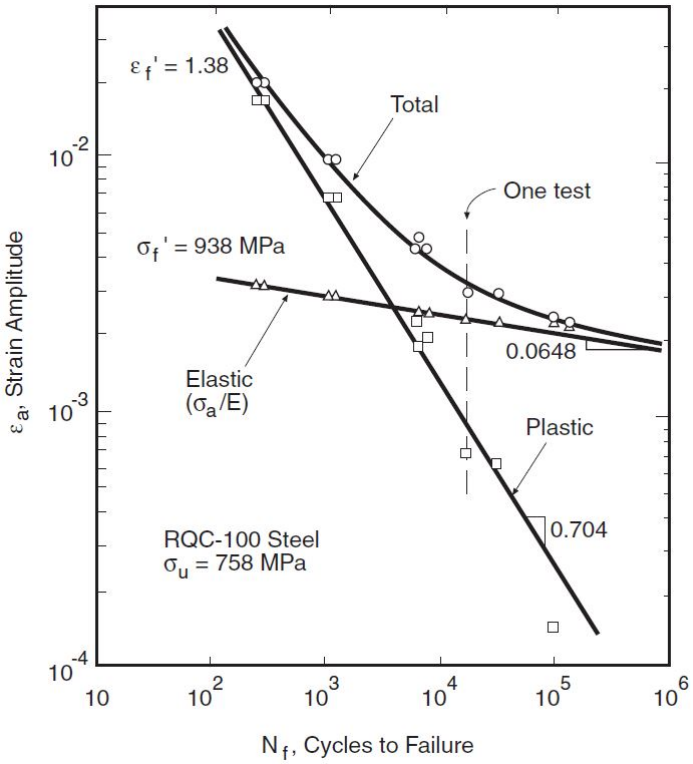

Figure 2.2: Strain-life curve (ε-N) of RQC-100 Steel. (DOWLING, 2013, p. 749)

2.2 Multiaxial fatigue criteria

Multiaxial fatigue criteria are used to assess the damage that a component is subjected to when the loading is multidirectional. A commonly used way to estimate the damage on such components is the critical plane approach, in which plane directions for crack nucleation and propagation are searched in the material critical stress point (the one with maximum stresses). Over the years, many studies have been created and adapted to consider high stress gradient problems, such as notched test specimens and contact problems such as fretting fatigue. For this purpose, several of them were based on Taylor (1999, 2008), where he presents the Theory of Critical Distances (TCD). In addition to TCD, this chapter also focused on the use of the Smith-Watson-Topper (SWT) fatigue damage parameter for determining the critical plane. Other fatigue damage parameters have been applied to estimate fretting fatigue lives, such as Fatemi-Socie parameter, Modified Wohler-Curve Method, Crossland, but SWT parameter have often shown the better results (BOHÓRQUEZ et al., 2019; ERENA GUARDIA et al., 2022).

2.2.1 Critical plane approach

To find the critical plane in a infinitesimal material point it is used what is called the Cauchy's tetrahedron. Figure 2.3 show how the tetrahedron looks like. The tetrahedron is formed by the plane we are interested and the Cartesian axis, and any plane can be defined by the unit vector direction $\boldsymbol{n}$, which is normal to such plane.

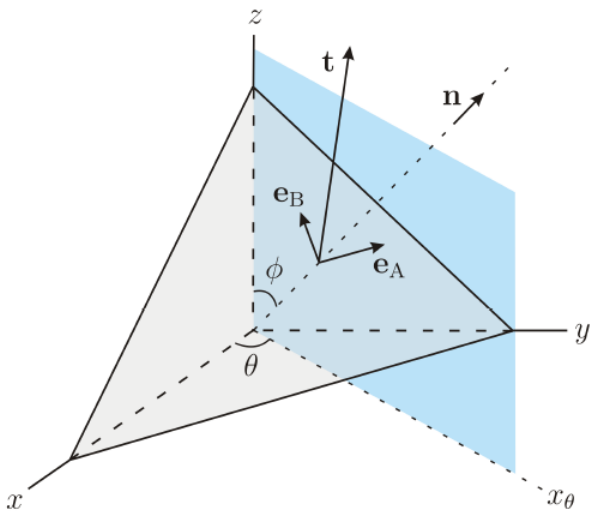

Figure 2.3: Cauchy's tetrahedron. (CASTRO, 2011)

From the $\boldsymbol{n}$ vector it can be defined the stress vector $\boldsymbol{t}$ from a multiplication with the Cauchy's stress tensor $\boldsymbol{\sigma}$:

$$\boldsymbol{t} = \boldsymbol{\sigma n} \tag{2.5}$$

Figure 2.3 also introduces the basis $(\boldsymbol{n}, \boldsymbol{e_A}, \boldsymbol{e_B})$. The vector $\boldsymbol{e_A}, \boldsymbol{e_B}$ are defined respectively as:

- $\boldsymbol{e_A}$ is the unit vector parallel to the plane xy.
- $\boldsymbol{e_B}$ is the unit vector that point to the z axis.

and these vectors are defined in function of the angles θ and ϕ, which are the angle between plane xz and the plane that passes through $\boldsymbol{n}$ and the angle between axis z and $\boldsymbol{n}$ itself, respectively. The basis vectors can be described in function of the angles as:

$$\boldsymbol{n} = \begin{pmatrix} \sin\phi\cos\theta \\ \sin\phi\sin\theta \\ \cos\phi \end{pmatrix} \;;\; \boldsymbol{e_A} = \begin{pmatrix} -\sin\theta \\ \cos\theta \\ 0 \end{pmatrix} \;;\; \boldsymbol{e_B} = \begin{pmatrix} -\cos\phi\cos\theta \\ -\cos\phi\sin\theta \\ \sin\phi \end{pmatrix} \tag{2.6}$$

With all that, it is possible to describe normal and shear stresses on any plane of a material point applying the following equations:

Normal stress:

$$\sigma_n = \boldsymbol{\sigma n} \cdot \boldsymbol{n} = \boldsymbol{t} \cdot \boldsymbol{n} \tag{2.7}$$

Shear stress:

$$\boldsymbol{\tau} = \tau_A \boldsymbol{e_B} + \tau_b \boldsymbol{e_A} \ , \ \text{where:} \tag{2.8}$$

$$\tau_A = \boldsymbol{\sigma n} \cdot \boldsymbol{e_A} \text{ and } \tau_B = \boldsymbol{\sigma n} \cdot \boldsymbol{e_B}$$

Moreover, fatigue parameters based on shear stress or normal stress can be formulated. In the present work only the Smith-Watson-Topper parameter is described. In previous work from the author, SWT showed better results when compared to others (ERENA GUARDIA et al., 2022; RESENDE, 2023).

2.2.2 Smith-Watson-Topper fatigue parameter

The Smith-Watson-Topper (SWT) criterion (SMITH; WATSON; TOPPER, 1970) was originally developed as a fatigue damage parameter that considered mean stress for uniaxial loading. Subsequently, SOCIE (1987) proposed the extension of the SWT parameter for multiaxial critical plane analysis. The original equation for SWT parameter is:

$$SWT = \max_{\theta} \left\{ \sqrt{\sigma_{n,max}(\theta,\phi)\sigma_{n,a}(\theta,\phi)} \right\} \tag{2.9}$$

Inside a linear-elastic regime, the form of the SWT parameter used for a 2D strain-based approach is expressed by Eq. 2.10 (DOWLING, 2013). This equation is the ideal form to use along with Basquin-Coffin-Mason Equation.

$$SWT = \max_{\theta} \left\{ \sigma_{n,max}(\theta)\varepsilon_{n,a}(\theta) \right\} = \max_{\theta} \left\{ \sigma_{n,max}(\theta) \frac{\sigma_{n,a}(\theta)}{E} \right\} \tag{2.10}$$

where $\varepsilon_{n,a}$ is the amplitude of normal strain, $\sigma_{n,max}$ is the maximum normal stress, and $\sigma_{n,a}$ is the amplitude of normal stress in the loading cycle for each orientation θ in a 2D problem. In a 3D problem, it is required to account σ_n as well for ϕ as regarded in the Cauchy's tetrahedron. Thus, $\sigma_n = f(\theta, \phi)$.

According to Chu (1995), the correct procedure for determining the critical plane is by calculating the plane where the SWT parameter from Eq. 2.10 is maximum, as it indicates that both mean and maximum stresses combined represent the greatest damage to the component.

2.2.3 Theory of Critical Distances

According to Araújo, Almeida, et al. (2017), critical plane techniques were developed based on the propagation behavior under uniform stress/strain conditions. In this type of stress field, the classical method for determining crack initiation orientation and life is to search for the critical plane at the singular material point in which the equivalent stress or stress parameter is maximum, here called hotspot. Unfortunately, for mechanical problems under high stress gradients, such as the cylinder-plane contact problem under partial slip conditions, the location of the material point at which to calculate is not evident.

Therefore, in this work, Theory of Critical Distances (TAYLOR, 1999, 2008) was considered to estimate the lives and crack initiation orientation under fretting conditions. The theory of critical distance was proposed to unify multiaxial fatigue methodology for notched or cracked specimens and was later applied by other researchers to fretting contact problem (ARAÚJO; SUSMEL; TAYLOR, et al., 2007; ARAÚJO; ALMEIDA, et al., 2017; ERENA GUARDIA et al., 2022; OLIVEIRA; CARDOSO; JÚNIOR; ARAÚJO, 2023). The Critical distance length is material dependent and has the goal to determine an area of influence around the most critical point in which the stress should be considered to determine fatigue life. This can be made by calculating the stress on another material point, by averaging the stress or fatigue parameters along a line or averaging the stress inside a region (area or volume). In this work, respectively, are presented the following methods applied to 2D cylindrical-plane fretting: Material Point Method, Line Method and Area Method.

2.2.3.1 Material Point Method

The Material Point Method is the most simple critical distance method, as it only requires to calculate the equivalent stress or the stress parameter at another point within a certain distance from the called hotspot. Figure 2.4 show the schematic for the method. The material point in fretting is often calculated perpendicular to the contact surface at a distance $L/2$, but some applications can require it to be variable. The angle θ concerns the angle of the critical plane in a straight forward critical plane approach.

To apply the SWT parameter it is required to take the history of the normal stress, σ_n, for each angle θ at the Material point, as equations:

$$\sigma_{n,max}(\theta) = \max_t(\sigma_n(\theta, t) \tag{2.11}$$

$$\sigma_{n,a}(\theta) = \frac{1}{2}[\max_t(\sigma_n(\theta, t) - \min_t(\sigma_n(\theta, t)] \tag{2.12}$$

respectively for maximum normal stress and for normal stress amplitude.

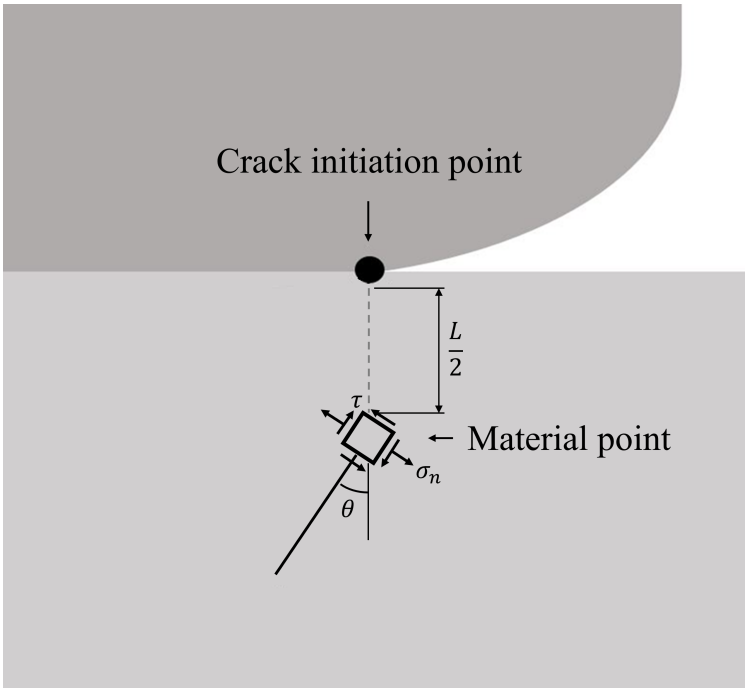

Figure 2.4: Schematic of the point method at the extreme edge of contact.

To apply this in a 3D context no complicated task is needed to consider the other spherical coordinate ϕ to the critical plane calculation.

2.2.3.2 Line Method

The line method is a method that the critical plane has one of its physical dimensions finite, unlike the concept of a point that considers planes of infinitesimal dimensions. Hence, for the fretting cylinder-plane problem, the critical plane is defined by a line, and its inclination indicates the crack initiation direction. The influence of stress is considered by taking their averages along the line.

To implement the method, the line with a characteristic length $2L$ and orientation θ starts at the crack initiation point, the hotspot, as shown in Figure 2.5. Thus, the averaged normal stress along the line is expressed by Eq. 2.13, where $\sigma_n(r, \theta, t)$ is the normal stress component at each time instant t. The r radial coordinate represents the position along the line.

$$\bar{\sigma_n}(\theta, t) = \frac{1}{2L} \int_0^{2L} \sigma_n(r, \theta, t) dr \tag{2.13}$$

In addition to this, the stresses need to be computed in the SWT parameter. Hence, the averages for the maximum normal stress and the normal stress amplitude, with respect to the line, are determined by the following equations, respectively (note the bar notation to indicate the average value).

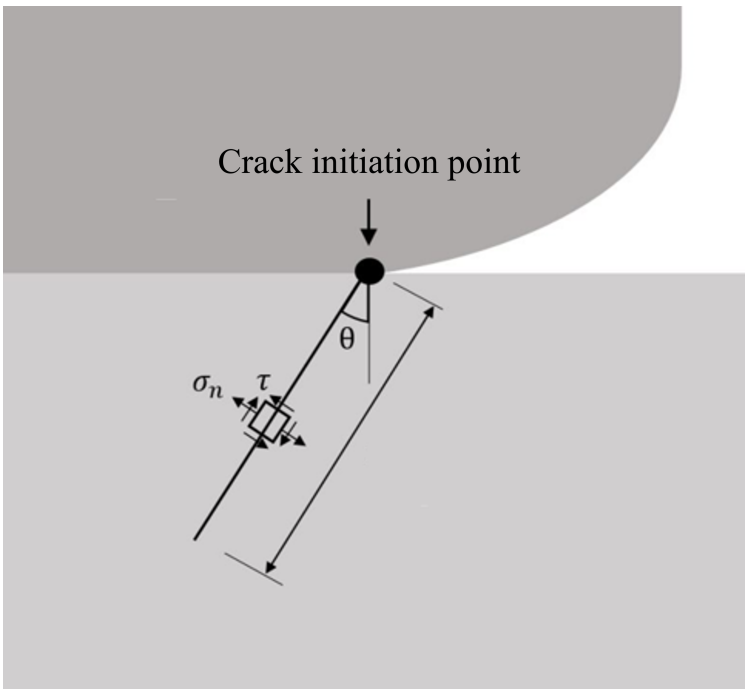

Figure 2.5: Schematic of the line method at the extreme edge of contact. The angle θ is positive clockwise (ERENA GUARDIA et al., 2022) - adapted.

$$\bar{\sigma}_{n,max}(\theta) = \max_t(\bar{\sigma_n}(\theta, t)) \tag{2.14}$$

$$\bar{\sigma}_{n,a}(\theta) = \frac{1}{2}\left[\max_t\left(\bar{\sigma}_n(\theta, t)\right) - \min_t\left(\bar{\sigma}_n(\theta, t)\right)\right] \tag{2.15}$$

It is worth noting that applying this methodology to a 3D context only requires to add ϕ angle, varying the line direction inwards or outwards the image plane ("paper plane").

2.2.3.3 Area Method

Last of all is the Area method for 2D applications or Volume method for a 3D one. This consist in considering a semi-circumference (or a semi-sphere) of interest to account the averaged stresses. The center of the area is the fretting hotspot, located in the other edge of the contact and the radius of this area may differ, from $1L$ to $1.54L$ (TAYLOR, 1999; SUSMEL, 2008; AL ZAMZAMI et al., 2020). The schematic of the area method is shown in Figure 2.6 for 2D fretting contact.

To average the stresses the equation is the following

$$\bar{\sigma_r}(t) = \frac{4}{\pi L^2}\int_0^{\pi/2}\int_0^L \sigma(r, \theta, t)\, r \quad dr d\theta \tag{2.16}$$

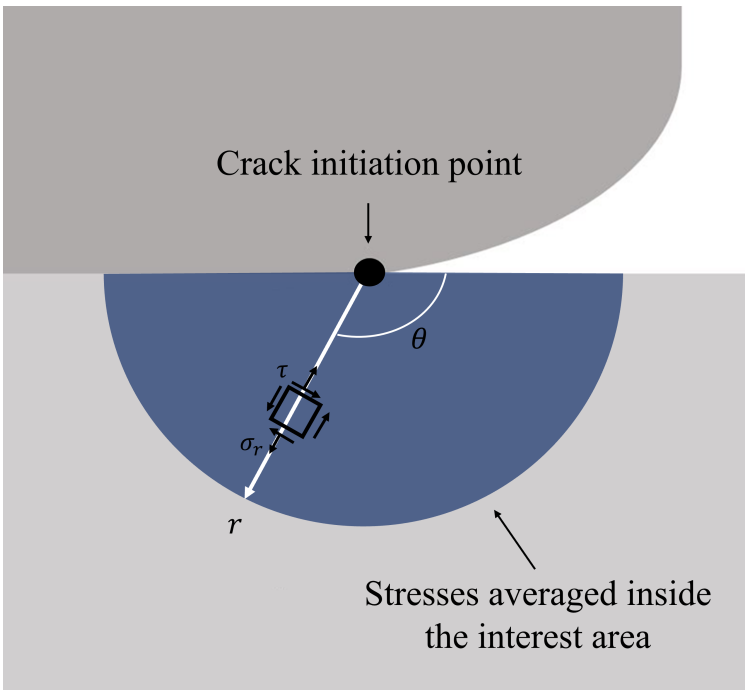

Figure 2.6: Schematic of the area method at the extreme edge of contact.

In a 3D configuration it is needed to account for a new integral around the coordinate ϕ. This method is a more complex approach and the amount of work required not always returns better estimates and a determination of the crack initiation direction is not straightforward. An example of this approach being used is in the case of residual stress due to indentation (GOMES et al., 2023).

For applying the SWT parameter the average stress is taken analogous to the line method, but instead of normal stress, radial stress:

$$\bar{\sigma}_{r,max} = \max_t(\bar{\sigma}_r(t)) \tag{2.17}$$

$$\bar{\sigma}_{r,a} = \frac{1}{2}\left[\max_t\left(\bar{\sigma}_r(t)\right) - \min_t\left(\bar{\sigma}_r(t)\right)\right] \tag{2.18}$$

2.2.4 Variable critical distance length

Throughout the years, several authors tried to fix the critical distance L often estimating its value by experimental fitting the best corresponding value (TAYLOR, 1999; ARAUJO; NOWELL, 2002; SUSMEL; LAZZARIN, 2002; ARAÚJO; SUSMEL; TAYLOR, et al., 2007). More recently, Araújo, Almeida, et al. (2017) came with the idea of having a critical distance L that varies with estimated life in fretting. This approach have been showing good results ever since (ARAÚJO; CASTRO, et al., 2020; ERENA GUARDIA et al., 2022; PINTO et al., 2023).

This critical distance can be determined by fitting a line L-N on a logarithmic scale (log-log), as shown in Figure 2.7, where the static and fatigue limit lives characteristic lengths, L_s and L_∞, are given by Eqs. 2.19 and 2.20, respectively:

$$L_s = \frac{1}{\pi}\left(\frac{K_{Ic}}{\sigma_u}\right)^2 \tag{2.19}$$

$$L_\infty = \frac{1}{\pi}\left(\frac{\Delta K_{th}}{\Delta\sigma_{-1}}\right)^2 \tag{2.20}$$

where K_{Ic} is the material fracture toughness in mode **I**, σ_u is the ultimate tensile strength, ΔK_{th} is the threshold stress intensity factor for fully reversed loading also in mode **I**, and $\Delta\sigma_{-1}$ is the range of uniaxial fatigue limit also with $R = -1$, determined for the fatigue limit life N_∞. Different Loading ratios require that the properties used in Eq. 2.20 to be for the same loading ratio.

Another way to estimate the $L - N_f$ curve is to calibrate it from the fracture toughness test for differently notched specimens.

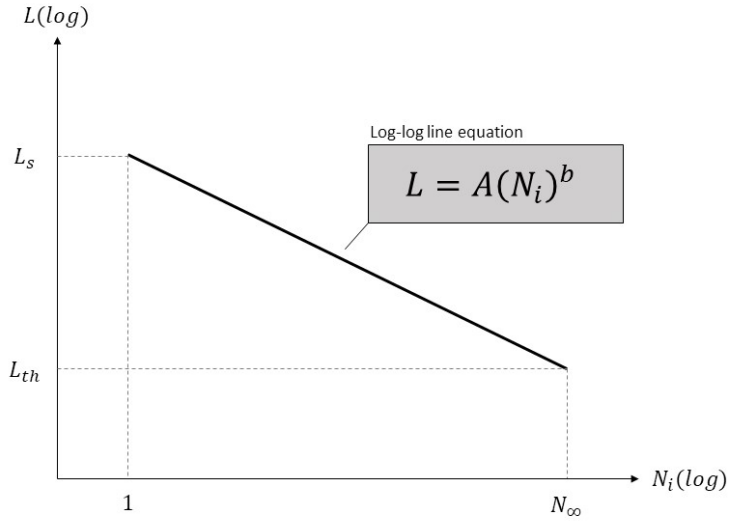

Figure 2.7: Log-log $L - N_f$ curve example for variable critical distance

2.3 Fracture mechanics

The fracture of metallic materials due to cyclic loading is known as the leading cause of failure in mechanical components, referred to as fatigue. The literature divides material fatigue into 3 phases: 1) crack initiation; 2) crack propagation; and 3) complete rupture of the component (catastrophic failure). Fracture mechanics involves the study of these latter two phases.

2.3.1 Stresses in the neighborhood of a crack

The stress field near the crack tip is important for assessing the intensity of the stress that stimulates crack propagation. Three crack propagation modes have been conventionally defined: Modes I, II, and III, referred to as opening mode, sliding mode, and tearing mode, respectively. Figure 2.8 illustrates the crack propagation modes.

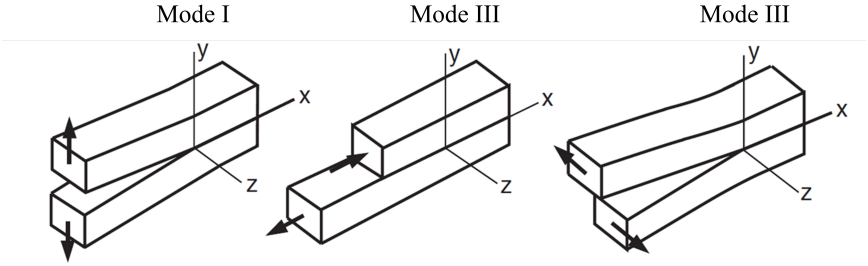

Figure 2.8: Crack Propagation modes (DOWLING, 2013)

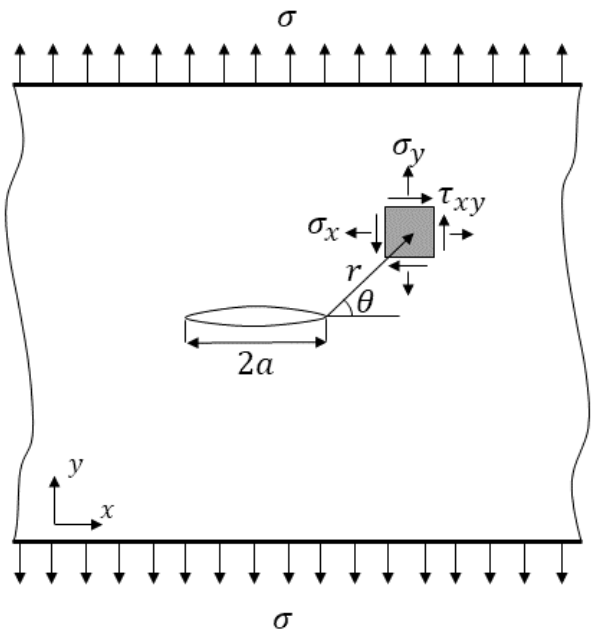

Figure 2.9: Crack and $2D$ stress element

To evaluate the stress near the crack, consider a crack of length $2a$ in an infinite plane subjected to a stress σ inducing propagation due to Mode I, as shown in Figure 2.9. For an element $dxdy$

at a distance r and inclination θ from one end of the crack, it is possible to calculate the stresses using the theory of Linear Elastic Fracture Mechanics (LEFM) (DOWLING, 2013):

$$\begin{aligned}
\sigma_{xx} &= \frac{\sigma\sqrt{\pi a}}{\sqrt{2\pi r}} cos\frac{\theta}{2}\left(1 - sin\frac{\theta}{2}sin\frac{3\theta}{2}\right) + \cdots \\
\sigma_{yy} &= \frac{\sigma\sqrt{\pi a}}{\sqrt{2\pi r}} cos\frac{\theta}{2}\left(1 + sin\frac{\theta}{2}sin\frac{3\theta}{2}\right) + \cdots \\
\tau_{xy} &= \frac{\sigma\sqrt{\pi a}}{\sqrt{2\pi r}} sin\frac{\theta}{2}cos\frac{\theta}{2}cos\frac{3\theta}{2} + \cdots
\end{aligned} \tag{2.21}$$

where Eqs. 2.21 are the first terms of an expansion series valid only if $r \gg a$.

Note that the stresses given by Eqs. 2.21 tend towards infinity ($\sigma_{xx}, \sigma_{yy}, \tau_{xy} \to \infty$) as $r \to 0$. All of these stresses contain two common terms, one from the geometric position:

$$\frac{1}{\sqrt{2\pi r}} f(\theta) \tag{2.22}$$

and another:

$$\sigma\sqrt{\pi a} \tag{2.23}$$

called stress intensity factor, in this case for mode I, K_I.

The stress intensity factor defines the magnitude of stresses near the crack tip. However, this K has constraints:

- K has a dominance region that requires the distance to be much larger than the crack semi-length $r \gg a$. This is because K is determined using only the first term of the series expansion.
- K should generally be applied for cases where the yield regime is small. It is restricted by the plastic zone because this zone must be much smaller than the dominance region of K.

Such restrictions can be visualized in Figure 2.10 and are necessary for the application of calculations based on LEFM. A K value calculated beyond its LEFM applicability zone underestimates the severity of the crack.

Numerically, according to Dowling (2013), the plastic zone must be considerably smaller than any structure end (Figure 2.10(b)). A distance of $8r_{pl}$ is usually considered reasonable. For a plane stress state, the radius of the plastic zone is:

$$r_{pl} = \frac{1}{2\pi}\left(\frac{K}{\sigma_y}\right)^2 \tag{2.24}$$

thus, the distances from the ends must be at least:

$$a, (l-a), h \geqslant \frac{4}{\pi}\left(\frac{K}{\sigma_y}\right)^2 \tag{2.25}$$

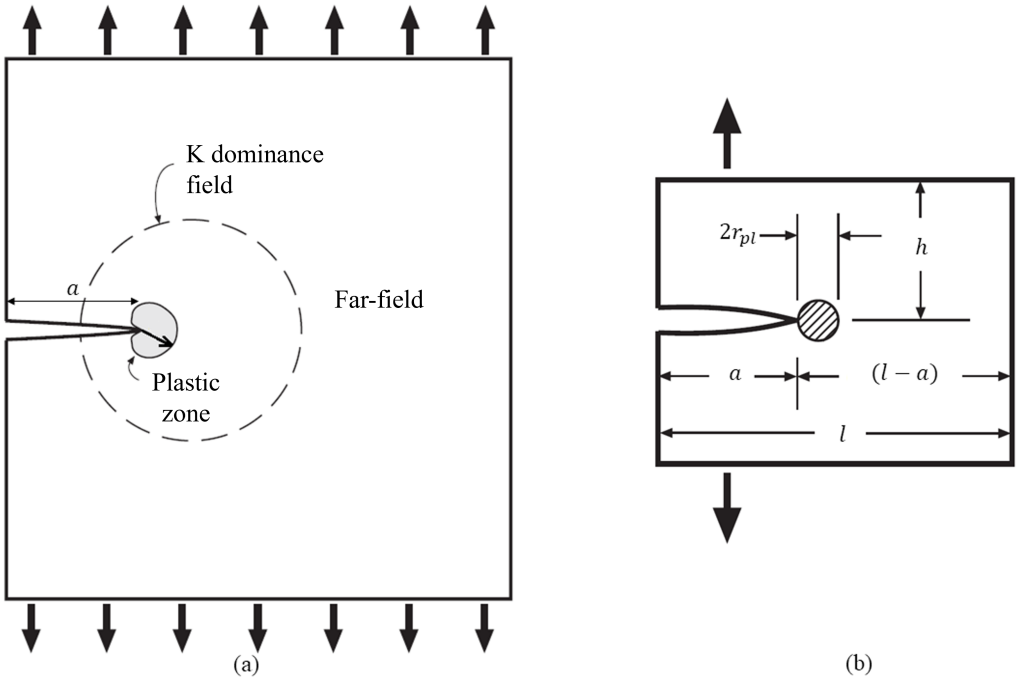

Figure 2.10: (a) Dominance zone of the Stress Intensity Factor. (b) Dimensions for the limitations of LEFM application. (DOWLING, 2013) - Adapted

2.3.2 Crack propagation

It has been defined that the Stress Intensity Factor (K) is a measure of stress and strain in the vicinity of the crack tip. Thus, we have that the crack propagation rate is also a function of K:

$$\frac{da}{dN} = f(\Delta K) \tag{2.26}$$

where $\frac{da}{dN}$ is the crack propagation rate, N is the number of fatigue cycles, and ΔK is the range of variation of the stress intensity factor at the crack tip.

If a significant volume of experimental data is plotted on a log-log scale graph of $\frac{da}{dN} \times \Delta K$, we have the behavior shown in Figure 2.11. One can observe a value of ΔK at which, from that point on, the propagation ceases to be considered null. This is a material property and is called the Threshold Stress Intensity Factor, ΔK_{th}. The figure also shows 3 stages for the presented curve. Stage 1 shows a considerable increase in $\frac{da}{dN}$ with a small variation in ΔK. Stage 2 comprises a linear variation, described by the Paris-Erdogan Law, Eq. 2.27 (PARIS, 1961), where C and m are material constants. Lastly, in stage 3, the propagation tends to infinity.

$$\frac{da}{dN} = C(\Delta K)^m \tag{2.27}$$

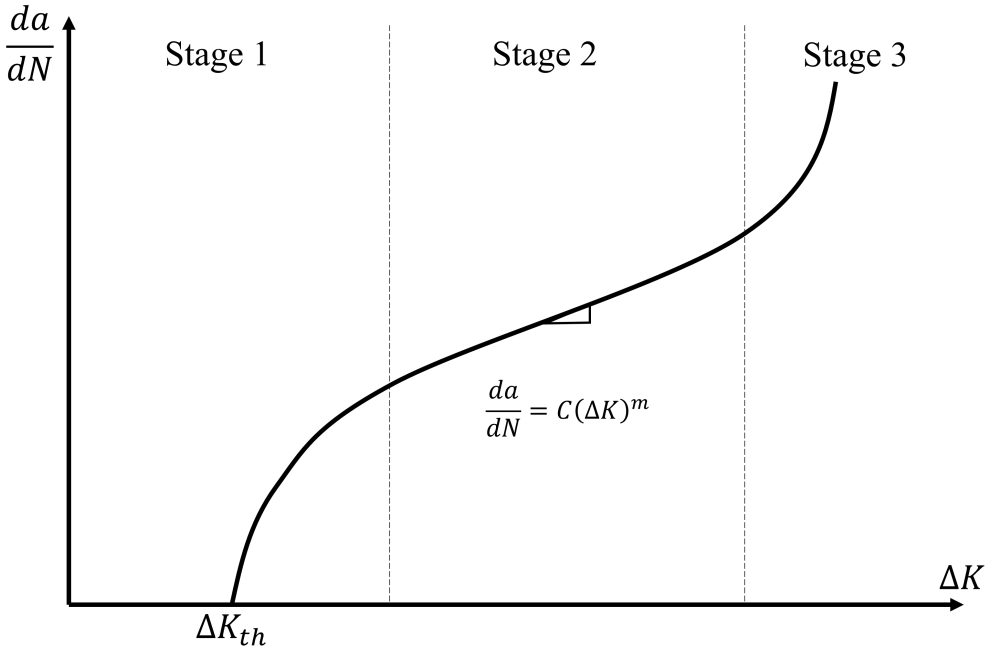

Figure 2.11: Crack growth rate as a function of ΔK

The calculations presented so far have been simplified for a 2D approach to the problem. To extend this approach to different geometries, such as a cylindrical section commonly used in experimental campaigns, some modifications must be made.

Following the work of engineers Forman and Shivakumar (1986), we should add a geometric shape factor F to the stress intensity factor amplitude. Thus, we have:

$$\Delta K = F\Delta\sigma\sqrt{\pi a} \tag{2.28}$$

and therefore we can substitute ΔK into the Paris Law (Eq. 2.27), isolate the life term, and integrate to obtain the propagation life:

$$N_p = \frac{1}{C}\int_{a_i}^{a_f} \frac{da}{(F\Delta\sigma\sqrt{\pi a})^m} \tag{2.29}$$

Figure 2.12 indicates how a circular section body would be divide with the into initiation, propagation and fracture sections. In the figure, a_i is the transition between the initiation and propagation phase, and a_f is the length at which the body undergoes catastrophic failure. Both are the integration limits of Eq. 2.29.

The length a_i does not have a consensus on its value in the literature. The crack length for

failure a_f is given by:

$$a_f = \frac{1}{\pi}\left(\frac{K_{Ic}}{F\sigma_{max}}\right)^2 \tag{2.30}$$

where K_{Ic} is the material fracture toughness in mode I, and σ_{max} is the maximum stress of the fatigue cycle.

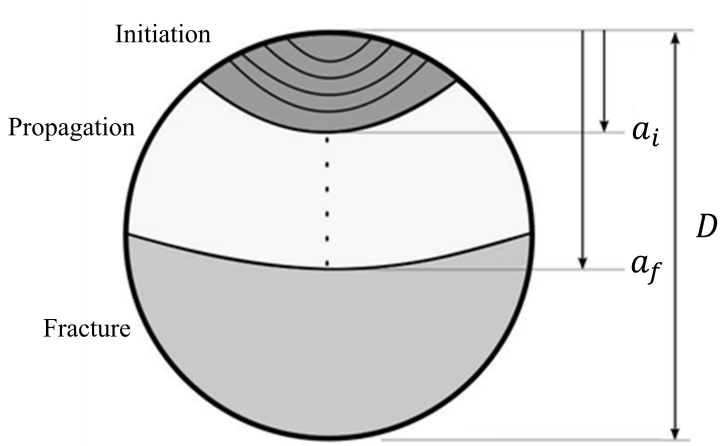

Figure 2.12: Fatigue phases in a circular section test specimen

Forman and Shivakumar, along with other scientists and engineers worked with NASA and the American Space Program on the assessment of propagation life and obtaining stress intensity factors to great amount of different geometries. Restricted at first to aerospace program, it was subsequently made available to the aeronautical sector through the NASGRO software (METTU et al., 1999). Many propagation models have already been implemented in this software, such as: Generalized Willenborg, Modified Generalized Willenborg, Constant Closure model, Walker-Chang model, and the deKoning-Newman Strain Ranges model, among others. The current version of this software (2023) is NASGRO 10.2, and it continues to be improved.

Chapter 3

Contact mechanics between cylinders

This chapter is intended to explain the mechanics of contact between cylinders, used as basic theory for analyzing elements in fretting. The advantage of studying the phenomenon as infinitely long cylinders is the two-dimensional approach to this analysis. In practice, stresses at the ends of real cylinders can interfere, but far from these ends and attenuating their effects, two-dimensional stresses represent the studied phenomenon well if we are capable of ensure a crack nucleation in a plane-strain state. This type of contact is knows as Hertz contact (HERTZ, 1882), and contact stresses distribution have been shown by Cattaneo (1938) and Mindlin (1949) and the analysis of stress under the contact used here was detailed by Hills and Nowell (1994) and more thorough demonstrations can be found in Nowell's PhD Thesis (NOWELL, 1988).

3.1 Superficial stresses

Firstly, to obtain the stress field in the contact region, one needs to find the magnitude and distribution of contact stresses. Two integral equations are used: the first one (Eq. 3.1) relates the pressure distribution $p(x)$ to the normal displacement $h(x)$, and the second one (Eq. 3.2) relates the superficial shear stress $q(x)$ to the relative tangential displacement $g(x)$.

$$\frac{1}{A}\frac{\partial h}{\partial x} = \frac{1}{\pi}\int \frac{p(\xi)d\xi}{x-\xi} \tag{3.1}$$

$$\frac{1}{A}\frac{\partial g}{\partial x} = \frac{1}{\pi}\int \frac{q(\xi)d\xi}{x-\xi} \tag{3.2}$$

where A is the composite compliance, defined as:

$$A = 2\left(\frac{\kappa_d + 1}{4\mu}\right) \tag{3.3}$$

being $\kappa_d = 3 - 4\nu$ for plane-strain state, ν is the Poisson's ratio and μ is the modulus of rigidity.

3.1.1 Normal loading

We continue with the fretting configuration between cylinders exposed by Hills and Nowell (1994), which has been widely validated since then by Araújo, Martín, Vázquez, among other authors. Figure 3.1 shows this configuration. The Hertz solution is used for the pressure distribution in the cylinders, where each one is considered here as an elastic half-plane. The normal loading P is defined as the force loading per unit thickness, th, and the equivalent radius of the cylinders is R^*, Eq. 3.7.

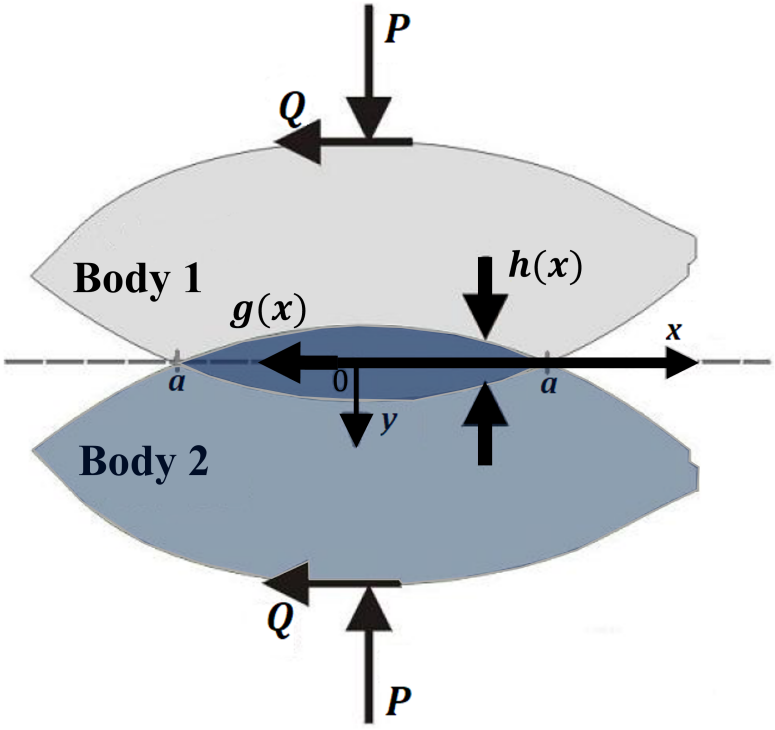

Figure 3.1: Contact between two elastically deformable bodies under normal, P, and tangential loading, Q.

The result from Hertz (1882) is that the pressure distribution occurs elliptically, defined by the following equations, where subscripts 1 and 2 represent their respective bodies, and E is the modulus of elasticity.

$$p(x) = -p_0\sqrt{1 - \left(\frac{x}{a}\right)^2} \tag{3.4}$$

$$-p_0 = \frac{2P}{\pi a} \tag{3.5}$$

$$a = \sqrt{\frac{4PR*}{\pi E*}} \tag{3.6}$$

$$R^* = \left(\frac{1}{R_1} + \frac{1}{R_2}\right)^{-1} \tag{3.7}$$

$$E^* = \left(\frac{1-{\nu_1}^2}{E_1} + \frac{1-{\nu_1}^2}{E_2}\right)^{-1} \tag{3.8}$$

It is worth noting that when testing a cylindrical surface pad on a flat specimen, one of the bodies has an infinite radius, so the equivalent radius is the radius of the pad, $R^* = R_{\text{pad}}$. However, for specimens and pads of the same material, the equivalent modulus of elasticity is not E of the material, but rather:

$$E^* = \frac{E}{2(1-\nu^2)} \tag{3.9}$$

3.1.2 Tangential loading

Now, the tangential load, Q, is responsible for the shear stresses. Fretting consists of phenomenon of partial sliding due to a tangential loading smaller than the friction limit for full sliding between the contact surfaces. As a result, two symmetric slip zones are formed where $c \leqslant |x| < a$, and an adhesion/ stick zone $|x| < c$, as shown in Figure 3.2.

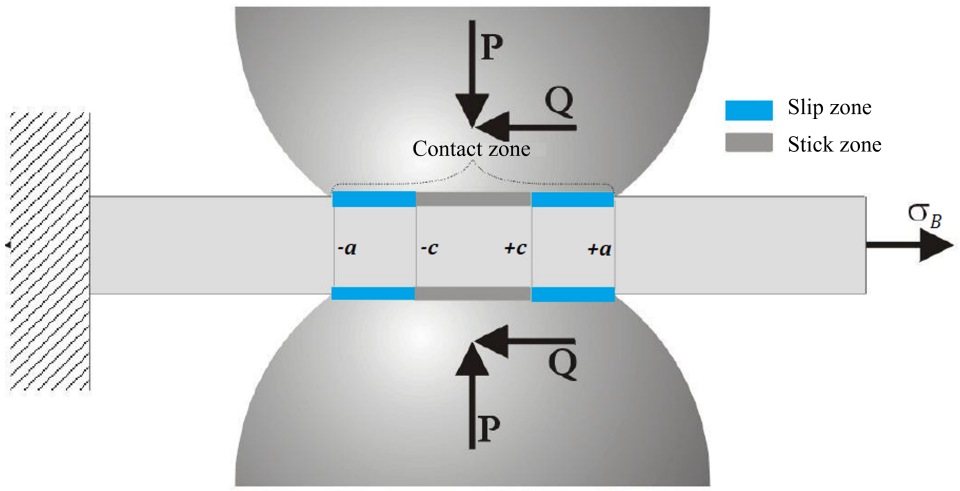

Figure 3.2: Contact slip and stick zones for a partial slip fretting configuration

due to the aforementioned, it is reasonable to model the shear stresses as the solution for full sliding, where f is the coefficient of friction, added by a perturbation $q'(x).q(x) = fp_0\sqrt{1-\left(\frac{x}{a}\right)^2} - q'(x)$(3.10)

In the adhesion zone, the perturbation can be obtained by solving integral 3.2, (HILLS; NOWELL, 1994). As a boundary condition, it is considered that there is no relative motion in the adhesion region, meaning: $g(x) = 0$, where $|x| < c$.

$$q'(x) = fp_0 \frac{c}{a} \sqrt{1 - \left(\frac{x}{c}\right)^2}, \qquad |x| < c \tag{3.11}$$

In the slip zone, there is no perturbation in the complete solution (Eq. 3.12), and the size of the adhesion zone, c, is obtained by tangential equilibrium (Eq. 3.13).

$$q'(x) = 0, \qquad c \leqslant |x| \leqslant a \tag{3.12}$$

$$\frac{c}{a} = \sqrt{1 - \left(\frac{Q}{fP}\right)} \tag{3.13}$$

The surface pressure and shear stress distributions, both normalized, are shown in Figure 3.3 for $f > 0.6$. In the center of the figure, the adhesion zone is evident due to the perturbation on the shear stresses.

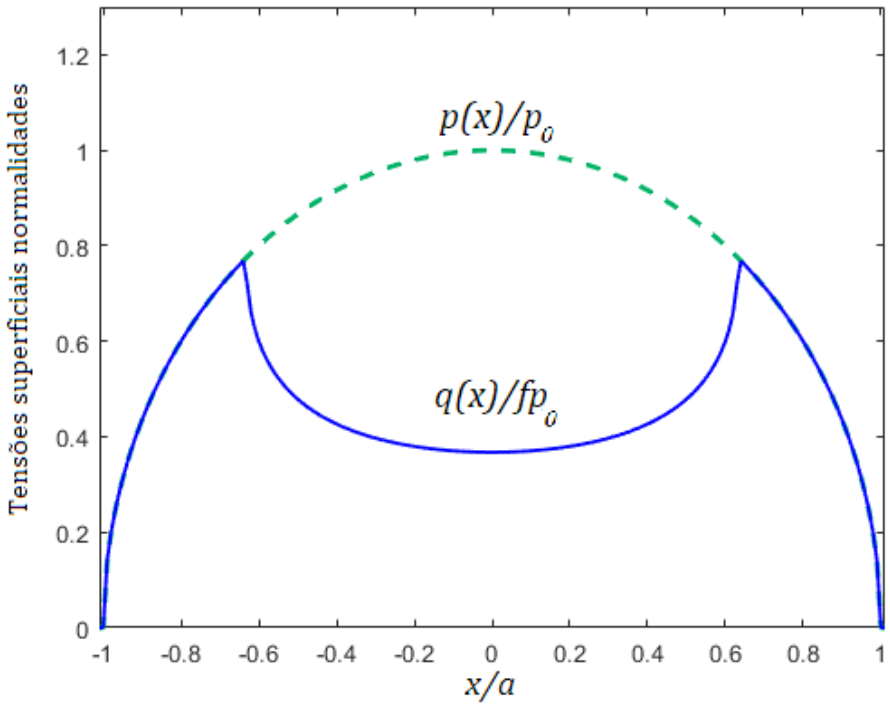

Figure 3.3: Superficial pressure and shear stress distribution for a typical loading configuration, $Q/fP = 0.6$, $\sigma_B/fp_0 = 0$.

So far, the tangential distribution has been developed for the case where the tangential loading of the cycle is maximum. It is necessary to evaluate the case of reverse loading in order to

characterize the stresses and/or deformations of the fretting phenomenon at any instant of time (HILLS; NOWELL, 1994).

The boundary conditions are imperative for a proper characterization. For the adhesion zone, the relative motion repeats $g(x) = 0$. For the slip zone, we have that for any x in this zone, the shear stress is given by Amontons-Coulomb's law for friction:

$$|q(x)| = -fp(x) \tag{3.14}$$

For the direction of the shear stresses, they are opposite to the motion of the surface, represented by the displacement rate in the x direction, $\frac{dg}{dt}$.

$$sgn(q(x)) = -sgn\left(\frac{\partial g}{\partial t}\right) \tag{3.15}$$

And, in the adhesion region, where the relative displacement between the bodies is zero, the shear stress on the surface must be less than the limit defined by Eq. 3.14 to ensure partial slip condition.

$$|q(x)| < -fp(x) \tag{3.16}$$

Figure 3.4 describes how the tangential load Q varies with time t. The equations described from 3.10 to 3.13 describe $q(x)$ well for the first phase of loading (from $Q = 0$ to point I). However, during the unloading between points I and II, the relative motion would change direction, causing complete adhesion of the contact as well as a violation of Eq. 3.15. By the point III of unloading, is seen reverse slip at the contact boundaries, resulting in a new slip zone ($c' \leqslant |x| < a$) where the shear stresses on the surface reverse direction.

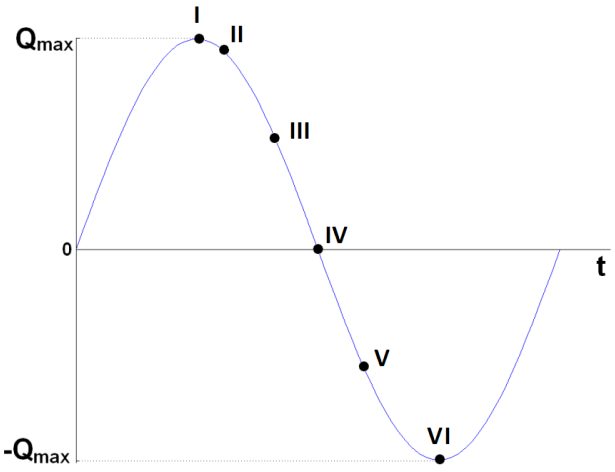

Figure 3.4: Tangential loading Q variation with time t (HILLS; NOWELL, 1994) - Adapted

Then, analogously, it is defined that within the adhesion zone, the correction factor surface stress added to predict slipping is given by:

$$q''(x) = 2fp_0\frac{c'}{a}\sqrt{1-\left(\frac{x}{c'}\right)^2} \tag{3.17}$$

where the factor of 2 cancels out the relative motion when the surface stresses change from $fp(x)$ to $-fp(x)$. Table 3.1 brings the shear stresses for each zone of the surface during this unloading phase.

Table 3.1: Surface shear stresses for the contact region during the time variation of tangential loading

$\frac{q(x)}{fp_0}$	Zone of correspondence
$-\sqrt{1-\left(\frac{x}{a}\right)^2}$	$c' < \lvert x\rvert \leqslant a$
$-\sqrt{1-\left(\frac{x}{a}\right)^2}+2\frac{c'}{a}\sqrt{1-\left(\frac{x}{c'}\right)^2}$	$c < \lvert x\rvert \leqslant c'$
$-\sqrt{1-\left(\frac{x}{a}\right)^2}+2\frac{c'}{a}\sqrt{1-\left(\frac{x}{c'}\right)^2}-\frac{c}{a}\sqrt{1-\left(\frac{x}{c}\right)^2}$	$\lvert x\rvert \leqslant c$

The new adhesion zone in reverse loading is defined by c' (Eq. 3.18), more external than c, also obtained by equilibrium.

$$\frac{c'}{a} = \sqrt{1-\left(\frac{Q_{max}-Q}{2fP}\right)} \tag{3.18}$$

The Figure 3.5 shows the variation of surface stresses $q(x)$ normalized for different values of shear load Q defined by Figure 3.4. From top to bottom, the curves are given for points I, III, IV, V, and VI. Two aspects are worth noting: first, the stress at the maximum (I) and minimum (VI) points are equal in magnitude and opposite. Second, when $Q = 0$ (point IV), the surface stress is in equilibrium but non-zero along the contact, making it clear that the friction in the contact depends on the fretting loading history.

3.1.3 Remote bulk fatigue load effects

The last load to be evaluated is the fatigue load, determined by σ_B in Figure 3.2. When this load is applied in phase with the tangential load, a displacement e occurs in the adhesion zone during the points of maximum and minimum of σ_B and Q. For reloading and unloading, we have a displacement of the adhesion zone given by e'. According to Hills and Nowell (1994), these displacements are defined as follows:

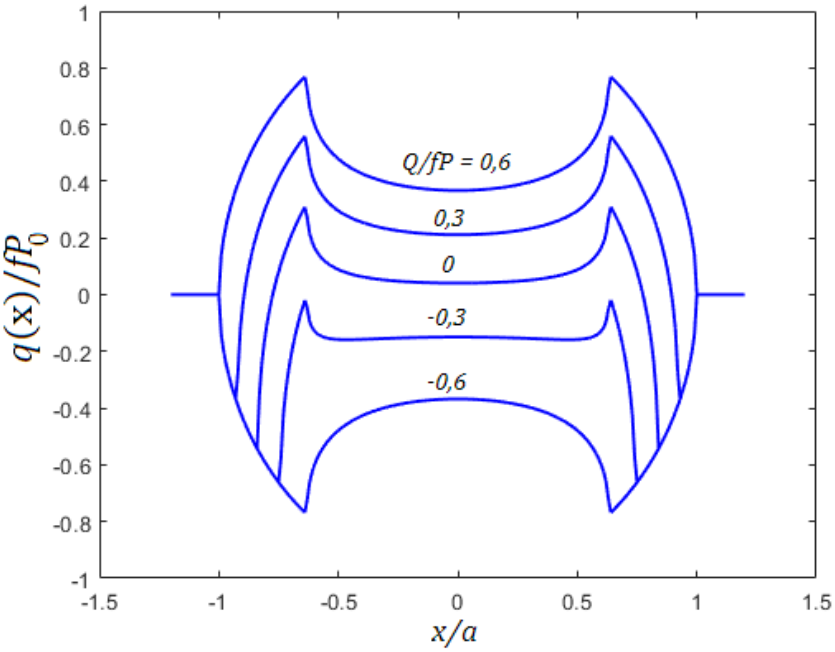

Figure 3.5: Variation of surface shear stresses at different moments of cyclic tangential loading. Q/fP ranging from ± 0.6

$$\frac{e}{a} = \frac{\sigma_B^{max}}{4fP} \tag{3.19}$$

and

$$\frac{e'}{a} = \frac{\sigma_B^{max} - \sigma_B(t)}{8fP} \tag{3.20}$$

The Figure 3.6 demonstrates the effect of the remote fatigue load compared to the previous Figure 3.5. It is imperative to emphasize an important condition for the equations presented. This condition is that the fatigue load must be small or moderate so that the regions are defined as follows:

$$e + c < a \qquad e \qquad e' + c' < a \tag{3.21}$$

otherwise, the displacement of the adhesion zone and consequently the stresses would have to be obtained numerically.

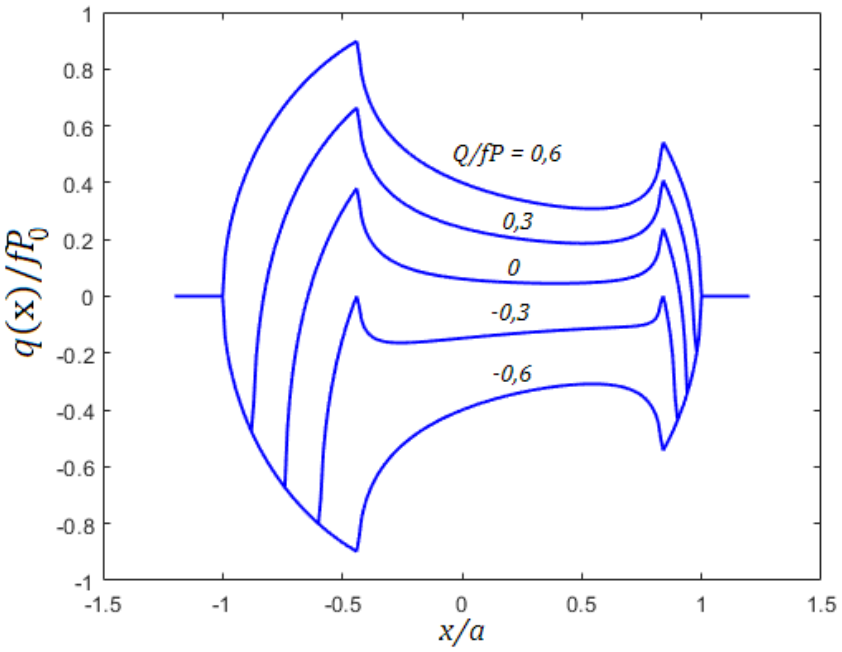

Figure 3.6: Effect of the remote bulk fatigue load on the shear stresses shown in Figure 3.5 for σ/p_0 varying between ± 0.6.

3.2 The cyclic stress field within the contact region

The resulting stress field below the contact surface is obtained by superposing the stress fields of $p(x)$ and $q(x)$ as well as the perturbation terms $q^{'}(x)$ and $q^{''}(x)$. Due to the fretting loading history, superposition needs to be performed for four different stages: the maximum, minimum, unloading, and reloading stages. The solutions for these stress fields are solved in plane strain using the Muskhelishvili potentials (MUSKHELISHVILI et al., 1953). Hence, as example, only the σ_{xx}/p_0 component for the four loading stages is provided next (Eqs. 3.22−3.25). Other components are thoroughly describe and solved similarly (NOWELL, 1988; HILLS; NOWELL, 1994).

During maximum loading,

$$\frac{\sigma_{xx}(x,y)}{p_0} = \left(\frac{\sigma^n_{xx}(\frac{x}{a},\frac{y}{a})}{p_0}\right) + f\left(\frac{\sigma^t_{xx}(\frac{x}{a},\frac{y}{a})}{fp_0}\right) - f\frac{c}{a}\left(\frac{\sigma^t_{xx}(\frac{x-e}{c},\frac{y}{c})}{fp_0}\right) + \frac{\sigma_B}{p_0} \tag{3.22}$$

During unloading,

$$\frac{\sigma_{xx}(x,y)}{p_0} = \left(\frac{\sigma^n_{xx}(\frac{x}{a},\frac{y}{a})}{p_0}\right) - f\left(\frac{\sigma^t_{xx}(\frac{x}{a},\frac{y}{a})}{fp_0}\right) + 2f\frac{c'}{a}\left(\frac{\sigma^t_{xx}(\frac{x-e'}{c'},\frac{y}{c'})}{fp_0}\right) - f\frac{c}{a}\left(\frac{\sigma^t_{xx}(\frac{x-e}{c},\frac{y}{c})}{fp_0}\right) + \frac{\sigma_B}{p_0} \tag{3.23}$$

During minimum loading,

$$\frac{\sigma_{xx}(x,y)}{p_0} = \left(\frac{\sigma^n_{xx}(\frac{x}{a},\frac{y}{a})}{p_0}\right) - f\left(\frac{\sigma^t_{xx}(\frac{x}{a},\frac{y}{a})}{fp_0}\right) + f\frac{c}{a}\left(\frac{\sigma^t_{xx}(\frac{x-e}{c},\frac{y}{c})}{fp_0}\right) + \frac{\sigma_B}{p_0} \tag{3.24}$$

During reloading,

$$\frac{\sigma_{xx}(x,y)}{p_0} = \left(\frac{\sigma^n_{xx}(\frac{x}{a},\frac{y}{a})}{p_0}\right) + f\left(\frac{\sigma^t_{xx}(\frac{x}{a},\frac{y}{a})}{fp_0}\right) - 2f\frac{c'}{a}\left(\frac{\sigma^t_{xx}(\frac{x-e'}{c'},\frac{y}{c'})}{fp_0}\right) + f\frac{c}{a}\left(\frac{\sigma^t_{xx}(\frac{x-e}{c},\frac{y}{c})}{fp_0}\right) + \frac{\sigma_B}{p_0} \tag{3.25}$$

Where the superscript n refers to the tensor produced by normal loading and t to the tangential one.

Chapter 4

Materials and experimental campaign

In this chapter it will be described the properties of the material used in this work, characterizing its mechanical behavior and fatigue strength. It will also contain the presentation of the testing rig used for experimentation of the fretting fatigue test campaign and at last the detailing of the tests carried out.

4.1 Material - 7075-T651 Aluminum alloy

The material used in this work was the Aluminum alloy 7075-T651, a high-strength aluminum alloy commonly used in aerospace and high-performance applications. It undergoes a specific heat treatment process called T651, which involves solution heat treatment followed by artificial aging. This treatment enhances its mechanical properties, including strength and hardness, while also improving its resistance to corrosion. As a aluminum alloy, it offers great strength-to-weight ratio and good machinability. The chemical composition of that defines material is given by Table 4.1.

Table 4.1: Chemical composition of Aluminum alloy 7075-T651 (% of mass)

Chemical composition (% mass) - (ALCOA, 2001; VÁZQUEZ; NAVARRO; DOMÍNGUEZ, 2017)										
%	Al	Zn	Mg	Cu	Fe	Si	Mn	Cr	Ti	Others
Max.	91,4	6,1	2,9	2,0	0,5	0,4	0,3	0,28	0,2	0,05
Min	87,1	5,1	2,1	1,2	-	-	-	0,18	-	-

Full characterization of the material is not a part of the present work, hence, the properties for the Al 7075-T651 shown here were taken by Pinto (2022) for his PhD dissertation and and also by ALCOA (2001), Navarro, Vázquez, and Domínguez (2011) and Boller and Seeger (2013). The experimental work conducted in the present document was done using pad and specimens from the same batch as Pinto's work.

4.1.1 Monotonic Properties

Pinto (2022) took these monotonic properties in the laboratories of the Group of fatigue, fracture and materials laboratories of the University of Brasília. For the tensile tests, he followed the manufacturing and procedures in accordance with ASTM E8/E8M-16 (specimen dimensions in Figure 4.1) and carried them out in a MTS 810 Servo Hydraulic Machine paired with a model 634.11F-24 strain gauge. As for the hardness test, it was taken in accordance with ASTM E18-19 in a Durometer Zwick Roell ZHU 250. Good accordance to the ASM international standards were found.

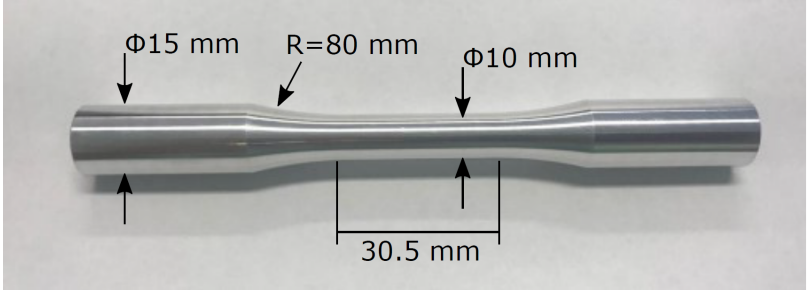

Figure 4.1: Tensile and fatigue test specimen (PINTO, 2022)

The properties are shown in Table 4.2 and the $\sigma - \varepsilon$ diagram in Figure 4.2. For a more thorough explanation, one may consult Pinto (2022).

Table 4.2: Mechanical properties of the Al 7075-T651 (PINTO, 2022)

Monotonic properties	
Hardness Rockwell B	88.7 HRB
Elasticity Modulus, E	68 GPa
Poisson's Ratio, ν	0.33
Yield strength, σ_y	506 MPa
Tensile strength, σ_u	570 MPa
Fracture toughness, K_{Ic}	26 MPa$\sqrt{m}$
Critical distance static strength L_s	662 μm

4.1.2 Fatigue properties

This material has been characterize many times by different author and institutions. Besides, Pinto (2022) this material has also been fatigue tested by Jiang, Hertel, and Vormwald (2007), Navarro, Vázquez, and Domínguez (2011), Boller and Seeger (2013) and Furuya et al. (2019). This section contains a summary of all the properties gathered by them and used for life estimation.

Pinto (2022) carry out experimentation following the ASTM E739 and E466. He load the test specimens (Figure 4.1) with uniaxial and also with torsional fatigue loading using a MTS 809

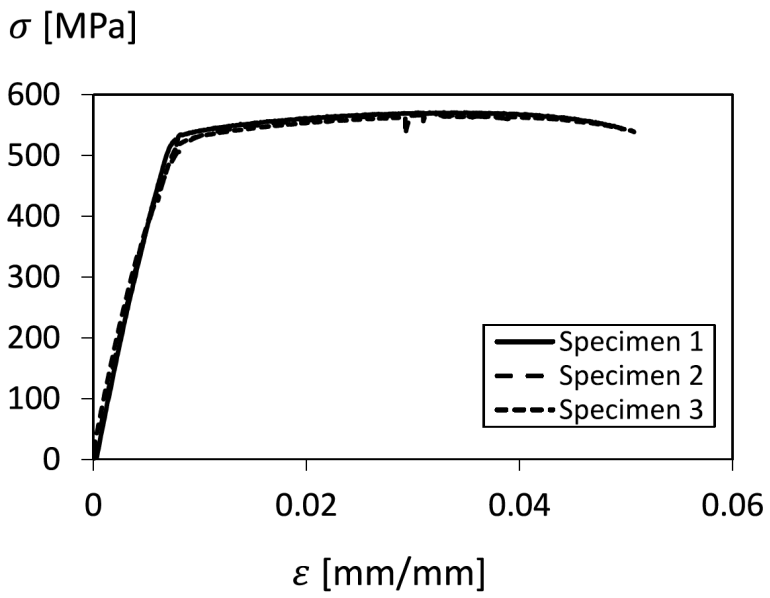

Figure 4.2: $\sigma - \varepsilon$ diagram for Al 7075-T651 (PINTO, 2022)

Servo Hydraulic axial-torsional machine. The loading ratio in both cases were equal to $R = -1$. From his work it is possible to obtain normal and shear stress amplitude curves in respect to fatigue lives as well as some characteristics regarding the crack propagation, as the stress intensity factor threshold and constants of Paris' Law (2.27). The Axial $\sigma - N_f$ and the Torsional $\tau - N_f$ curves are in Figure 4.3, and they gave fatigue limit ranges of respectively: $\Delta\sigma_{-1} = 427MPa$ and $\Delta\tau_{-1} = 337MPa$, both for fatigue limit of 10^6 cycles.

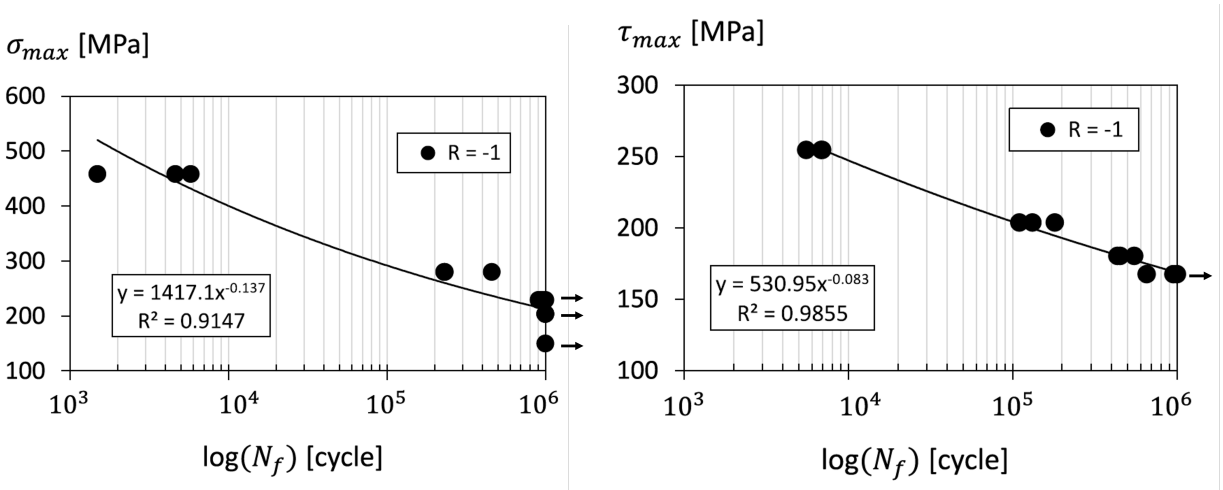

((a)) Uniaxial $\sigma - N_f$ curve for $R = -1$

((b)) Torsional $\tau - N_f$ curve for $R = -1$

Figure 4.3: Stress amplitude vs final lives curves Pinto (2022)

Other properties gathered from the literature are presented in Table 4.3.

Table 4.3: Main properties for Al 7075-T651 in the literature

Elasticity Modulus[1,2,4]	E	$68 - 70$ GPa	Fatigue limit range $R = 0.05$[4]	$\Delta\sigma_{-1}$	350 MPa
Poisson's Coeff.[1,2,4]	ν	0.33	Critical distance static strength[4]	L_∞	19.5 μm
Yield Strength[1]	σ_y	503 MPa	Fatigue strength coeff.[3]	σ'_f	1231 MPa
Ultimate strength[1]	σ_u	572 MPa	Fatigue ductility coeff.[3]	ε'_f	0.263
Threshold stress intensity factor mode I[4] (R = 0.1)	ΔK_{th}	2.74 MPa$\sqrt{m}$	Fatigue strength exp.[3]	b	-0.122
Paris' Law coeff.[4] (R=0)	C	$5.17\dot{1}0^{-7}$	Fatigue ductility exp.[3]	c	-0.806
Paris' Law exp.[4] (R=0, MPa$\sqrt{m}$)	m	2.72	Grain size[1]	d	50 μm

[1] University of Seville (ERENA GUARDIA et al., 2022)
[2] (ALCOA, 2001)
[3] (BOLLER; SEEGER, 2013)
[4] (PINTO, 2022)

4.2 Testing Rig

The fretting fatigue testing rig of the University of Brasília is a one of a kind, state of the art machine that is able to carry out the vanguard of fretting fatigue experiments, such as high temperature test, independent loading conditions for every actuator, out-of-phase loading, etc. All of that, brings the machine even closer to what actual components suffer during a aircraft cycle in the most high-end jet engines. The schematic of Figure 4.4 shows what is contained in such machine. A more thorough explanation of the rig can be found in Almeida et al. (2022).

In the machine, the flat dog-bone tensile specimen (8) is held between by one fixed and one movable hydraulic grip/jaw (6 and 7). The movable grip (7) is linked to a load cell (4) and to a hydraulic actuator (3) capable of applying loads up to $250\ kN$. This actuator is responsible for applying the remote bulk load or fatigue load (B or F_B) on the specimen. The fretting apparatus is linked and guided by 4 columns to another load cell and LVDT sensor (2) and to the hydraulic actuator (1), which is in charge of providing fretting loads up to $100\ kN$, in other words, the tangential/frictional load, Q. Lastly, on the side view of Figure 4.4 it is possible to see a closer look of how the fretting apparatus works. Both actuators (9) apply the normal pressure load, P, to the fretting contact. As aforementioned, when applying the fretting load the entire fretting apparatus plus the testing pad move generating the tangential load. It is possible to place an igniter (13 - Figure 4.5) for high temperature testing, however the insulation is suppressed in the schematics. Another possibility is to install in the principal columns a DIC system (15) to obtain the displacement field of the free surface of the contact (unfortunately it is not possible to acquire images while testing in high temperature).

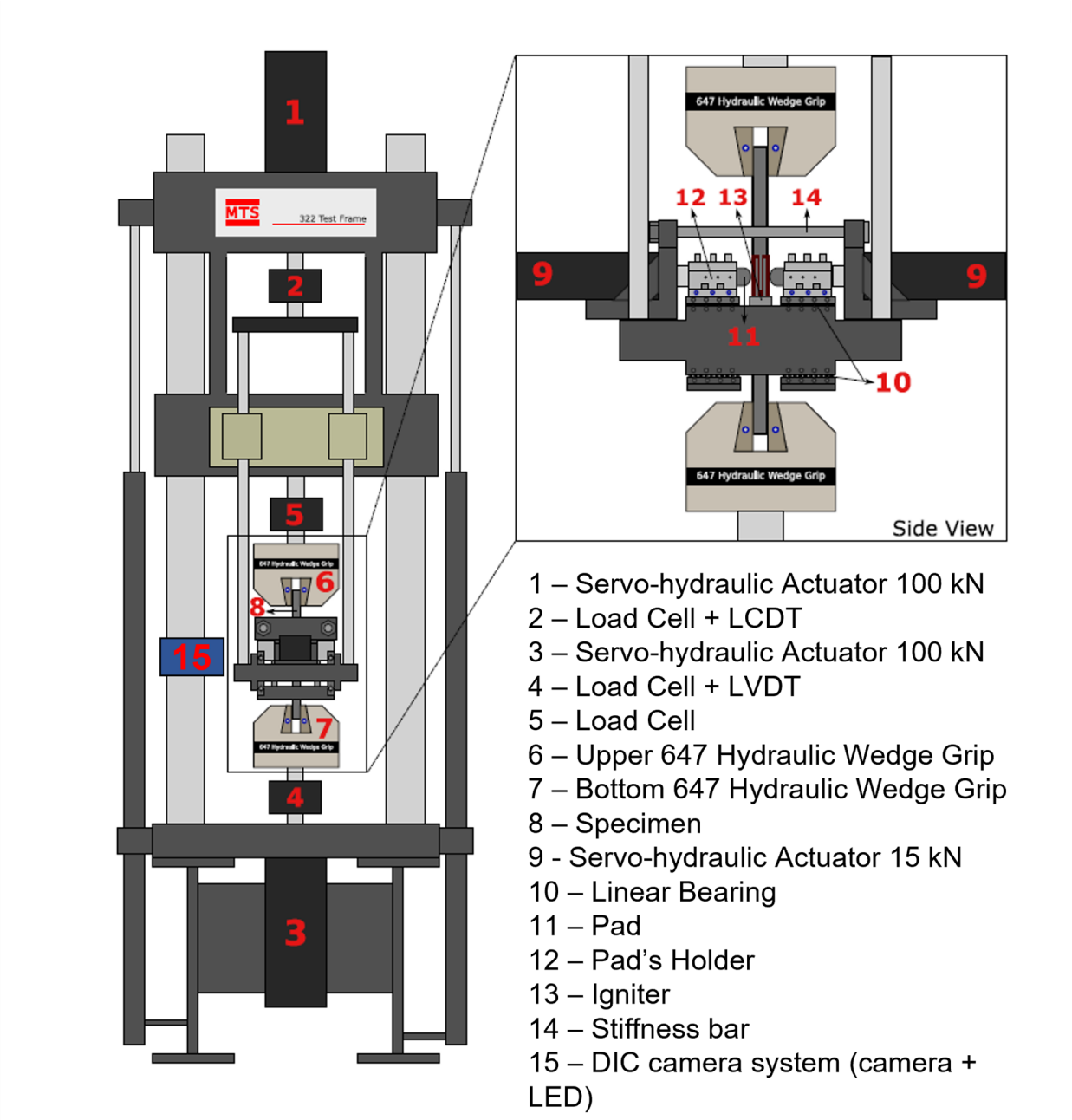

Figure 4.4: Schematic of the four actuators fretting fatigue rig (ALMEIDA et al., 2022).

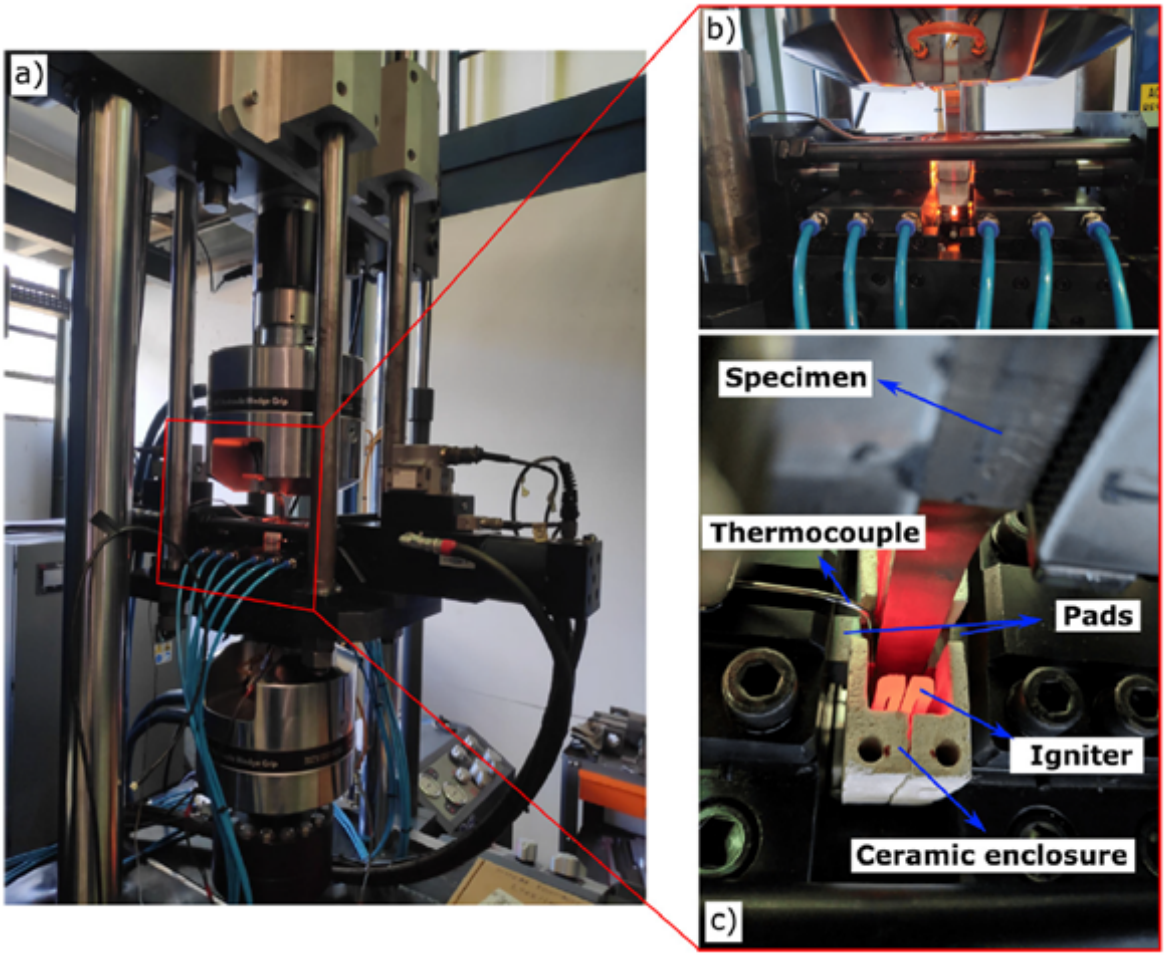

Figure 4.5: Four actuator testing rig high temp apparatus close-up (ALMEIDA et al., 2022).

4.3 Experimental campaign

4.3.1 Fretting fatigue tests

These fretting fatigue tests are the main experiments of this work since their goal is to validate the fretting fatigue life estimate methodology and the main theory of this dissertation, which is that the pad overhang length between support apparatus and contact surface change the fretting fatigue life meaningfully. Figure 4.6 shows a schematic of the pad contact to the specimen and what is considered to be the overhang distance. This overhang distance can be changed by machining the length of the pad or by changing the diameter of the steel roller (top of the image) that is used to properly apply the Normal load P when aligning the Pad to the contact surface.

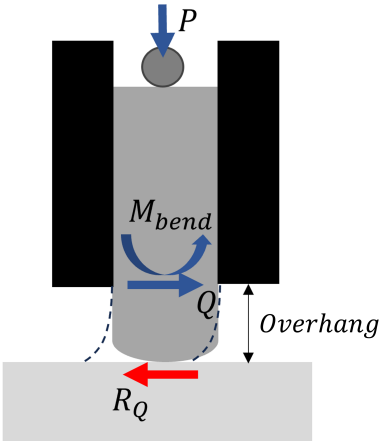

Figure 4.6: Schematic of the Pad and Specimen contact overhang.

4.3.1.1 Test procedure

The following is a brief step-by-step procedure on how to perform a fretting fatigue test at UnB's testing rig.

1. to position the test specimen (Figure 4.7) on the rig;
2. to measure that the specimen is leveled by measuring top and bottom distance between specimen and hydraulic grip walls. It is recommended the usage of a Pachymeter;
3. to apply the mean fatigue bulk load to the specimen, if needed. The bulk load actuator is the one for $250\ kN$;
4. to align the pad contact surface. The proper way to align the surface is done by adjusting side screws that keep it in place and applying a slight pressure on the contact zone measuring it with a pressure sensitive film, Figure 4.8 shows the desired mark.

5. to apply the Normal pressure load. This is done by applying load to both lateral actuators. Once both actuators have the desired load, you may assign one to displacement control;

6. to start fretting wear slowly in displacement control until it reaches the desired tangential load magnitude. This is done by varying the displacement of the $100\ kN$ actuator so the pad and specimen do not fully slip. A recommended frequency of loading is $3\ Hz$;

7. to apply slowly both tangential load and cyclic bulk load together until both reach the desired value;

8. once all loads are the desired, to increase frequency up until it reaches your frequency of choice. It is important to make sure the machine does not enter in resonance when increasing it. If it does, consider running the test with a lower one.

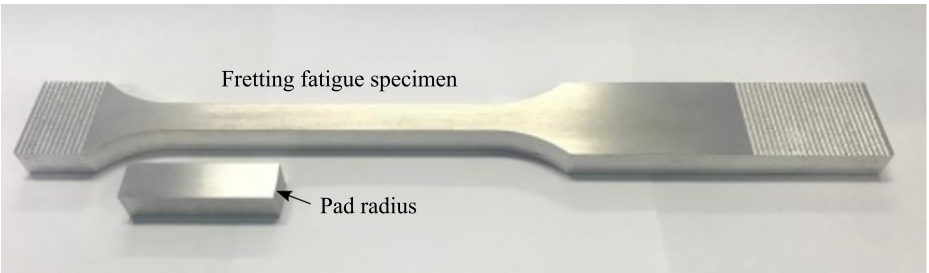

Figure 4.7: Test Specimen and Pad for a fretting fatigue experiment, dimensions on the Appendix.

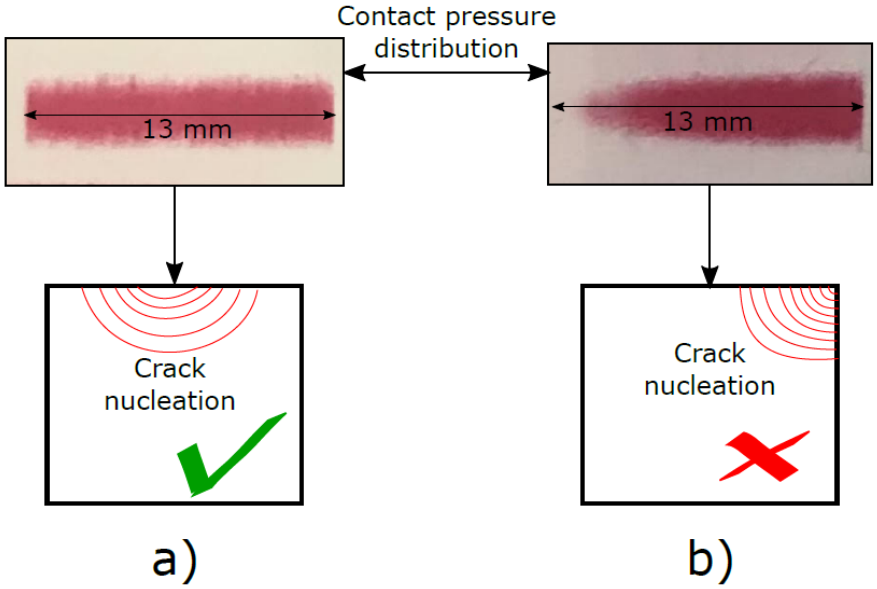

Figure 4.8: a) Well aligned and b) mis-aligned contact pressure mark between pad and specimen contact in pressure film (PINTO, 2022).

4.3.1.2 Test results

The fretting fatigue tests carried out for this work applied the same load for different overhang distances, the loads were:

- Normal Load $P = 5200\ N$, or $P^* = 400\ N/mm$.
- Tangential Load $Q = 2080\ N$, or $Q^* = 160\ N/mm$. Hence, $Q/P = 0.4$.
- Mean bulk fatigue load $B_m = 10328\ N$, or $\sigma_{B_m} = 61.1\ MPa$.
- Cyclic bulk fatigue load amplitude $B_a = 8450\ N$, or $\sigma_{B_a} = 50\ MPa$. Hence, $\sigma_{B_a}/P_0 = 0.187$.

The table 4.4 shows the experimental life results from the fretting fatigue testing campaign.

Table 4.4: Fretting fatigue Experimental results

Overhang	Test	Experimental Life
$5\ mm$	FF-05-01	193437
	FF-05-02	224749
$9\ mm$	FF-09-01	139263
	FF-09-02	261442
$13\ mm$	FF-13-01	142219
	FF-13-02	141548
	FF-13-03	165022
$20\ mm$	FF-20-01	Resonance
	FF-20-02	Resonance
	FF-20-03	Cracked Pad

4.3.1.3 Problems remarks

As seen from Table 4.4, it is possible to see that the tests performed with $20\ mm$ overhang where not possible to be performed. When applying the desired frequency of $10\ Hz$ to the test, both FF-20-01 and FF-20-02 entered in resonance, making the contact lose their partial slip condition and scrape hard the pad against the specimen, and the test had to be emergency stopped. When increasing the frequency, the machine feedback shows us a sign that increasing it more could induce a severe resonance, the Figure 4.9 shows what it looks like. By the figure, While the machine hydraulic command tries to apply a sinusoidal load, the machine feedback starts showing a small oscillation of the command before getting out of control.

At last, a lower frequency test was attempted to be applied, the test FF-20-03, on which the frequency was set to $5\ Hz$. But unfortunately, the bending moment was very high, generating a small but visible movement on the support flange that fixes the pad. The flange movement

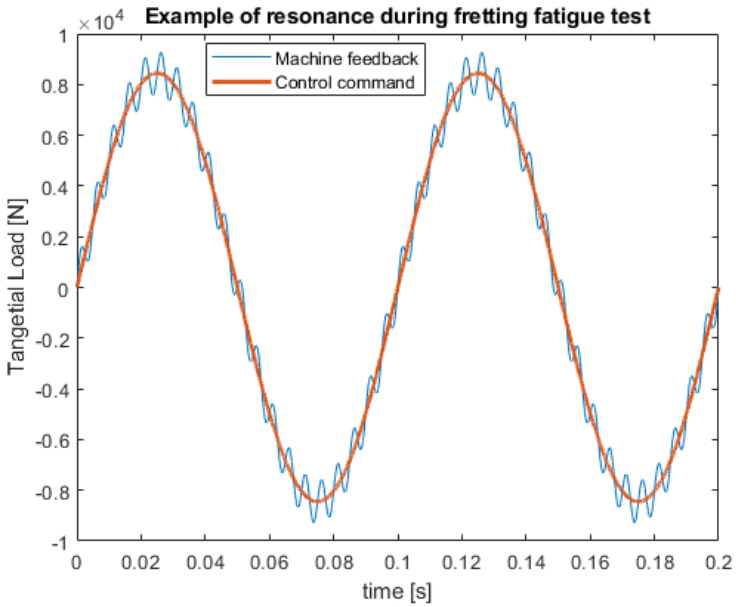

Figure 4.9: Example of small resonance on FF test.

generated a friction between it and the pad that caused fretting wear. Figure 4.10.a) shows the scar on the fretting apparatus flange and also in the pad. Moreover, 4.10.b) shows the crack that propagated due to the fretting wear added by the high bending moment . This cracked pad at the end caused a mis-alignment between the pad and the bearing that applies the normal load on the opposite side of the specimen in room temperature tests. The bearing cracked and broke, causing a intense jolt that made the machine stop due to safety detectors.

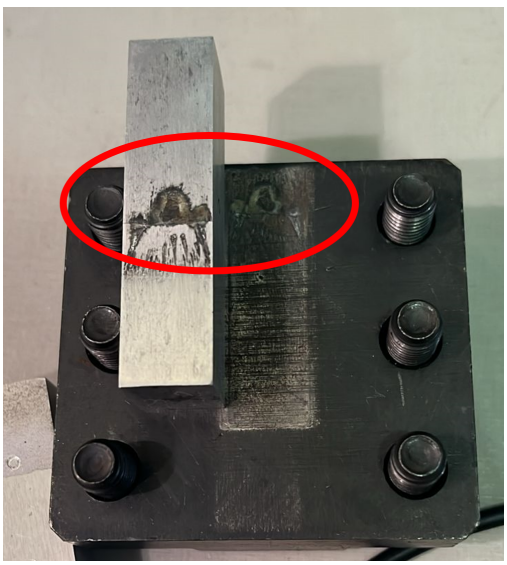

((a)) Fretting scar on flange and pad

((b)) Crack on pad due to high bending moment

Figure 4.10: Image results from test FF-20-03

4.4 Microscopic analysis

This section is focused on highlighting and evaluating some aspects from the contact surface and from the crack and fracture surface. For this, measurements were made using a Confocal microscope, Model Olympus LEXT OLS4000. Two different specimens were analyzed, one that was tested with $5\ mm$ overhang and the other with $13\ mm$. The $5\ mm$ was the test 'FF-05-02' and the one with $13\ mm$ was the 'FF-13-02'.

4.4.1 Contact surface measurements

The contact surfaces were measured aiming to analyze the fretting marks on them and estimating the slip zone size, the stick zone size and also estimating where the crack began. These was made by taking the images and then tracing 3 lines along the contact mark as Figure 4.11. Points 1 to 4 are from the first line, 5 to 8 from the second and 9 to 12 from the third, for both contact overhangs.

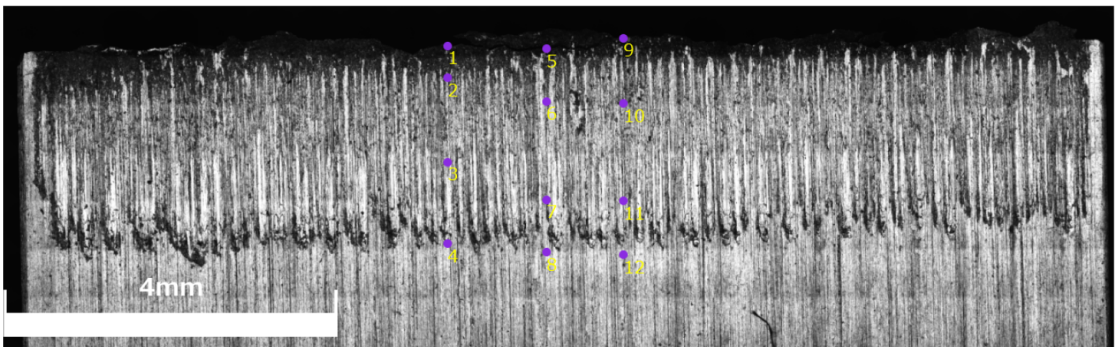

((a)) 5 mm overhang

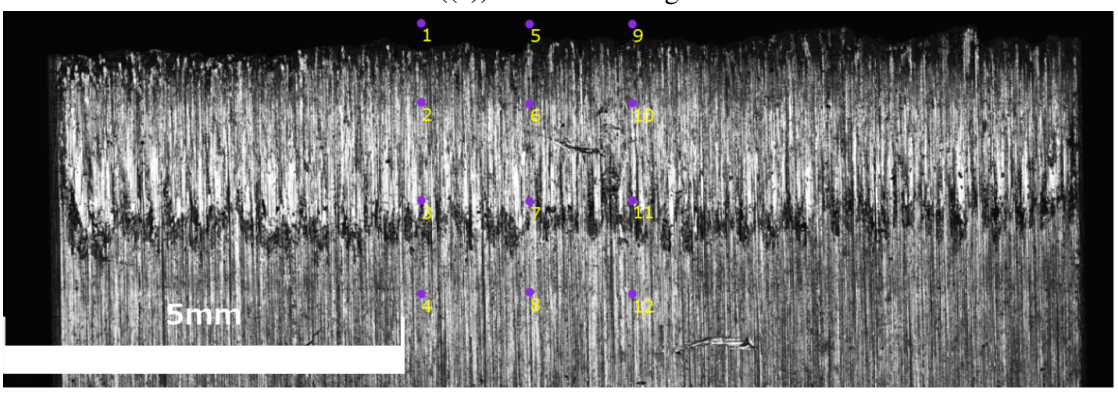

((b)) 13 mm overhang

Figure 4.11: Contact surface and points

By doing the profile of the lines in the contact surface, it was expected to estimate the zones in the fretting scar. Figure 4.12 shows the line profiles for both specimens. From them, it was possible to assure that wear and marks caused by the $13\ mm$ overhang to the specimen were way more intense. The marks made into the $5\ mm$ specimen were very difficult to pinpoint, even with the help of the color and laser images from the microscope it was really hard to proper access. From the Figure 4.12, it is clear the changes of level in the line profiles of the $13\ mm$ overhang contact scar, but not for the $5\ mm$.

Nonetheless, the estimation of the contact size, the stick zone size, the slip zone size were done for both. The slip zone was estimated by taking the average of the most external points as:

$$\text{Slip zone size} = \frac{\overline{4-3} + \overline{8-7} + \overline{12-11}}{3} \tag{4.1}$$

where the numbers represent the point position from Figures 4.11 and 4.12.

The same could be calculated for the stick zone by taking the average but of intermediate points:

$$\text{Stick zone size} = \frac{\overline{3-2} + \overline{7-6} + \overline{11-10}}{3} \tag{4.2}$$

The contact size and the crack nucleation position were taken then as, respectively:

$$\text{Experimental contact size} = a^{Exp.} = \text{Slip zone size} + \frac{\text{Stick zone size}}{2} \tag{4.3}$$

and

$$\text{Crack nucleation position} = \frac{\text{Stick zone size}}{2} + \frac{\overline{2-1} + \overline{6-5} + \overline{10-9}}{3} \tag{4.4}$$

being the average term representative in the last equation the average of the closest to fracture on the Figure 4.11.

The Table 4.5 was generated with results, more thorough data can be seen in the Appendix. From the Table, it can be said that the slippage was way higher for $13\ mm$ than for $5\ mm$ and that this is the main reason as why the contact size is different, of around $448\ \mu m$, or $33\ \%$ higher on the $13\ mm$ overhang specimen. All this difference is probably not only due to pad deformation, but also compliance of the machine apparatus itself. As for the crack nucleation point, the normalized by contact size value shows that no considerable difference can be seen comparing both cases.

Table 4.5: Microscopic results from the contact zone

Overhang	**Slip zone size**	**Stick zone Size**	**Contact size**	**Crack nucleation position**
5 mm	$749.8\ \mu m$	$1116\ \mu m$	$1307\ \mu m$	$1155\ \mu m = 0.88a^{Exp.}$
13 mm	$1149\ \mu m$	$1211\ \mu m$	$1755\ \mu m$	$1592\ \mu m = 0.90a^{Exp.}$

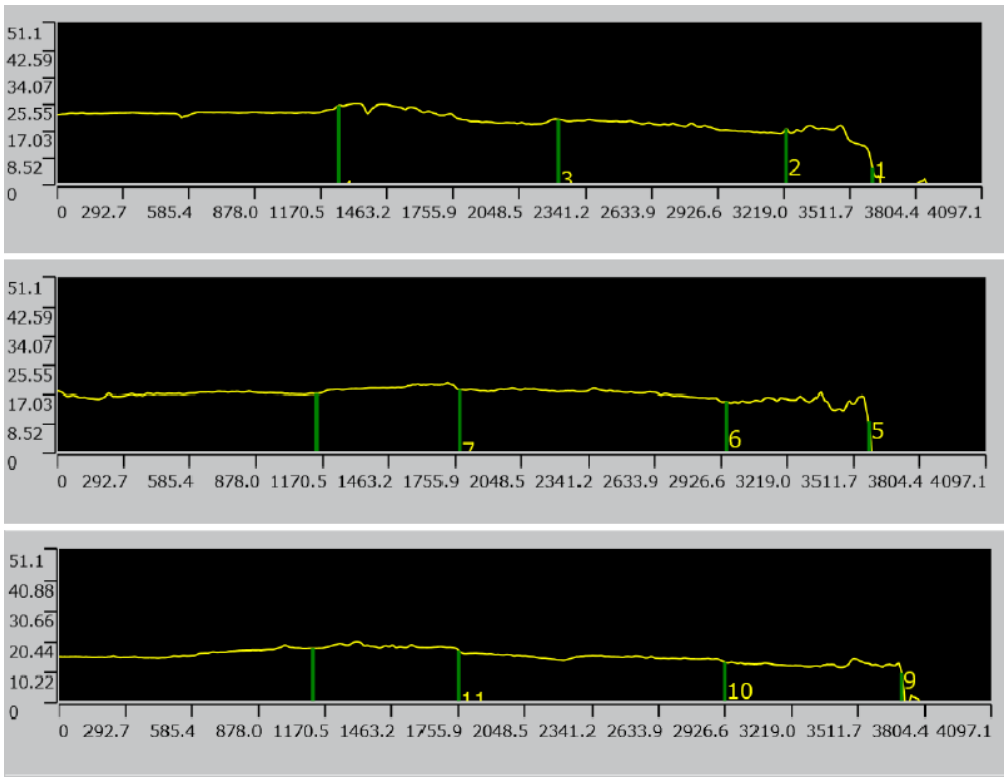

((a)) 5 mm overhang

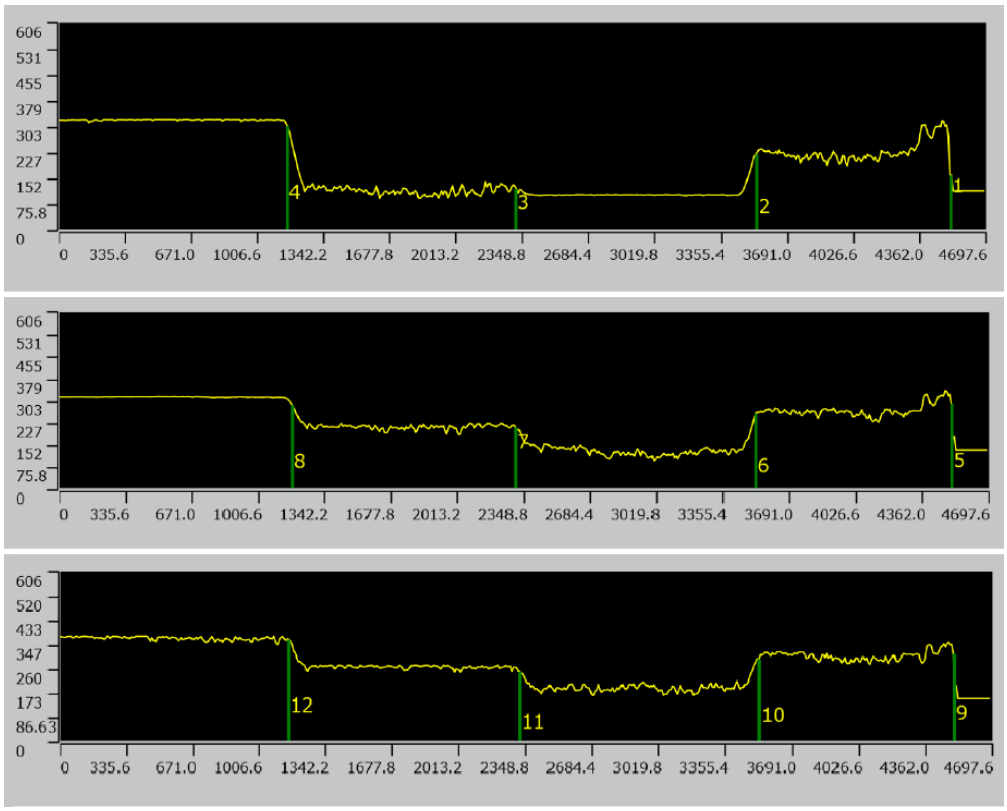

((b)) 13 mm overhang

Figure 4.12: Line profiles of the contact surface

4.4.2 Crack and fracture surface measurements

After the contact surface evaluation, it was made the analysis of the crack and fracture surface for the same specimens. Figure 4.13 shows the cracked surface for both specimens, showing the crack region, which includes the initiation and propagation phase, and the fracture region.

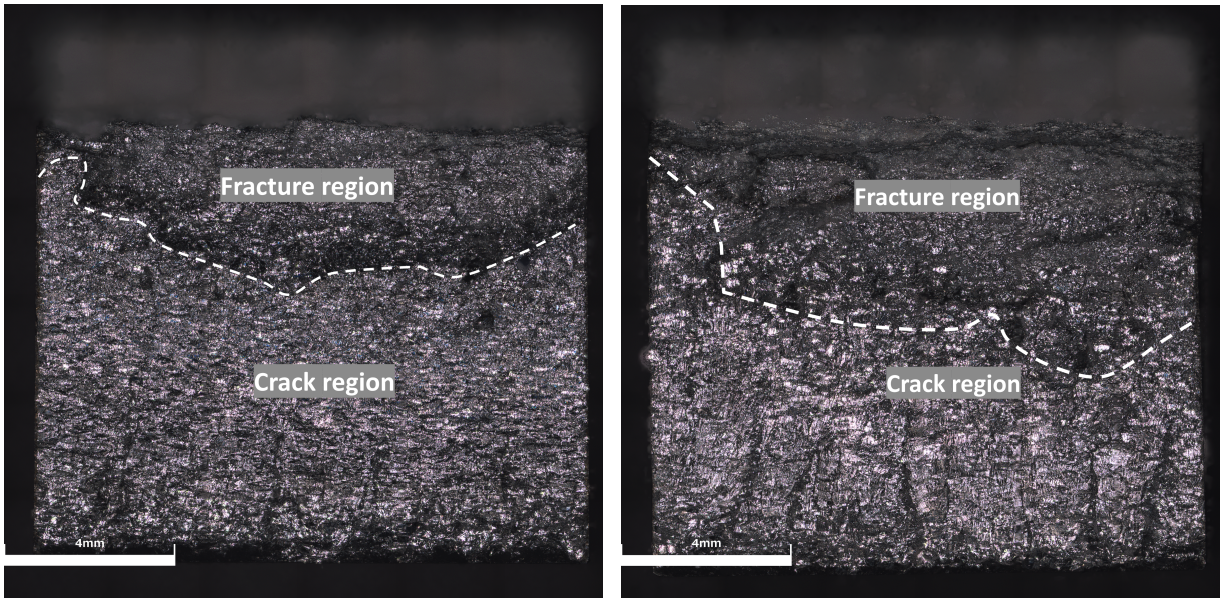

((a)) 5 mm overhang ((b)) 13 mm overhang

Figure 4.13: Crack and fracture surfaces

The main measurement that can be taken from this in the confocal microscope is the crack inclination. For this, 3 profile lines are traced in the the region closer to the contact and away from the fracture region, that means, where the crack initiates. As an example, Figure 4.14 shows how the inclination can be measured, and all the measurements can also be found in the Appendix.

From this measurement it was possible to see that for the $5\ mm$ overhang, the average inclination is $\theta = 21.2°$ and for the $13\ mm$, $\theta = 12.2°$. No obvious reason can be given to the inclination difference.

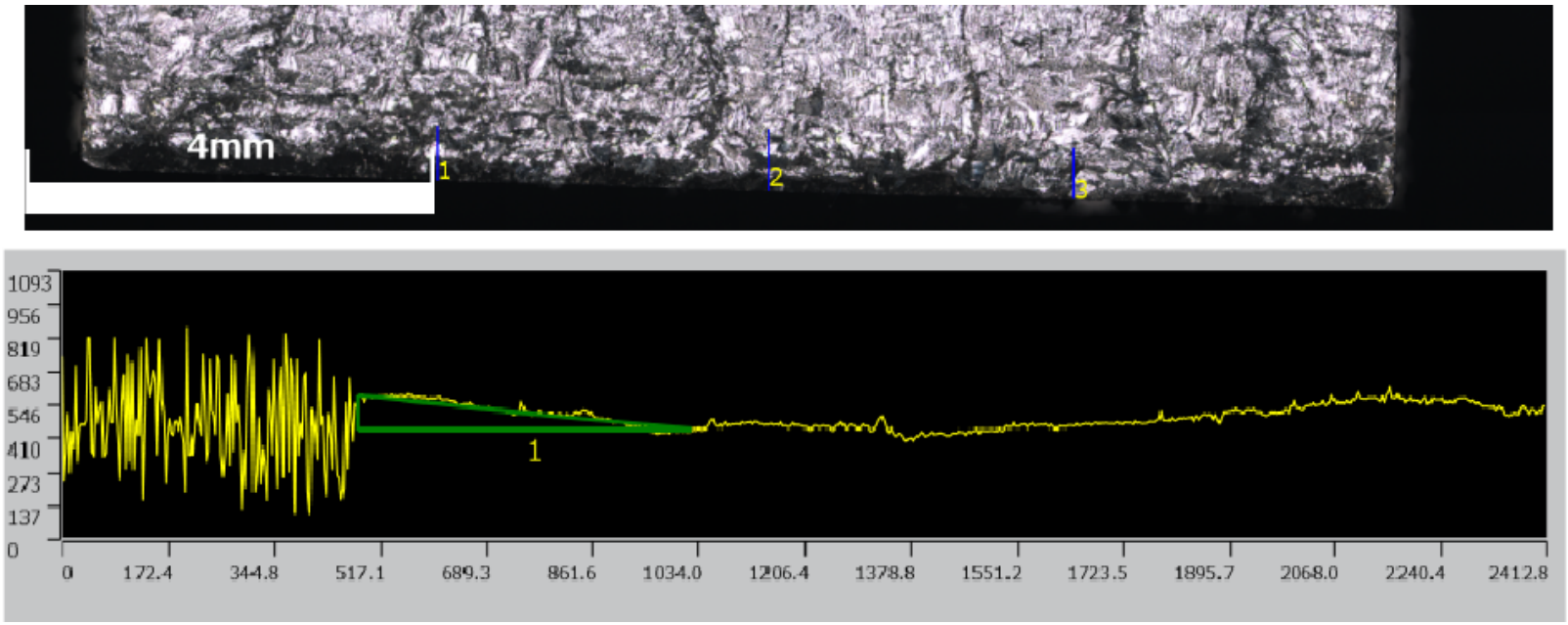

Figure 4.14: Example of inclination measurement

Chapter 5

Stress analysis and life estimate for different pad overhang

This chapter's goal is to have a minute discussion over the procedure taken to estimate life of a mechanical contact under fretting fatigue loading and evaluate pad deformation. In here it is discussed the step-by-step procedure of stress analysis performed with the commercial finite element method software, the critical point search and then the application of the Theory of critical distance line method to estimate fretting fatigue life, the last two by means of the Smith-Watson-Topper parameter.

Hence, the chapter is divided into 3 sections. One regarding the FEM analysis, the other the critical point finding and lastly the iterative line method with critical distance varying in function of life. It is worth noting that this procedure focus on highlighting the differences for analyzing the pad overhang length as shown by the schematics of the Figure 5.1. In the figure, the pad support is represented by the black bars, and the overhang can be changed by cutting the pad length or by changing the diameter of the steel rollers that are positioned between the support and the pad to guarantee an even pressure distribution.

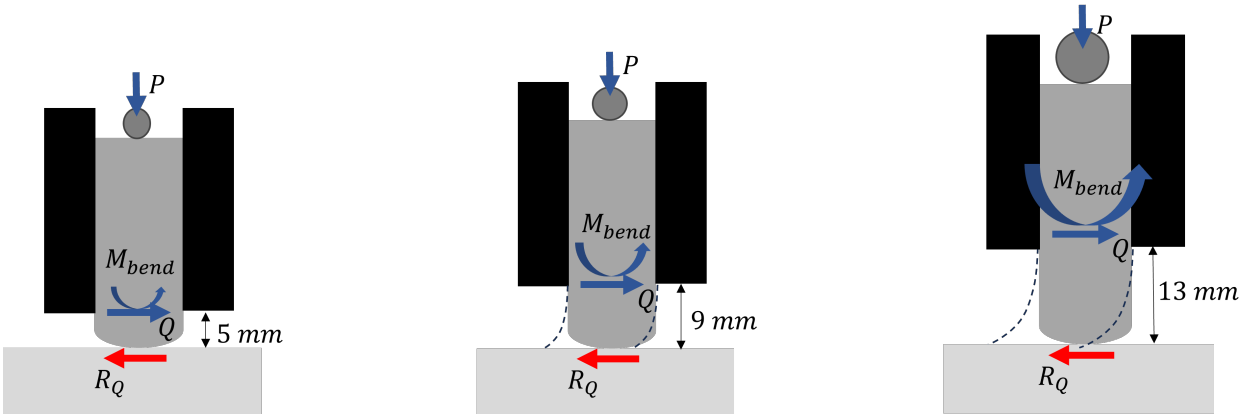

Figure 5.1: Pad overhang schematics for 3 different overhang sizes

5.1 Finite Element Method Analysis

The finite element method is a type of numerical analysis where the object of study, being it a complex mechanical component, a fluid or fluid filled volume, a building structure or a thermal mass can be modeled as a finite amount of smaller pieces that are easier to calculated them the entire object. These small pieces are connected together and applying correctly the loads and the boundary conditions it is possible have an approximation of the real variables of interest of that problem.

It is obvious that there is a trade-off between how many pieces there are and the time to compute them. So a good FEM analysis can give a good enough approximation to understand and to predict the phenomenon and also be fast enough to be used in an academic context or even faster in an industrial one.

The basic concept of finite element analysis, although not the only numerical method that uses it, is the meshing of a continuous object. The method traces back to the 1940s and from them a whole lot of researches developed and rediscovered it all over the planet. Robust mathematical basis were published on 1970s with Strang and Fix (1973). The author also recommends the works from Hughes (1987) for practical learning of the method and Wriggers and Laursen (2006) for computational contact mechanics.

It is out of the scope of this work to present the mathematical basis for FEM and numerical contact mechanics, thus, from now on, an user friendly procedure used on the commercial software ABAQUS 6.14 applied to fretting fatigue will be explained.

5.1.1 Fretting fatigue FEM in ABAQUS

ABAQUS is a well known finite element commercial software created by HKS and now owned by Dassault Systèmes, under the subgroup SIMULIA, well reputed on the computational software industry. It is very used for stress analysis of mechanical components and the simulations held for this work were performed in licensed workstations at the University of Brasília.

5.1.1.1 Problem modeling

ABAQUS has a very straightforward interface in terms of step-by-step modeling. In the first tab, the Part tab, two shell 2D parts were modeled, one for the pad and one for the specimen. It is shown in the Figure 5.2 the dimensions and the assembly positioning of the parts. Note that the pad height will concern the pad overhang configuration which we are studying. The dimensions of the problem are the same as the real problem, except for the length of the specimen that is cut of due to fatigue load being applied far away from the contact.

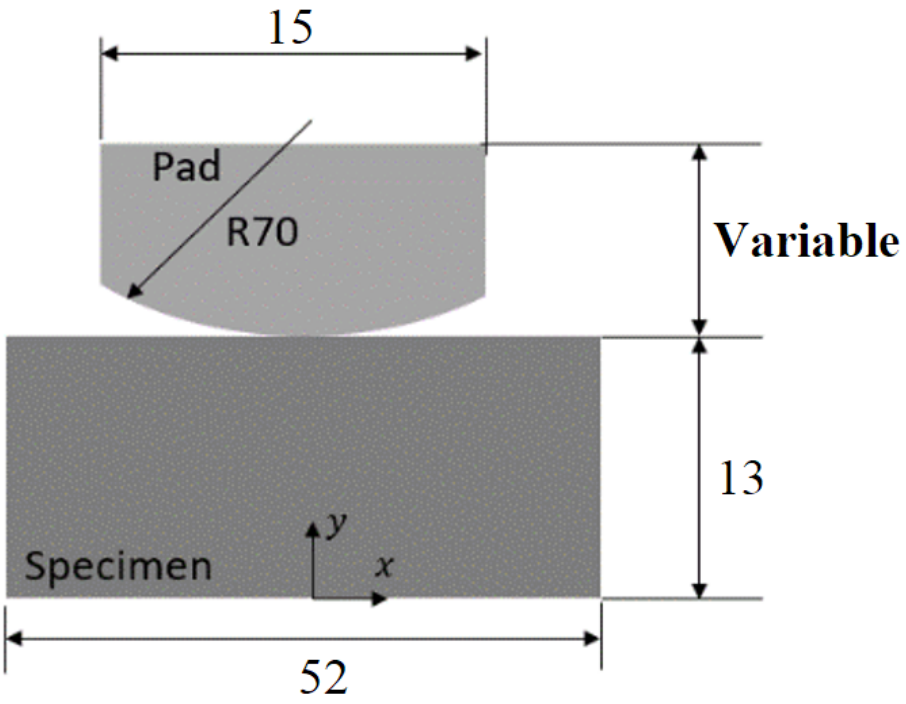

Figure 5.2: Part dimensions and positioning

5.1.1.2 Material Properties

In Properties Tab, we must assign the material and the section of each parts. As both parts are the same material, just one section and one material were created. As the fatigue analysis is made outside ABAQUS by a external code, the properties needed are just the Elasticity modulus and the Poisson Ratio. As shown in Chapter 4, these properties are respectively, $70000\ MPa$ and 0.33. Note that in ABAQUS the stress/pressure variables are assigned as MPa, so we can keep all variables in the Newton and millimeter system, hence, pressure is N/mm^2, which is MPa.

For the section assignment, it is possible to determine a thickness to our model. As we performed a 2D analysis, the thickness was set to $1\ mm$ so we can attribute the loading in the N/mm form.

5.1.1.3 Assembly tab

For the Assembly tab, the only requirement is to insert the parts and to position them. As the parts were drawn in the configuration and position of the Figure 5.2, the assembly does not take much time for this problem. The meshing of the assembly was chosen to be dependent, so in the mesh section the problem is meshed as a whole instead as part by part separately.

5.1.1.4 Step tab

In the Step section, the steps of the problem are created. By default each step has 1 time unit (we shall call it seconds). The steps created for the problem were divided by each loading as follows:

1. Remote step: in this step the average bulk load is applied to the specimen part. Also, a small vertical displacement is set to the pad so it does not slip over the specimen when loading.
2. Normal load step: in this step the normal load is applied to the pad part in direction of the specimen.
3. Cyclic load step: in this step, two full sinusoidal cycles are set to tangential and fatigue load. These two are taken so any temporal characteristics of fretting loading are disregarded on the next step.
4. Analysis step: in this, one full cycle of the fretting fatigue phenomenon is taken. The stresses on this step are the ones taken for the post processing. The step was manually set to 32 increments so the post-processing is more refined.

The Figure 5.3 shows how the loads are applied in function of each step.

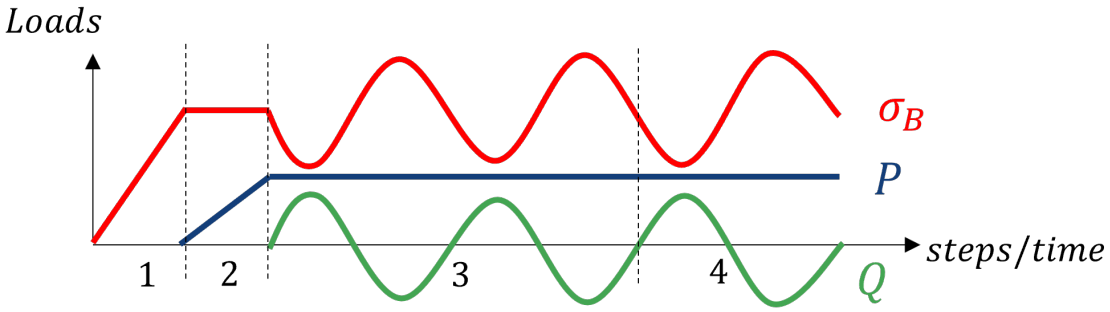

Figure 5.3: Step evolution graphic

5.1.1.5 Interaction tab

The interaction is a very important step of modeling the problem because in it we define the contact properties of our problem. Besides that, we also create and assign the reference points to control the loads. The references points are two. One is the master for the pad top edge and it represents the pad support starting from where the pad is considered "free" from the contact of the support. The second one is connected to the right specimen edge and is on it that the fatigue load is applied. Figure 5.4 shows the reference points interactions to their respective edges and the master and slave contact surfaces/edges.

Contact interaction

As Fretting is a contact phenomenon, the correct definition of the contact interaction is crucial for obtaining good results. Below are the most important definitions along with their justifications. Much of the information presented here can be found in the ABAQUS documentation (DS SIMULIA, 2023a).

- Master and slave surfaces: In contact finite element analysis, it is common for the component that receives loads to be defined as the master, and components that are more static and are secondary exposed to the loads to be defined as the slave (Figure 5.4). Thus, the pad is defined as the master component and the test specimen defined as the slave.
- Global contact search: ABAQUS by default has an initial step in which it performs an exhaustive global search for possible contacts in the model. New global searches are performed every 100 iterations, and are therefore not necessary for the model in question (DS SIMULIA, 2023a).
- Local search: The local contact search was defined as node-to-segment. The other possible choice would be segment-to-segment. The first is less computationally expensive and applies the force of a node in the master surface to the segment of an element in a punctual way. Although segment-to-segment is a more refined and distributes the nodal pressure to the segment in a linear manner, the contact region was refined enough to not affect precision of the model.
- Sliding condition: Within the contact definition, the sliding condition must be specified as either finite sliding or small sliding. Small sliding was defined because the sliding is very small compared to the whole problem since in fretting the sliding is partial.
- Normal contact restraint formulation: In this option, the type of contact restraint formulation is defined as a property of the contact interaction. It was defined as "rigid" contact, in which the contact penetration is minimized. Within this, the augmented Lagrange formulation was chosen, which is a hybrid formulation between the penalty method and the Lagrange multiplier method.
- Tangential contact behavior formulation: Here, the friction condition of the contact is defined. Governed by the Coulomb-Amontons Law, the Lagrange multiplier formulation was defined, in which the contact reaction is calculated exactly compared to the penalty method, which is an approximation. In this definition is where ABAQUS receives the friction coefficient of the material, in which for the Al-7075-T651 is $f = 0.6$.

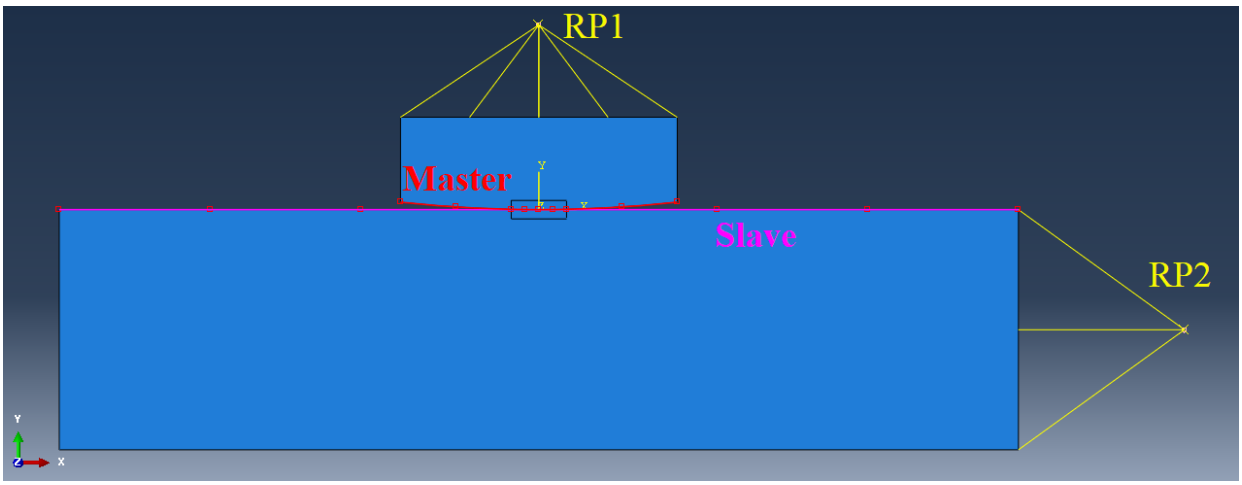

Figure 5.4: Interaction viewport from ABAQUS

5.1.1.6 Load tab

In the Load tab is where the problem takes its shape because in it is applied all the loads and set the boundary conditions. Figure 5.5 shows a summary of the loads and boundary conditions as they are explained subsequently. In total, it was applied 4 loads and 4 boundary conditions.

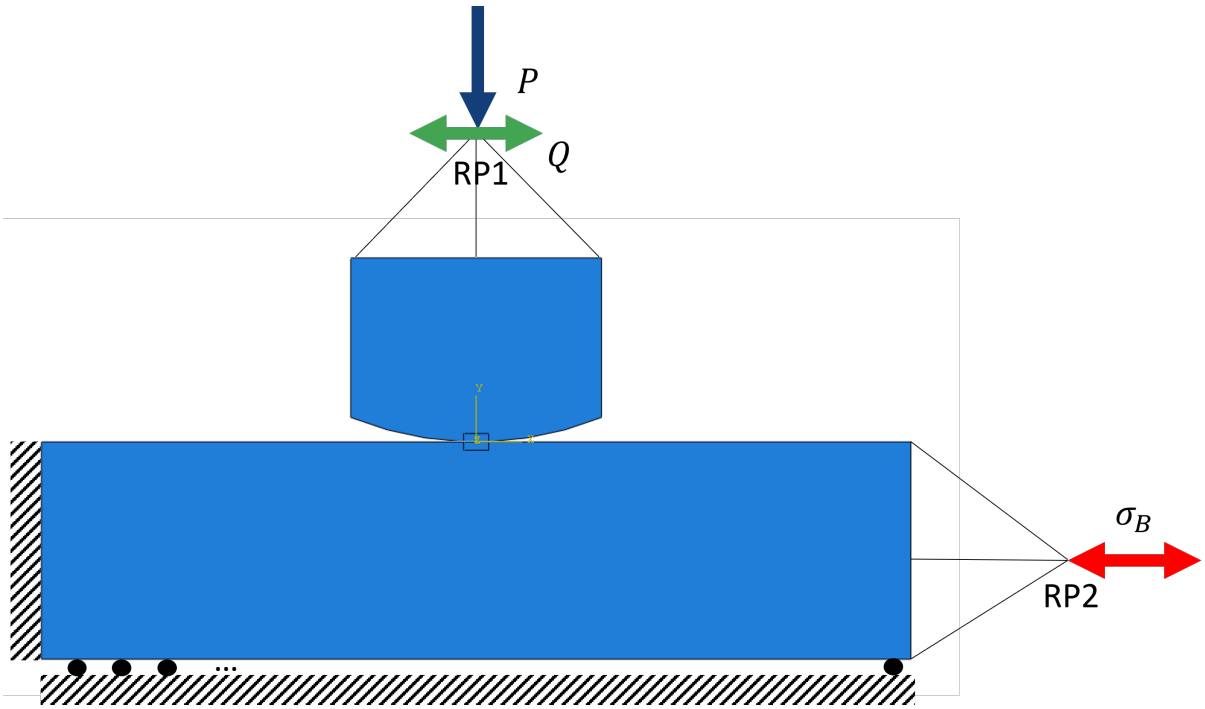

Figure 5.5: Load and boundary conditions schematics

Loads

As aforementioned, 4 loads were applied to the model. They are set as shown in Table 5.1, in accordance to Figure 5.3.

Table 5.1: Load application process

Load	Magnitude	Steps			
		1	2	3	4
Normal Load, P	$-400\ N/mm$	-	Ramp	Propagated	Propagated
Tangential fretting load, Q	$160\ N/mm$	-	-	2 Cycles	1 Cycle
Mean Bulk load, B_m	$650\ N/mm$	Ramp	Propagated	Propagated	Propagated
Cyclic Bulk load, B_a	$-794.5\ N/mm$	-	-	2 Cycles	1 Cycle

It is worth noting that the minus sign in the Normal Load, P, is regarded to it being compressive, and down to the vertical axis. Also, the minus sign in the Cyclic bulk load, B_a, means that it is loaded 180° out-of-phase, opposite direction from the tangential fretting load, Q.

Boundary conditions

In total, 4 boundary conditions (BC) were applied to the model. All boundary conditions are applied in all steps of the model, with exception to boundary condition 4, which is a prescribed displacement meant to avoid the sliding during the application of Mean Bulk load, B_m. They are described as following:

1. Fixing of left specimen edge: The edge is restricted both directions x and y and to rotate around z axis. In ABAQUS, directions are set, respectively as 1,2 and 3. This BC regards the fretting machine grip that is fixed. Lastly, this boundary can be duplicated to the right edge if no remote load is desired.

2. Support of bottom specimen edge: in this boundary condition the bottom edge is fixed in direction y. This is considered equal to the fretting apparatus where one of the pads can be substituted by a roller bearing. It doesn't affect the phenomenon since fretting fatigue over 10^5 is mainly a crack initiation problem.

3. Non rotation of Reference point 1: This is considered by the author one of the most important BC. This boundary condition fixes the rotation of RP1 meaning it can only move in translation. It is related to the consideration that the fretting apparatus machine deformation is much smaller than the one from the pad, so in the model can be set as fully rigid. The separation of the effect of pad deformation, as well as its systematic testing is the differential of this work, as opposed to the works from Erena et al. (2022) and Vantadori et al. (2023).

4. Separation of pad when applying B_m: when applying the Mean bulk load, a small prescribed vertical displacement, of $0,0001mm$, is set to RP1 so the small deformation of the specimen do not cause any tangential load to the pad rather them the prescribed load Q. Depending of the model, ABAQUS may need that this BC is set back to its original place before the step 2.

5.1.1.7 Mesh tab

The last modeling tab is the Mesh tab, where we divided our continuous model into small elements so the finite element analysis can be computed. The steps to be taken on this is to draw a partition on each part of our model so we can have a refined region on the contact zone. Later, it is needed to define the elements size, called "to seed" the model, where is possible to determine the space between elements or the number of nodes per edge or surface. Finally it is very important to set the element type on our regions so the analysis makes sense of what we are studying.

For the partition, this model only requires a small rectangle to be draw where the pad enters in contact with the specimen. Both parts have a more refined contact region. Figure 5.6 shows what the mesh is suppose to look like. The partition dimension for the loads applied accordingly Table 5.1 have a height and length of around 0.5 and 3 times (respectively) the semi contact width, a, which is approx. $a = 0.95mm$. Thus, the dimensions are $0.5mm$ and $3mm$.

Regarding sizing and element type, the global mesh is set as free quadratic elements so it can gradually be more refined towards the contact. The global elements are set to have around 0.8 mm and it gets smaller until $0.01mm$, where it finds the refined contact mesh. This mesh is not as important as the contact one and may be changed for a better performance and convergence control in ABAQUS.

The contact refined mesh is the more important one as it will be set as the Area of interest when calculating the stresses and the fatigue life methodology. It is set as structured quadratic elements with fixed size of $0,005mm$.

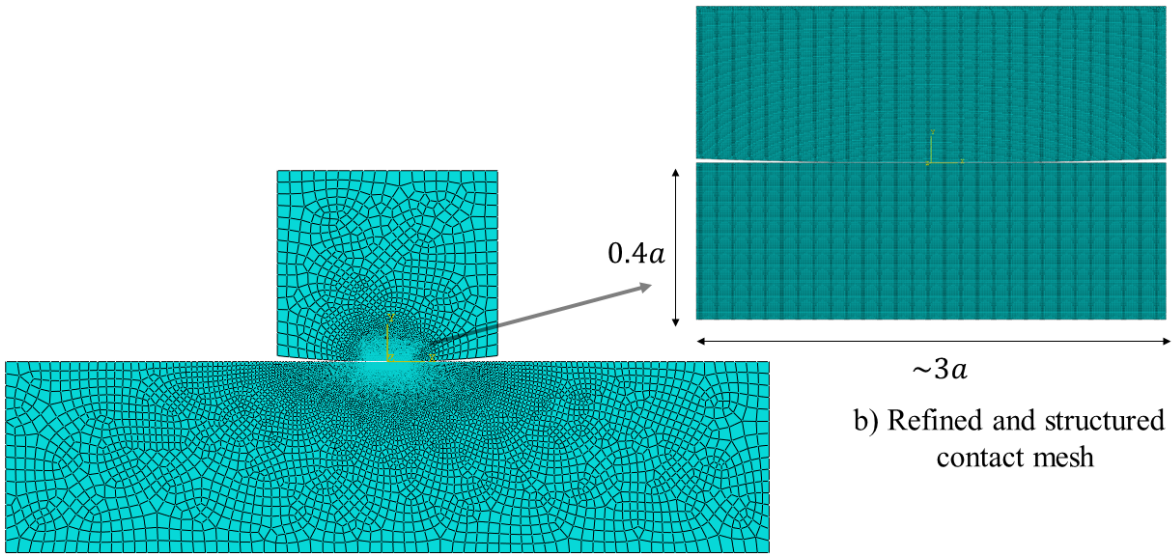

Figure 5.6: a) Global mesh and b) Refined contact mesh

At last, a important step is to defined the element type for the model. It is set as a standard element type of solution for the element, rather than explicit. The family is **set to plane strain**. Setting it to plane strain is important because the plane strain state is the one inside and at the center of the specimen, where the crack is expected to nucleate which have a slightly higher stress than plane stress one, that regard the stresses at the free surface. At last, the integration type was set to reduced for performance. The ABAQUS documentation (DS SIMULIA, 2023b) shows that this element is called **CPS4R**.

5.2 Search of critical point

Once the FEM analysis is done by ABAQUS the next procedure is to use the output file from it to find the Critical Point, in other words, the point where the stresses or the fatigue parameter is maximum.

For the purpose of extracting the stresses from ABAQUS odb. file it was used a Python code, produced by Professor Rafael Cardoso (2024), from Universidade Federal do Rio Grande do Norte, and adapted by the author. The code may be found in the Appendix. It returns one .txt with the undeformed position of each element and one file for each stress in the Cauchy's stress tensor. For the stresses files, each row is for a element and each columns for a increment time. As said in the ABAQUS FEM section, 5.1, the analysis step has 32 increments.

To run the code, a main python function has to call the extracting code aforemantioned, which opens ABAQUS, that has an great interaction with Python. The code is like the following:

```
import os
import time

start = time.time()

flag = os.system('abaqus CAE noGUI=extracting_stress.py')

end = time.time()
print(end - start)
```

Now, we have all the stresses from the area of interest which was defined as the contact zone of the specimen. After that, it has to be run another code that computes the SWT fatigue parameter for every element to define the hotspot. This was made by the author via a code in the language MatLab. The code may be found in the Appendix.

As fretting is a contact problem, the author decided to search for the critical only in the contact region and only in the surface, since its where the crack would nucleate. In general, hotspots are in the surface, unless the component has high a residual stress.

At the end of this code run, the code defines where is the hotspot of the area of interest, in

the case, the contact area. Figure 5.7 show a example graph of the SWT distribution over each element in horizontal direction x of the contact surface. The one with the largest SWT parameter is considered to be the hotspot.

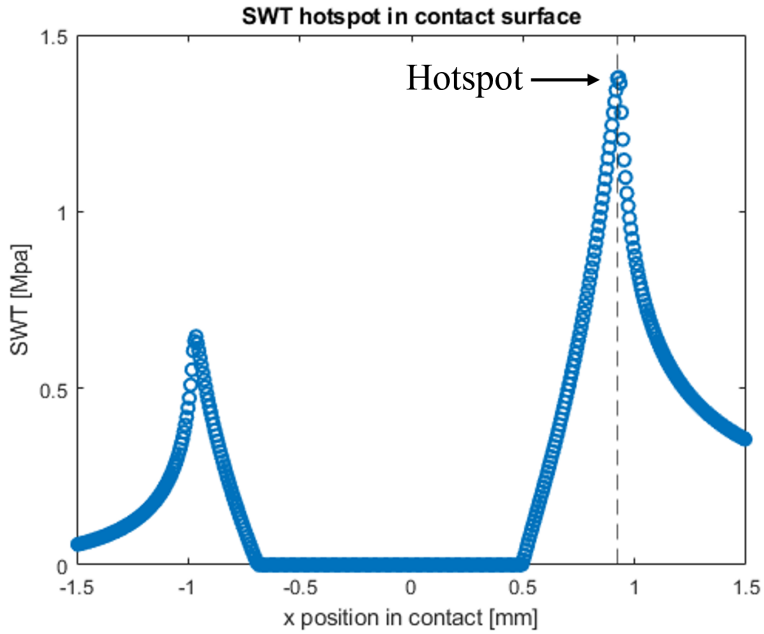

Figure 5.7: Example of the SWT stresses in the contact surface and hotspot location

Summarizing this procedure:

1. Compute the SWT for each element of the surface.
    1.1. To compute SWT it is needed to calculate the normal stresses for a range of θ from $0°$ to $179°$ as the the opposite half of the full circle result in the complementary plane: $\boldsymbol{n}(0° \text{ to } 180°) = -\boldsymbol{n}(180° \text{ to } 360°)$.
    1.2. Store the SWT(θ) Maximum for each element of the surface.
2. Find the element on which SWT(element) is maximum.

5.3 Iterative TCD line method

In this section it is explained the iterative procedure to estimate fretting fatigue life along with the called variable critical distance. Hence, the first thing is to determine the relation that connects the variable critical distance to the estimated life.

5.3.1 Relation between L-N_f

As said before, independently of what small length is considered to be the initiation crack, for high cycle fatigue the initiation life and total life tend to be the same. In a previous work (RESENDE, 2023), a procedure in which the propagation lives of cylindrical specimens were subtracted of the SWT-total life curve for the Al 7075-T651 taken by NIMS (FURUYA et al., 2019). Figure 5.8 shows a graph that confirms that from 10^5 on, the initiation and total lives can be considered the same. Hence, for this work a procedure similar to the one used to estimate the initiation life on Rangel, Erena Guardia et al. (2022) and Resende (2023) is used to estimate now total life, if the estimated total life is $N_f > 10^5$.

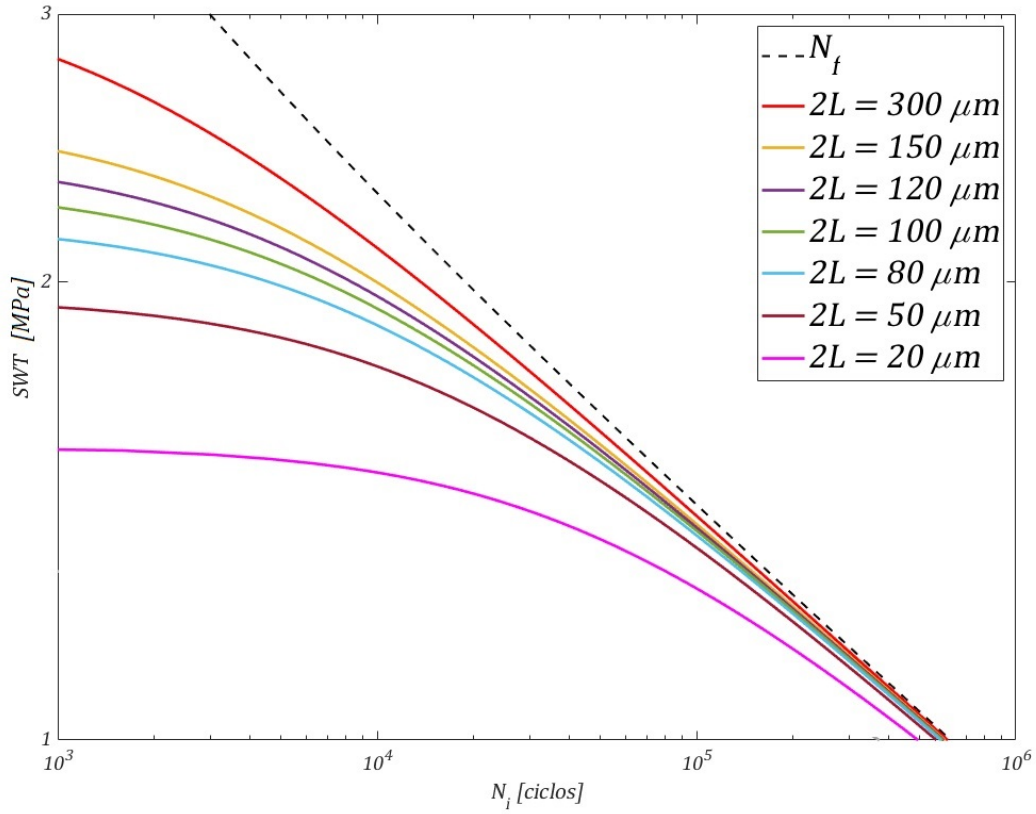

Figure 5.8: Curves of SWT in terms of initiation life for different initiation lengths. (RESENDE, 2023)

With that clarified, it is possible to approximate a curve of the length L in fuction of total life N_f from the work of Pinto (2022). In his work, he calculated the two critical lengths from Eqs. 2.19 and 2.20, $L_S = L(N_f = 1)$ to be $L_S = 662\ \mu m$ and $L_\infty = L(N_f = 10^6)$ to be $L_S = 19.5\ \mu m$, for a approximate loading ratio of $R = 0.1$, the one used for the loading as shown is section 5.1.1.6.

The linear log-log equation as shown in Figure 2.7, is then:

$$L = L_S(N_f)^{\frac{log(L_\infty/L_s)}{log(10^6)}} = 0.662(N_f)^{-0.2551}\ [mm] \tag{5.1}$$

5.3.2 Relation between SWT-N_f

Next step is to determine the relation between SWT and total life. This is made by manipulating the Basquin and Basquin-Coffin-Mason Equations (2.1 and 2.4) with the SWT strain based equation in case of linear elastic mechanics (Eq. 2.10) and we arrive at:

$$SWT = \frac{\sigma_f^{'2}}{E}(2N_f)^{2b} + \sigma_f^{'}\varepsilon_f^{'}(2N_f)^{b+c} \tag{5.2}$$

where $\sigma_f^{'}$ and b are the coefficient and exponent of fatigue strength, respectively, $\varepsilon_f^{'}$ and c are the coefficient and exponent of fatigue ductility, respectively, E is the modulus of elasticity, and N_f is the life for total separation of the test specimen. The Al 7075-T651 properties will be the ones in Table 4.3, the same as the ones used by Pinto (2022), taken from Boller and Seeger (2013) work.

5.3.3 The line method associated with FEM stresses

This is the process to calculate the SWT parameter over the line of characteristic length $2L$ when taking the stresses from the FEM analysis. This may be a complicated process because we only know the stresses at the centroid of each element in the FEM. However, due to Matlab native function "griddata" (MATHWORKS, 2024), it is possible to map any point of a 2D variable field for any arbitrary point you want by natural interpolation (C^1 Continuity). The Figure 5.9 is a schematic that helps guide us through the process.

Once we get a hotspot point we can start our TCD line method calculation. The process starts with a guess critical distance L_G. Then, for each θ [in increments of 1° limited from 0 to 15° due to results from previous works, Resende (2023) and Pinto (2022)] that we desire to calculate, we divide the line with $2L_g$ length into 40 points. It is worth noting that a small L_G passes through at least 8 element centroid points, which guarantee a smooth continuous stress curve.

The coordinates in the 40 points are taken in regard to x and y directions and each stress component of the Cauchy's stress tensor is defined via Matlab's Griddata function. This stress variables are given in respect to the time increment (on a full fretting fatigue cycle with 32 increments), hence:

$$\text{Tensor:}\quad \boldsymbol{\sigma} = function(1:40\,points, t-1:32)$$

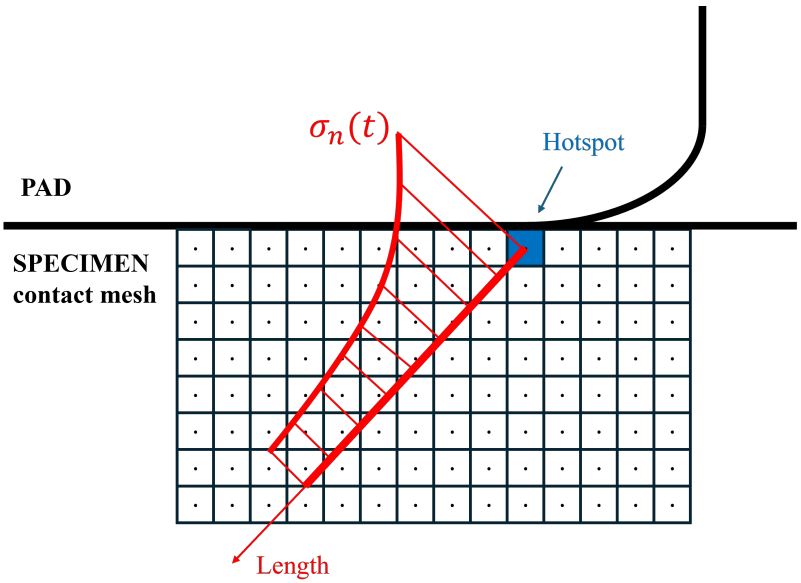

Figure 5.9: TCD line method with FEM schematic

Each point has a corresponding normal stress σ_n, all of them are distributed as a continuous function, as shown in Figure 5.9 by the red function over the axis length. For each time increment, the numerical integral of all those point is taken and divided by $2L_G$ so we have the average normal stress over the line for a given time, as in Eq. 2.13:

$$\bar{\sigma_n} = function(t)$$

where the bar represents the average value. Figure 5.10 shows how the average is taken by numerical integral over the $2L$ length.

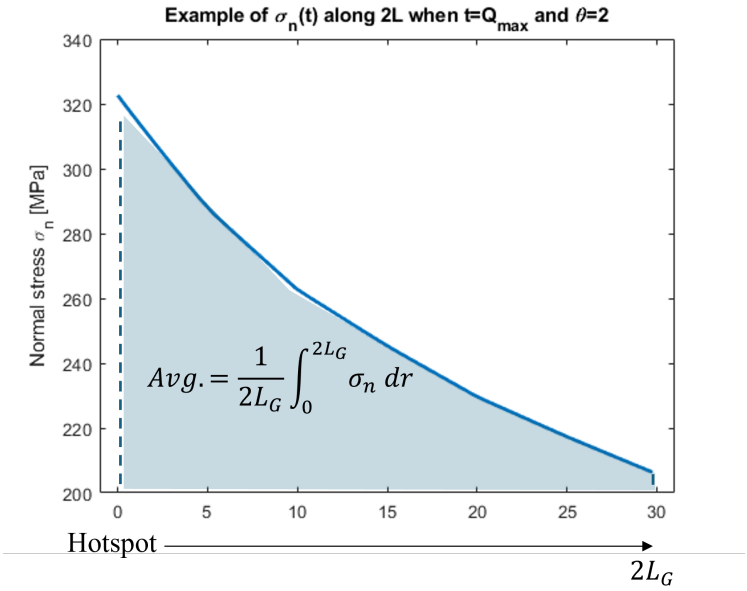

Figure 5.10: Example of $\sigma_n(t)$ along $2L_G$ when $t = t(Q = Qmax)$ and$\theta = 2°$.

Hence, at this point, for each time we have a corresponding average normal stress. With them, we can calculate a maximum average value over the line by Eq. 2.14 and a amplitude of the average by Eq. 2.15:

$$\sigma_{n,max}(\theta) = \max_t(\sigma_n(\theta, t)$$

and

$$\sigma_{n,a}(\theta) = \frac{1}{2}[\max_t(\sigma_n(\theta, t) - \min_t(\sigma_n(\theta, t)]$$

Lastly, once we have $\bar{\sigma_{nmax}}$ and $\bar{\sigma_{na}}$, it is possible to apply the Eq. 2.10.

$$SWT = \max_\theta \left\{ \sigma_{n,max}(\theta) \frac{\sigma_{n,a}(\theta)}{E} \right\}$$

Keeping the SWT value for each θ, in the end is possible to determine the maximum SWT in respect to θ for that given L_G that we started with.

5.3.4 Iterative algorithm to estimate life

Finally, with all the relations defined, we can implement the iterative algorithm. Now, it is possible to calculate the length $2L$ and inclination θ of the critical distance , the value of the SWT parameter, and the prediction of the fretting fatigue life N_f.

All the relations form a system of equations, so a numerical calculation is necessary to determine these variables. It is used an iterative approach based on the bisection method (BURDEN; FAIRES, 1985). The flowchart shown in Fig. 5.11 illustrates the step-by-step process, similar to the one applied in Resende (2023). The main difference is that now the life is considered total life, and that, instead of computing the stress via analytical means, the stresses come from FEM analysis.

In the flowchart, first, we assume a critical distance $2L_G$, with the initial value being the average between $2L_S$ and $2L_\infty$. Using the stresses originated by the ABAQUS's output file, the average stresses along the length line $2L_G$ are calculated over time, as explained in the last section. This is repeated for the inclinations of θ in order to determine the maximum SWT_G parameter and consequently, the critical plane and crack direction. The total life N_G associated with the critical length L_G is calculated from the SWT-N_f curve (Eq. 5.2).

Next, with N_G, a new characteristic length L is calculated using Eq. 5.1, and consequently the critical distance $2L$ as well. If L and L_G are within tolerance, the procedure stops; otherwise, the procedure is repeated with L_G being a function of L and the possible interval being reduced by half (bisection method). The steps are repeated until convergence. These calculations were performed in Matlab, and the codes of this process may be found in Appendix.

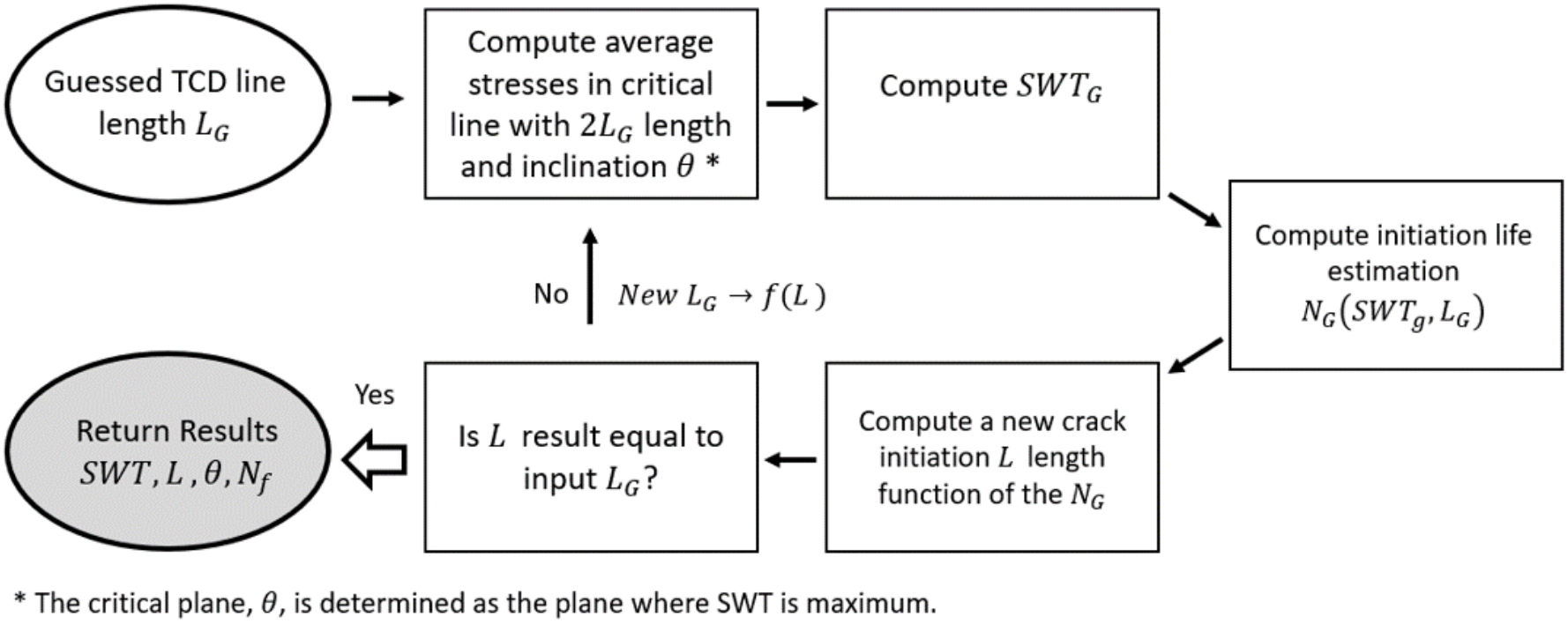

Figure 5.11: Flowchart of iterative method for fretting fatigue method

Chapter 6

Results and discussion

This chapter is focused on presenting the results clearly, along with the discussions and conclusions drawn out of the work presented until now. First it is presented the pad compliance difference between FEM analysis with different overhangs. Second, we determine the difference in hotspot point for the pad overhang. Lastly, and most important we show the difference in life estimations and experimental, including the well known and used analytical solution estimate based on Chapter 3.

6.1 Pad deformation

The schematics of pad overhang indicates, in Figure 5.1, that as overhang length between pad support and contact surface increases, the bending moment applied to the pad also increases. Calculated bending moments for different pad overhangs are shown in the following Table 6.1.

Table 6.1: Bending moment for different pad overhang lengths

Pad overhang length	**Bending moment**
$5\ mm$	10.4 Nmm
$9\ mm$	18.7 Nmm
$13\ mm$	27.7 Nmm

Hence, as expected, this bending moment increases linearly with the overhang distance. With this increase in moment, even tough for metal alloys the deformation in not particularly visible, the thesis from this work is that a different pad overhang can cause a non-negligible life difference when we account all the nonlinearities from the life estimate process, with special regards to the known Basquin and Baquin-Coffin-Mason equations (2.1, 2.4) that are in logarithmic scale.

The first thing it is worth checking is if a visible deformation and contact movement can be seen from the finite element analysis. Figure 6.1 shows* the normal pressure distribution along

the contact of the FEM results and also a close up of point in which contact is detected. In the Figure 6.1 it was plotted for the 3 overhang lengths the pressure distribution in two moments of the fretting load, one in the time increment on which the tangential load is maximum, $Q = Q_{max}$, and other when $Q = Q_{min}$, which is the maximum in the opposite direction.

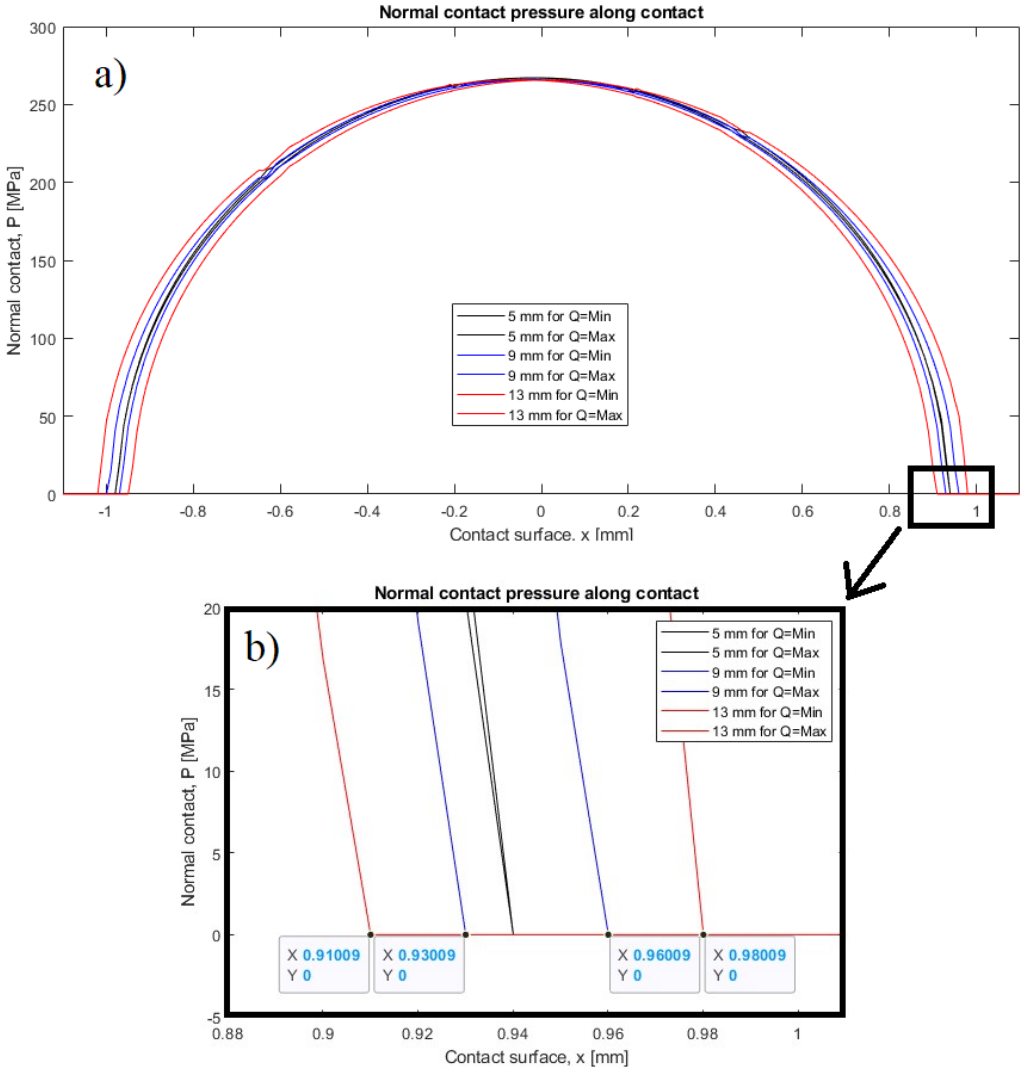

Figure 6.1: a) Pressure distribution over the full contact; b) Close-up of the contact limit

Figure 6.1.a) shows that for the $5\ mm$, the black line basically overlap each other, hence it can be said that for maximum and minimum load of Q the contact for $5\ mm$ overhang do not move. For the $9\ mm$ overhang, it is seem that the two blue lines surround the black line, one at maximum and another at minimum tangential loading, showing that a small contact movement is happening. At last, in red is possible to see clearly that for $13\ mm$ overhang a noticeable contact movement is happening from the separation of the red lines in each moment.

The Figure 6.1.b) shows the contact limit zoomed in so we can quantitatively measure contact movement, which is regarded to the pad deforming in the FEM analysis. As we can see, the 5 mm black lines basically overlap each other from where the contact starts. For it to match the

analytical solution presented in Chapter 3 it is needed that the overhang tend to a value closer to 0. The blue lines, for $9\ mm$, are separate in an amount of $0.03\ mm$ or $30\ \mu m$. As the contact semi-width is $a = 0.96\ mm$, the full contact has $2a = 1.92\ mm$, so the contact movement is 1.6%. For the red lines the movement is greater, around $0.08\ mm$ or $80\ \mu m$, which translate to a contact movement of 4.2%. Both contact movements are small and the peak pressure value, p_0, do not change, but as said, this cannot discard a different life estimate due to all nonlianearities of the problem.

6.2 Hotspot Position

Following, the next step then is to calculate the SWT parameter all over the surface and find the hotspots and also, confirm if any change in the SWT will be translated to a different life estimate. Thus, as example of the Figure 5.7 in the Section 5.2 showed, after acquiring the hotspot for all overhang lengths we can plot the surface SWT as shown in Figure 6.2.

From the Figure 6.2.a) it is possible to see that the SWT are not the same for the different overhangs although they are close. Hence, it was need to have a zoom from the area around what is the theoretical contact trailing edge, or semi-width a, calculated by Equation 3.6. Figure 6.2.b) is the zoomed area. From it can be drawn that the hotspot changes, going in direction of the interior of the contact as the overhang increases. The hotspot for $5\ mm$ is almost exactly as the theoretical one, as for the $9\ mm$ and the $13\ mm$, they are bit to the side.

Besides that, the SWT values also change with the overhang. They increase with the increase of the overhang as shown in Figure 6.2.b). The Table 6.2 shows the values for the hotspot of each overhang as well as the SWT maximum value at the contact surface. It can be seem that the SWT maximum can change from 5 to 10 %. Since, $SWT - N_f$ curve is not linear, then it can be said that the lives for different pad overhangs may significantly change.

Table 6.2: Maximum SWT at surface hotspot

Pad overhang length	**Hotspot** $(x\ position)$	$\boldsymbol{SWT_{max}}$	**Difference to 5 mm**
5 mm	0.904 mm	1.38 MPa	-
9 mm	0.923 mm	1.46 MPa	5.5 %
13 mm	0.929 mm	1.52 MPa	9.2 %

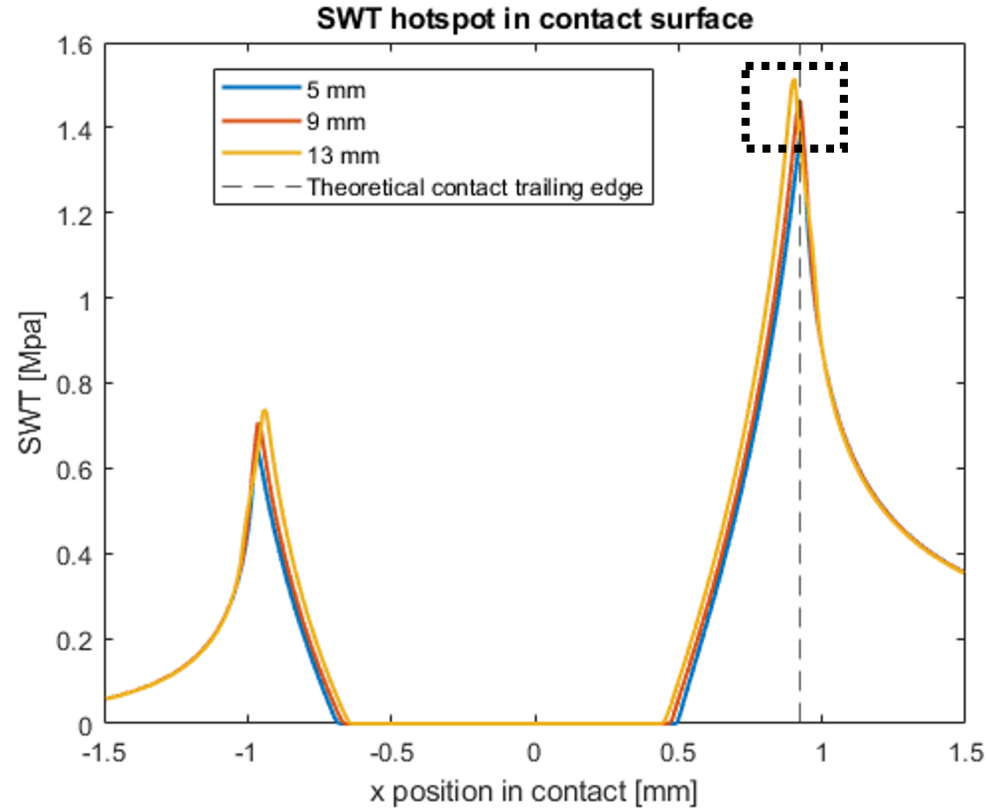

((a)) SWT distribution

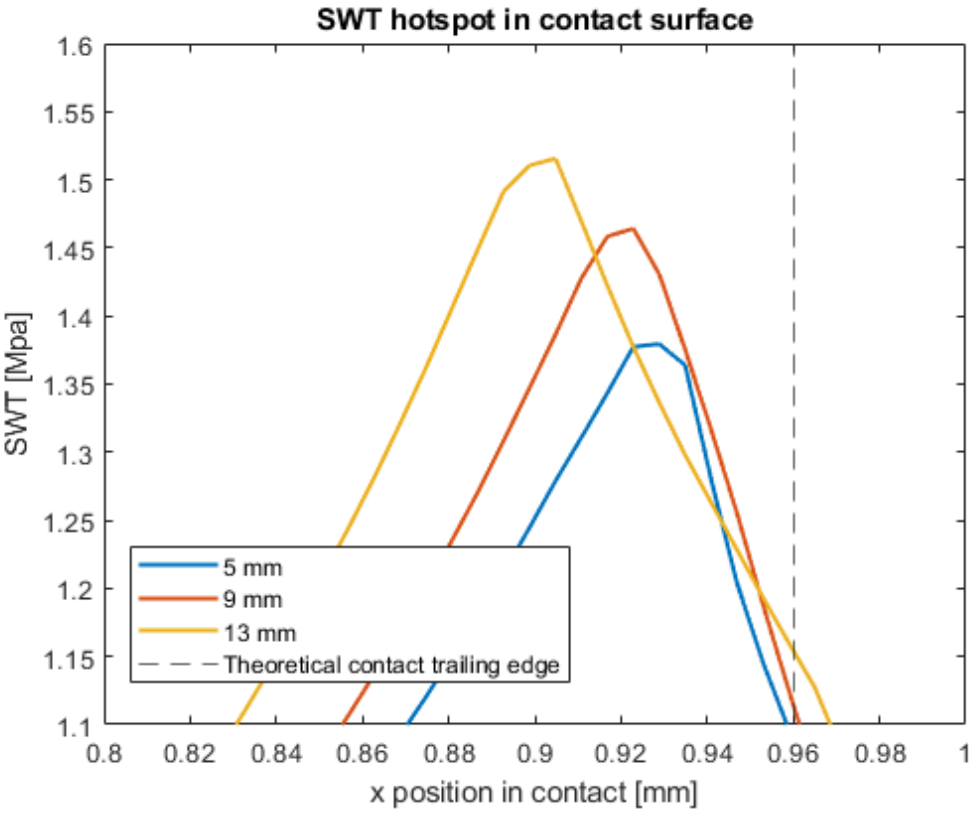

((b)) Zoomed graph of the hotspot region

Figure 6.2: Maximum SWT for each element on the Contact surface

6.3 Life estimates for different pad overhangs compared to experimental life

Once it was acquainted the distinction in hotspot position and SWT fatigue parameter, as following the methodology of the last Chapter 5, the last step is to apply the iterative Theory of Critical Distance Line method and estimate lives for fretting fatigue. The Figure 6.3 shows the lives for different pad overhangs coming from the FEM analysis and the also very important analytical solution, in which no lateral pad deformation exists. The procedure for the analytical stresses and line method can be found in depth in Erena Guardia et al. (2022) and Resende (2023).

From Figure 6.3, taking the analytical estimate as the base one, it can be seen that the 5 mm that had almost no pad deformation has a life only 4% smaller. As for the 9 mm, the estimated life is 13.4% less than the expected with the analytical. These two values are considered non-negligible already. Nonetheless, the difference due to 13 mm overhang to the base one is 24.5% less. This shows that the small changes from last section in hotspot and SWT values show a bigger difference on the estimated lives when compared to the analytical one. It is obvious that this difference will depend of how great is the tangential load responsible for pad deformation, but in any case, this pad overhang is accountable in a considerable form to life estimate.

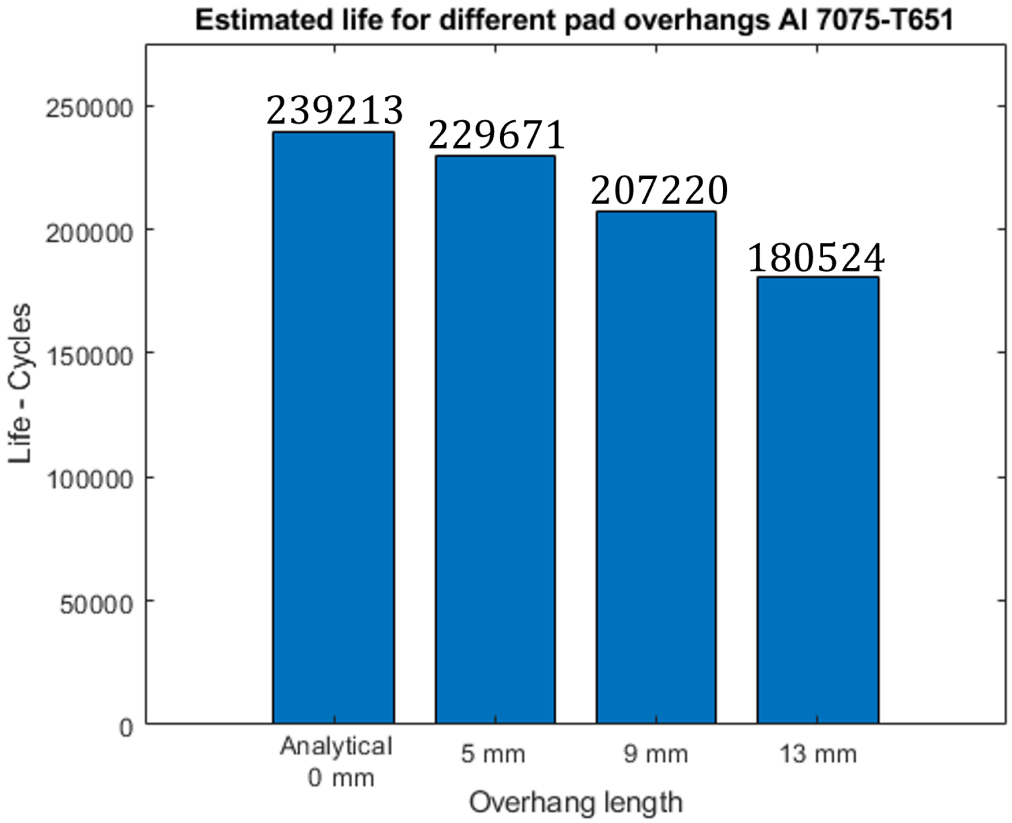

Figure 6.3: Estimated lives for different pad overhangs

The values from the estimated lives where considerable enough to be tested out in a

experimental campaign as seen in Chapter 4's, Section 4.3.1. With all the data gathered from Analytical estimate, FEM estimates, and experimental fretting fatigue analysis, the Table 6.3 was created to summarize the estimated fatigue parameter SWT, critical distance length L, line orientation θ and life N_f and the last two columns the experimental lives of tests carried out.

From the Table 6.3, is possible to conclude that the SWT over the line is smaller than the ones at maximum, which is obvious, but the trend that the SWT increases when the overhang increases is the same. With respect to SWT_{line} of the analytical solution, $5\ mm$ overhang, $9\ mm$ and $13\ mm$ are respectively 1.0% , 3.6% and 7.8% higher. These values although smaller than the difference between SWT from the hotspot still generated considerable life difference when comparing the estimated lives for different pad overhangs to the analytical solution. The L length and inclination θ are mostly the same for the loads applied for these estimates.

Moreover, it is worth comparing the contact size, the crack nucleation position (hotspot) and the crack inclination with the microscopic estimates (Section 4.4). It can be seen that in the microscopic results, the contact size is higher for the experimental estimates, being it around 30% and 75% higher, respectively for the $5\ mm$ and the $13\ mm$, and this difference may be attributed to machine compliance. The experimental inclination is also higher, in both $5\ mm$ and $13\ mm$, $4\times$ and $2\times$, respectively. As for the crack initiation point, the amount of which each one goes towards the center of the contact is around 10% for experimental, compared to 3%, 4% and 6% from the 5,9 and 13 mm estimates (respectively), but it is not possible to affirm that the trend of it going more towards the inside of the contact with a higher overhang is true.

The average experimental lives show that from estimated analytical, $5\ mm$ experimental life was 13.6% smaller than the analytical estimated, the $9\ mm$ was 16.2% smaller and $13\ mm$ was 37.5%. This amount show that not considering the overhang used to carry the fretting fatigue tests can relate to a great difference in lives. The pad used in the University of Brasília has 15 mm in width. A great amount studies have Pad's with a smaller section area and may be more susceptible to deformation.

Now, comparing the estimates with their respective experimental lives, it can be said that the methodology captures well the trend that the increase in the overhang decreases FF lives. As shown in Table 6.3, $5\ mm$ is 8.96% smaller than its estimate, as $9\ mm$ and $13\ mm$ are, respectively, 3.31% and 17.13% smaller. This show great correspondence of methodology applied to the studied problem. To even further the analysis, it can be said that the slightly bigger divergence in the bigger overhang can be due to a portion of the deformation be from the machine apparatus. Consequently, the consideration of a rigid fretting apparatus is not completely true, as shown by fretting test Section 4.3.1, that when trying to carry out tests with a greater overhang of $20\ mm$ the Pad and support flange suffered from fretting wear and resulted in a cracked Pad.

Lastly, to summarize, the most important regard is that no experimental test was more than twice or less than half the estimated life from the proposed methodology, which in fatigue we consider inside scatter band of 2, and a great result. Also, this confirms that the consideration

of the pad overhang is very important when analyzing fretting fatigue tests, with differences up to 37.5% compared to the often used analytical solution. It is then recommended by the author that the pad overhang should be indeed decrease to a minimum. However, as already said, when carrying out tests with the DIC camera system or with the high temperature igniter, a distance of at least $9\ mm$ should exist between contact surface and pad support so these equipment can fit. Therefore, the present work results will come in hand when carrying out those type of tests and highlighting the importance of accounting for the pad deformation.

Table 6.3: Estimate and experimental lives results

Overhang	**Hotspot**	SWT_{line}	**L length**	θ_{line}	**Estimated life**	**Test**	**Experimental life (error to estimated)**	**Experimental Avg. (error to estimated)**
Analytical - 0 mm	(0.96 , 0.0)	0.9076 MPa	28.1 μm	5°	239213	-	-	-
5 mm	(0.93 , 0.0)	0.9167 MPa	28.5 μm	5°	229671	FF-05-01 FF-05-02	193437 (-15.8%) 224749 (-2.14%)	209093 (-8.96%)
9 mm	(0.92 , 0.0)	0.9401 MPa	29.2 μm	6°	207220	FF-09-01 FF-09-02	139263(-32.8%) 261442(+26,2%)	200352 (-3.31%)
13 mm	(0.90 , 0.0)	0.9785 MPa	29.6 μm	6°	180524	FF-13-01 FF-13-02 FF-13-03	142219 (-21.2%) 141548 (-21.6%) 165022 (-8.59 %)	149596 (-17.1%)

Chapter 7

Conclusions

In this Master's dissertation it was presented a hybrid methodology to estimate total life in components under fretting high-cycle fatigue. This methodology used stresses from finite element ABAQUS commercial software instead of the usual analytical solution for fretting fatigue. This is because the main thesis in the present work was to evaluate the distance between pad support and the contact surface in fretting, so called pad overhang. The greater this pad overhang is, the greater is the pad deformation due to tangential loading, and this deformation was supposed to meaningfully affect fretting fatigue life. The analytical solution does not account for lateral deformation of the contacting components, and this can generate an error up to 37%. The methodology improves significantly the studied of fretting fatigue and that can lead to more reliable live estimates for aircraft components.

After the FEM analysis, the stresses were extracted from ABAQUS output file via Python integration. These stresses were used to calculate if there were any changes in the critical point/hotspot position and in Smith-Watson-Topper fatigue parameter, both regarding the stresses when pad deformation is occurring. It is possible to say, that meaningful differences were regarded about both position and fatigue stress history in the hotspot, that, when considering the nonlinearities of the Fretting fatigue phenomenon, could cause a significant life difference.

Furthermore, from the hotspot analysis, it was applied the Theory of critical distance's Line method to estimate the life. These calculations were performed using Matlab commercial software since its graphic interface and functions documentation are very useful. The characteristic length size was determined as variable with total estimated life, as the most recent works have been doing, instead of being a fixed material property.

The main conclusion from the FEM analysis and TCD line method was concerning the estimated life. It showed that the increase in the pad overhang generated a lesser life in fretting fatigue. One of the main reasons for that can be the contact not being fixed, generating a loading and unload effect closer to the trailing edge of the contact, and this loading and unloading might generate a larger stress amplitude over the contact edge and below it. The life estimate can change

down to 37% less for the $13\ mm$ overhang than the same analysis done via analytical means. The author recognizes that this change in life is also function of the tangential load, although the analysis was made with $Q/P = 0.4$, leaving room to further increase fretting loading until ratio is equal to the friction coefficient, $Q/P = f = 0.6$, of the Aluminum alloy.

The last analysis left to do was to validate the methodology and what was found from the estimated life with experimental data. As the scientific method states, a systematic experimental campaign was carried out to evaluate real changes of the pad overhang. The experimental data showed us the same trend: that increasing overhang decreases fretting life. In general, the estimates not only indicate the trend well but also have a great precision. They showed that no average experimental data had more than a 18% difference from the estimates. In addiction, the greater difference was regarded to the bigger $13\ mm$ overhang, which can be explained by deformation in the fretting apparatus, that although very rigid, the completely rigid boundary condition is not possible in reality.

So, to the extend of this work, all specific objectives were fully completed. The FEM analysis was performed, and the stresses were extracted from ABAQUS, the hotspot position variation was captured, the iterative routine was applied and the life estimates were corroborated by the experimental results. This shows a robust work developed by this Master's dissertation, in which the author can affirm that to consider the proper overhang on simulations with over $5\ mm$ is imperative for a proper fretting fatigue life estimation. This may be true for all future works on which is intended to use the DIC system or the High temperature apparatus.

7.1 Future works

As future works to advance this methodology, the author recommends to apply the analysis for different materials, as Titanium and INCONEL alloy, since both are susceptible to high temperature tests. Other validation may be using different geometrical dimensions as different pad radii and different loading cases, to further improve the herein results. A last possibility should be to utilize the DIC camera system to capture the real deformation including the fretting apparatus compliance.

References

AL ZAMZAMI, I et al. The critical distance method to estimate the fatigue strength of notched additively manufactured titanium alloys. **Procedia Structural Integrity**, Elsevier, v. 28, p. 994–1001, 2020.

ALBERT, Wilhelm A.J. Über Treibseile am Harz. Archiv für Mineralogie Geognosie Bergbau und Hüttenkunde, vol. 10, pp 215-34, 1838.

ALCOA. Alloy 7075 Plate and Sheet. **Alcoa Mill Products: SPD 10-037**, 2001.

ALMEIDA, GMJ et al. Four actuators fretting fatigue rig and tests with cyclic normal load for Ti-6Al-4V. **Theoretical and Applied Fracture Mechanics**, Elsevier, v. 119, p. 103292, 2022.

ARAUJO, JA; NOWELL, DJIJOF. The effect of rapidly varying contact stress fields on fretting fatigue. **International Journal of Fatigue**, Elsevier, v. 24, n. 7, p. 763–775, 2002.

ARAÚJO, JA; ALMEIDA, GMJ, et al. Early cracking orientation under high stress gradients: The fretting case. **International Journal of Fatigue**, Elsevier, v. 100, p. 611–618, 2017.

ARAÚJO, JA; CASTRO, FC, et al. Life prediction in multiaxial high cycle fretting fatigue. **International Journal of Fatigue**, Elsevier, v. 134, p. 105504, 2020.

ARAÚJO, JA; SUSMEL, L; PIRES, MST, et al. A multiaxial stress-based critical distance methodology to estimate fretting fatigue life. **Tribology International**, Elsevier, v. 108, p. 2–6, 2017.

ARAÚJO, JA; SUSMEL, L; TAYLOR, D, et al. On the use of the Theory of Critical Distances and the Modified Wöhler Curve Method to estimate fretting fatigue strength of cylindrical contacts. **International journal of fatigue**, Elsevier, v. 29, n. 1, p. 95–107, 2007.

BASQUIN, OH. The exponential law of endurance tests. In: PROC Am Soc Test Mater. [S.l.: s.n.], 1910. v. 10, p. 625–630.

BOHÓRQUEZ, L et al. On the prediction of the crack initiation path in fretting fatigue. **Theoretical and Applied Fracture Mechanics**, Elsevier, v. 99, p. 140–146, 2019.

BOLLER, Chr; SEEGER, T. **Materials Data for Cyclic Loading: Aluminium and Titanium Alloys**. [S.l.]: Elsevier, 2013. v. 42.

BURDEN, Richard L; FAIRES, J Douglas. 2.1 The bisection algorithm. **Numerical analysis**, PWS Publishers, p. 46–52, 1985.

CARDOSO, RA. Código em Python para extração de tensões no ABAQUS. **Universidade do Rio de Janeiro**, 2024.

CASTRO, FC. Modelos de Plano Crítico para Fadiga Multiaxial de Alto Ciclo. **Class notes - Fadiga em metais - UnB**, 2011.

CATTANEO, Carlo. Sul contatto di due corpi elastici: Distribuzion local degli sforzi. Reconditi dell Accademia nazionale dei Lincei, 1938.

CHENG, WHST et al. Micromechanics modeling of crack initiation under contact fatigue, 1994.

CHU, C-C. Fatigue damage calculation using the critical plane approach, 1995.

DOWLING, N.E. **Mechanical Behavior of Materials: Engineering Methods for Deformation, Fracture, and Fatigue**. [S.l.]: Pearson, 2013. ISBN 9780131395060. Available from: <https://books.google.com.br/books?id=IKcHvgAACAAJ>.

DS SIMULIA. **ABAQUS documentation: 12.4 Defining contact in ABAQUS/Standard**. Available from: <https://classes.engineering.wustl.edu/2009/spring/mase5513/abaqus/docs/v6.6/books/gsa/default.htm?startat=ch12s04.html>. Visited on: 10 June 2023.

_____. **ABAQUS documentation: 4.1 Element formulation and integration**. Available from: <https://classes.engineering.wustl.edu/2009/spring/mase5513/abaqus/docs/v6.6/books/gsa/default.htm?startat=ch04s01.html>. Visited on: 14 June 2023.

ERENA, Diego et al. Influence of the rolling of contact pads on crack initiation in fretting fatigue tests. **International Journal of Fatigue**, Elsevier, v. 163, p. 107087, 2022.

ERENA GUARDIA, Diego et al. A fretting fatigue model based on self-steered cracks. **Theoretical and Applied Fracture Mechanics, 117, 103144.**, Elsevier BV, 2022.

FATEMI, Ali; SOCIE, Darrell F. A critical plane approach to multiaxial fatigue damage including out-of-phase loading. **Fatigue & Fracture of Engineering Materials & Structures**, Wiley Online Library, v. 11, n. 3, p. 149–165, 1988.

FORMAN, RG; SHIVAKUMAR, V. Fracture Mechanics, 17. **ASTM STP**, v. 905, 1986.

FURUYA, Yoshiyuki et al. Catalogue of NIMS fatigue data sheets. **Science and Technology of Advanced Materials**, Taylor & Francis, v. 20, n. 1, p. 1055–1072, 2019.

GOMES, Rodrigo C et al. Fatigue life prediction using critical distance on aluminum alloy wire containing indentation produced marks. **Theoretical and Applied Fracture Mechanics**, Elsevier, v. 128, p. 104135, 2023.

HERTZ, Heinrich. Ueber die Berührung fester elastischer Körper. Walter de Gruyter, Berlin/New York Berlin, New York, 1882.

HILLS, D.A.; NOWELL, D. **Mechanics of Fretting Fatigue**. [S.l.]: Springer Netherlands, 1994. (Solid Mechanics and Its Applications). ISBN 9780792328667. Available from: <https://books.google.com.br/books?id=t9Q60-N-13MC>.

HUGHES, Thomas JR. **The finite element method: linear static and dynamic finite element analysis**. [S.l.]: Dover Publications, 1987.

JIANG, Yanyao; HERTEL, Olaf; VORMWALD, Michael. An experimental evaluation of three critical plane multiaxial fatigue criteria. **International Journal of Fatigue**, Elsevier, v. 29, n. 8, p. 1490–1502, 2007.

LACZKO, Peter. **Fretting of interference fitted shaft**. Available from: <https://slideplayer.com/slide/10926940/>. Visited on: 25 Jan. 2023.

LAMACQ, Valérie; BAIETTO, Marie-Christine. Modelling of initial fatigue crack growth and crack branching under fretting conditions. **Fatigue and Fracture of Engineering Materials and Structures**, v. 22, n. 6, p. 535–542, 1999.

LAMACQ, Valérie; DUBOURG, Marie-Christine; VINCENT, Léo. A theoretical model for the prediction of initial growth angles and sites of fretting fatigue cracks. **Tribology International**, Elsevier, v. 30, n. 6, p. 391–400, 1997.

MATHWORKS. **Matlab documentation - Help**. Available from: <https://www.mathworks.com/help/>. Visited on: 10 Jan. 2024.

METTU, SR et al. NASGRO 3.0: A software for analyzing aging aircraft. In: Pt. 2. THE Second Joint NASA/FAA/DoD Conference on Aging Aircraft. [S.l.: s.n.], 1999.

MINDLIN, Raymond David. Compliance of elastic bodies in contact. American Society of Mechanical Engineers, 1949.

MUSKHELISHVILI, Nikolaĭ Ivanovich et al. **Some basic problems of the mathematical theory of elasticity**. [S.l.]: Noordhoff Groningen, 1953. v. 15.

NAVARRO, Carlos; VÁZQUEZ, Jesús; DOMÍNGUEZ, Jaime. A general model to estimate life in notches and fretting fatigue. **Engineering Fracture Mechanics**, Elsevier, v. 78, n. 8, p. 1590–1601, 2011.

NEU, Richard W; PAPE, John A; SWALLA, Dana R. Methodologies for linking nucleation and propagation approaches for predicting life under fretting fatigue. In: FRETTING fatigue: current technology and practices. [S.l.]: ASTM International, 2000.

NOWELL, D; DINI, D; HILLS, DA. Recent developments in the understanding of fretting fatigue. **Engineering fracture mechanics**, Elsevier, v. 73, n. 2, p. 207–222, 2006.

NOWELL, David. **An Analysis of Fretting**. 1988. PhD thesis – The University of Oxford, Lincoln College, Oxford, UK. Available at https://ora.ox.ac.uk/objects/uuid:61c9f75d-7c81-4280-9997-91f6e79543fb/files/mceb9a67b5bd04e39d194ebdea55050ef.

NTSB, National Transportation Safety Board -. Aloha Airlines, Flight 243, Boeing 737-200, N73711. **Aircraft Accident Report AAR-89/03**, 1989.

_____. Left Engine Failure and Subsequent Depressurization Southwest Airlines Flight 1380, Boeing 737-7H4, N772SW. **Aircraft Accident Report AAR-19/03**, 2019.

NYE LUBRICANTS. **Fight Fretting with Rheotemp™ 769G**. Available from: <https://www.nyelubricants.com/fight-fretting-with-rheotemp%5C%E2%5C%84%5C%A2-769g>. Visited on: 25 Jan. 2023.

OLIVEIRA, Giorgio André Brito; CARDOSO, Raphael Araújo; JÚNIOR, Raimundo Carlos Silverio Freire; ARAÚJO, José Alexander. A generalized ANN-multiaxial fatigue nonlocal approach to compute fretting fatigue life for aeronautical Al alloys. **Tribology International**, Elsevier, v. 180, p. 108250, 2023.

OLIVEIRA, Giorgio André Brito; CARDOSO, Raphael Araújo; JÚNIOR, Raimundo Carlos Silverio Freire; DOCA, Thiago, et al. On the generalization capability of artificial neural networks used to estimate fretting fatigue life. **Tribology International**, Elsevier, v. 192, p. 109222, 2024.

OLIVEIRA, Giorgio André Brito; JÚNIOR, Raimundo Carlos Silverio Freire, et al. A hybrid ANN-multiaxial fatigue nonlocal model to estimate fretting fatigue life for aeronautical Al alloys. **International Journal of Fatigue**, Elsevier, v. 162, p. 107011, 2022.

PARIS, Paul C. A rational analytic theory of fatigue. **Trends Engin**, v. 13, p. 9–14, 1961.

PINTO, AL et al. Fretting fatigue under variable amplitude shear loading blocks considering partial slip regime: Experimental/numerical analysis. **Tribology International**, Elsevier, v. 182, p. 108367, 2023.

PINTO, André Luis. **Fretting fatigue under variable amplitude loading**. Sept. 2022. PhD Dissertation – University of Brasilia and KU Leuven, Example City, CA. Available at https://example.com/thesis.pdf.

RESENDE, Danilo RS. **ESTIMATIVA DE VIDA SOB CONDIÇÕES DE FRETTING PARA LIGA AL 7075-T651**. Feb. 2023. Engineering degree project – University of Brasilia, UnB, Asa Norte, Brasília DF.

RUIZ, C; CHEN, KC. Life assessment of dovetail joints between blades and discs in aero-engines. **Mechanical Engineering Publications,** p. 187–194, 1986.

SMITH, KN; WATSON, P; TOPPER, TH. Stress-strain function for the fatigue of metals. **J mater**, v. 5, n. 4, p. 767–778, 1970.

SOCIE, D. Multiaxial fatigue damage models. **Journal of engineering materials and technology**, v. 109, n. 4, p. 293–298, 1987.

STRANG, Gilbert; FIX, George. **An Analysis of the Finite Element Methods, and Engineering**. [S.l.]: Prentice Hall.Inc, 1973.

SUSMEL, Luca. The theory of critical distances: a review of its applications in fatigue. **Engineering Fracture Mechanics**, Elsevier, v. 75, n. 7, p. 1706–1724, 2008.

SUSMEL, Luca; LAZZARIN, P. A bi-parametric Wöhler curve for high cycle multiaxial fatigue assessment. **Fatigue & Fracture of Engineering Materials & Structures**, Wiley Online Library, v. 25, n. 1, p. 63–78, 2002.

SZOLWINSKI, Matthew P; FARRIS, Thomas N. Mechanics of fretting fatigue crack formation. **Wear**, Elsevier, v. 198, n. 1-2, p. 93–107, 1996.

TAYLOR, David. Geometrical effects in fatigue: a unifying theoretical model. **International Journal of Fatigue**, Elsevier, v. 21, n. 5, p. 413–420, 1999.

_____. The theory of critical distances. **Engineering Fracture Mechanics**, Elsevier, v. 75, n. 7, p. 1696–1705, 2008.

VANTADORI, Sabrina et al. Effect of rolling on fretting fatigue assessment of cylindrical contact in partial slip regime. **Tribology International**, Elsevier, v. 188, p. 108772, 2023.

VÁZQUEZ, J; NAVARRO, C; DOMÍNGUEZ, J. Analysis of fretting fatigue initial crack path in Al7075-T651 using cylindrical contact. **Tribology International**, Elsevier, v. 108, p. 87–94, 2017.

WATERHOUSE, RB. Fretting wear. **Wear**, Elsevier, v. 100, n. 1-3, p. 107–118, 1984.

WOHLER, August. Theorie rechteckiger eiserner Brückenbalken mit Gitterwänden und mit Blechwänden. Zeitschrift für Bauwesen. 5: 121–166, 1855.

_____. Über die Festigkeitsversuche mit Eisen und Stahl. Zeitschrift für Bauwesen. 20: 73–106, 1870.

WRIGGERS, Peter; LAURSEN, Tod A. **Computational contact mechanics**. [S.l.]: Springer, 2006. v. 2.

Appendix

Python code to extract stresses from ABAQUS .obd file

```
# Reading field outputs (stress) and element centroid positions from ABAQUS odb #
# R. A. Cardoso Adapted By Danilo R.S. Resende

## Importing libraries ##

from abaqus import *
from abaqusConstants import *
from caeModules import *
from driverUtils import executeOnCaeStartup
executeOnCaeStartup()
import numpy as np

## Input data ##

cwd = os.getcwd()


odb_name = cwd +'\\Pad_h_5mm.odb' # path odb

part_name = 'CP-1' #  name of the part evaluated

set_name = part_name + '.AOI' # set selected for extracting field data (upper cas

dim = 2 # Problem's dimension (2 or 3)

odb = session.openOdb(name=odb_name) # Opening odb file

## Selecting stress components in the region of interest (In this example:
## SET-STRESS, which was pre-defined on the ABAQUS model) ##

session.viewports['Viewport: 1'].setValues(displayedObject=odb)

SXX = session.xyDataListFromField(odb=odb, outputPosition=ELEMENT_CENTROID, ...
variable=(('S', INTEGRATION_POINT, ((COMPONENT, 'S11'), )), ), elementSets=(set_name, ))
```

```
35
36 SYY = session.xyDataListFromField(odb=odb, outputPosition=ELEMENT_CENTROID, ...
37 variable=(('S', INTEGRATION_POINT, ((COMPONENT, 'S22'), )), ), elementSets=(set_name, ))
38
39 SZZ = session.xyDataListFromField(odb=odb, outputPosition=ELEMENT_CENTROID, ...
40 variable=(('S', INTEGRATION_POINT, ((COMPONENT, 'S33'), )), ), elementSets=(set_name, ))
41
42 SXY = session.xyDataListFromField(odb=odb, outputPosition=ELEMENT_CENTROID, ...
43 variable=(('S', INTEGRATION_POINT, ((COMPONENT, 'S12'), )), ), elementSets=(set_name, ))
44
45 nel = len(SXX) # number of elements in the selected region
46
47 ## Removing repeated time data ##
48
49 time = [0.0]
50
51 time_id = [0]
52
53 for i in range(1,len(SXX[0].data)):
54
55     if SXX[0].data[i][0] != SXX[0].data[i-1][0]:
56
57         time.append(SXX[0].data[i][0])
58
59         time_id.append(i)
60
61 time = np.array(time)        # time instants
62
63 nt = len(time)               # number of time instants
64
65 ## Defining "empty" arrays to store stress components over time for each element ##
66
67 POS = np.zeros((nel,dim))     # Position elements centroid
68
69 Sxx = np.zeros((nel,nt))      # sigma_xx components
70
71 Syy = np.zeros((nel,nt))      # sigma_yy components
72
73 Szz = np.zeros((nel,nt))      # sigma_zz components
74
75 Sxy = np.zeros((nel,nt))      # sigma_xy components
76
77 ## Filling arrays ##
78
79 for i in range(nel):
80
81     # Determining centroid coordinates for each element #
```

```
82
83      name = SXX[i].name; id1 = name.find('E:'); id2 = name.find('Centroid')
84
85      elem = int(name[id1 + 3:id2 - 1])
86
87      conn = odb.rootAssembly.instances[part_name].elements[elem - 1].connectivity
88
89      pos = np.array([odb.rootAssembly.instances[part_name].nodes[node-1].coordinates ...
90  ... [:dim] for node in conn])
91
92      POS[i,:] = np.mean(pos,axis = 0)
93
94      # Storing stress components over time for each element #
95
96      for k, idk in enumerate(time_id):
97
98          Sxx[i,k] = SXX[i].data[idk][1]
99
100         Syy[i,k] = SYY[i].data[idk][1]
101
102         Szz[i,k] = SZZ[i].data[idk][1]
103
104         Sxy[i,k] = SXY[i].data[idk][1]
105
106 ## Saving arrays ##
107
108 tfr = np.nonzero(time == 4.0)[0][0]
109
110 np.savetxt(cwd + '\\time.txt',time[tfr:] - 4.0)
111 np.savetxt(cwd + '\\Sxx.txt',Sxx[:,tfr:])
112 np.savetxt(cwd + '\\Syy.txt',Syy[:,tfr:])
113 np.savetxt(cwd + '\\Szz.txt',Szz[:,tfr:])
114 np.savetxt(cwd + '\\Sxy.txt',Sxy[:,tfr:])
115 np.savetxt(cwd + '\\Pos.txt',POS)
```

Matlab code to define hotspot

```
1 %% Code to compute SWT from elements extract from ABAQUS .odb
2 % Author: Danilo Rangel de Sousa Resende
3 % Mechanical Engineer and Master student UnB
4 % 2023
5
6 clear;clc;close all;
7
8 %% Import stresses from .txts
```

```
time(1) = 0;
time(2:33) = table2array(readtable('Time.txt'));
Sxx = table2array(readtable('Sxx.txt'));
Syy = table2array(readtable('Syy.txt'));
Szz = table2array(readtable('Szz.txt'));
Sxy = table2array(readtable('Sxy.txt'));
Pos = table2array(readtable('Pos.txt'));
x = Pos(:,1);
y = Pos(:,2);
E = 68800;
%% Vector and tensor alocation
discretization = 1;
phi = 90; % set to only 90 as this is 2D compute and n is always over xy plane
theta = 0:discretization:179; % critical point depends only on theta
S = zeros(3,3,length(Pos(:,1)),length(time)); % Tensor 3x3 (elem,t)
Sn = zeros(1,length(time));
SWT = zeros(1,length(Pos(:,1)));
phi_swt = zeros(1,length(Pos(:,1)));
theta_swt = zeros(1,length(Pos(:,1)));
zero = zeros(1,33);
tic
%% Loops to calculate stress tensor and SWT
surf_points_dist = length(y)/length(find(y==max(y))); % only compute surface points

for elem = 1:surf_points_dist:length(x)
    for i_the = 1:length(theta)
        for i_phi = 1:length(phi)

            % vector n normal
            nx = sind(phi(i_phi))*cosd(theta(i_the));
            ny = sind(phi(i_phi))*sind(theta(i_the));
            nz = cosd(phi(i_phi));
            n = [nx ny nz]';

            for t = 1:length(time)

                S(:,:,elem,t) = [Sxx(elem,t) Sxy(elem,t) 0;
                                 Sxy(elem,t) Syy(elem,t) 0;
                                 0           0           Szz(elem,t)];

                Sn(t) = dot(S(:,:,elem,t)*n,n);

            end

            % SWT computation
            SWT_teste = (max(Sn) - min(Sn))/2/E * max(Sn);

```

```
            % Condition to have the max SWT of a element.
            if SWT_teste>SWT(elem)
                SWT(elem) = SWT_teste;
                phi_swt(elem) = phi(i_phi);
                theta_swt(elem) = theta(i_the);
            else
            end
        end
    end
    disp(elem)

end

[SWT_max, SWT_index] = max(SWT);
hotspot = Pos(SWT_index,:) % Defines what of all elements has the max SWT parameter


toc
```

Matlab code compute iterative line method

```
    %% Code to compute TCL variable line method from elements extract from ABAQUS .odb
% Author: Danilo Rangel de Sousa Resende
% Mechanical Engineer and Master student UnB
% 2023
tic

% Assignment of the constants of L-Nf curve
Ls = 662e-3;
Lhcf = 19.5e-3;
B = log(Lhcf/Ls)/log(10^6);

Lmin = Lhcf; % L max of the methodology
Lmax = Ls; % L min min of the methodology

stop = 0;
while stop == 0
    Lg = (Lmin+Lmax)/2; % First guess
    L2 = 2*Lg;

    L_array = linspace(0,L2,40); % Discretization of the line length


    hotspot = Pos(SWT_index,:); % hotspot determined by running MAIN_SWT_2D
    theta_line= 0:1:15; % Possible line inclinations
```

```
25
26      % Vector alocation
27      Sn_line = zeros(1,length(L_array));
28      Sn_mean_line = zeros(1,length(time));
29      SWT_line = 0;
30
31      for i_theta = 1:length(theta_line) % Theta loop
32          x_line = hotspot(1)-sind(theta_line(i_theta)).*L_array;
33          y_line = hotspot(2)-cosd(theta_line(i_theta)).*L_array;
34
35
36          for i_time = 1:length(time) % time loop
37
38              % Use of grid data to analise stress at any point given a data
39              % field from FEM analysis.
40              Sxx_line = griddata(x,y,Sxx(:,i_time),x_line,y_line,'natural');
41              Syy_line = griddata(x,y,Syy(:,i_time),x_line,y_line,'natural');
42              Szz_line = griddata(x,y,Szz(:,i_time),x_line,y_line,'natural');
43              Sxy_line = griddata(x,y,Sxy(:,i_time),x_line,y_line,'natural');
44
45              % Assingment of normal vector
46                  nx = sind(90)*cosd(-theta_line(i_theta));
47                  ny = sind(90)*sind(-theta_line(i_theta));
48                  nz = cosd(90);
49                  n = [nx ny nz]';
50
51              % Calculating the stress along all point of the line
52              for cont = 1:length(x_line)
53                  Sn_line(cont) = dot([  Sxx_line(cont) Sxy_line(cont) 0;...
54                                         Sxy_line(cont) Syy_line(cont) 0;...
55                                         0              0              Szz_line(cont)]*n,n);
56              end
57          % Taking the average normal stress along the line
58          % Sn_mean_line(i_time) = mean(Sn_line);
59          Sn_mean_line(i_time) = 1/L2*trapz(L_array,Sn_line);
60
61          end
62
63          % Calculating SWT_line
64          SWT_teste =  (max(Sn_mean_line) - min(Sn_mean_line))/2/E * max(Sn_mean_line);
65
66          % Condition to test if the given theta has the higher SWT
67          if SWT_teste>SWT_line
68              SWT_line = SWT_teste;
69              theta_swt_line = theta_line(i_theta);
70          end
71      end
```

```
    % calculate life from SWT, returns N_final
    % Life from Basquin-Cofin-Mason Eq
    % Coefficients
    Sig_f = 1231;
    Eps_f = 0.2634;
    b = -0.122;
    c = -0.806;
    E = 68800; % Elasticity modulus

    % Solving equation
    syms N
    eq = SWT_line == Sig_f^2/E*(2*N)^(2*b)+Sig_f*Eps_f*(2*N)^(b+c);

    N_final = vpasolve(eq,N);
    N_final = round(double(N_final))

    Lcomp = Ls*(N_final)^B % Gives the L comparison from L-N_f curve


    % Condition to check is L comp and Lg are sufficiently close
    if Lcomp >= 0.99*Lg && Lcomp<=1.01*Lg
        stop = 1
    elseif Lcomp>Lg
        Lmin = Lg; % Updates Lg by bissection method
    else
        Lmax=Lg; % Updates Lg by bissection method
    end

end
    toc
```

Technical Drawings

It follows the technical drawing of the fretting fatigue test specimen and pad used on this work, all machined of the aluminum alloy Al 7075-T651.

Microscopy results

After, it can also be seen the microscopy results for the contact surface measurements and for the crack and fracture surface measurements.

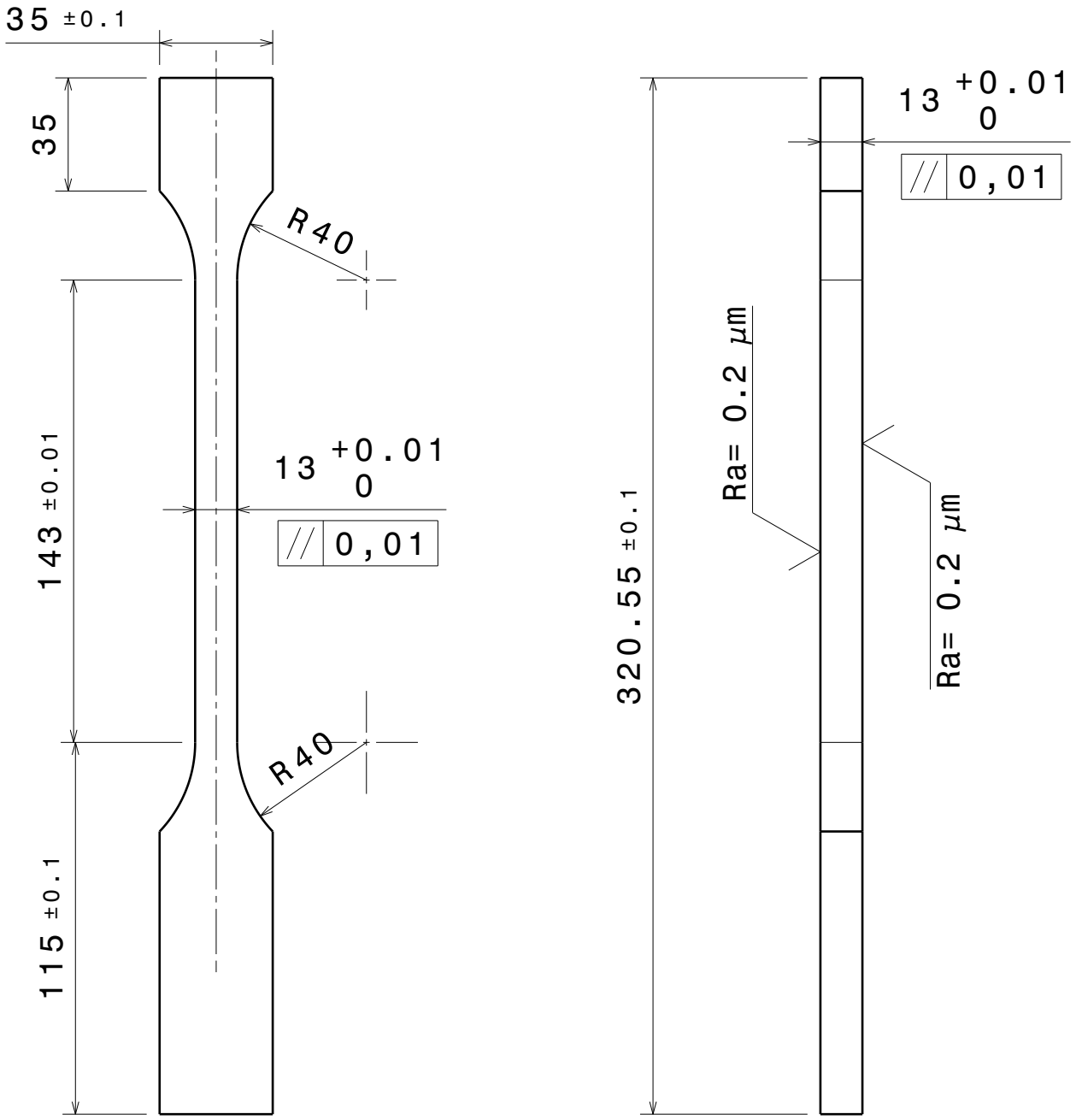

-	-	Fretting fatigue Specimen 13x13	Al-7075-T651	-	-
Item	Qde	Denominação	Material	Tratamento	Observações

UnB | Faculdade de Tecnologia-FT | Departamento de Engenharia Mecânica-ENM

Laboratório de Ensaios Mecânicos

Testes de Fadiga sob condições de Fretting

TOLERÂNCIAS GERAIS						ESCALA	DATA	DESENHISTA	COORDENADOR
Dimensões	Fêmea	Macho	Largura	Rosca	Angulos	1:2	09/01/24	Danilo	Prof. Alex
<30	+ 0,2 + 0	+ 0 - 0,2	± 0,1	6 H	± 15'	A3	UnB	1011A29	
>30	H13	h13	Js13	6 g					

Data	Tipo da revisão	Rev.

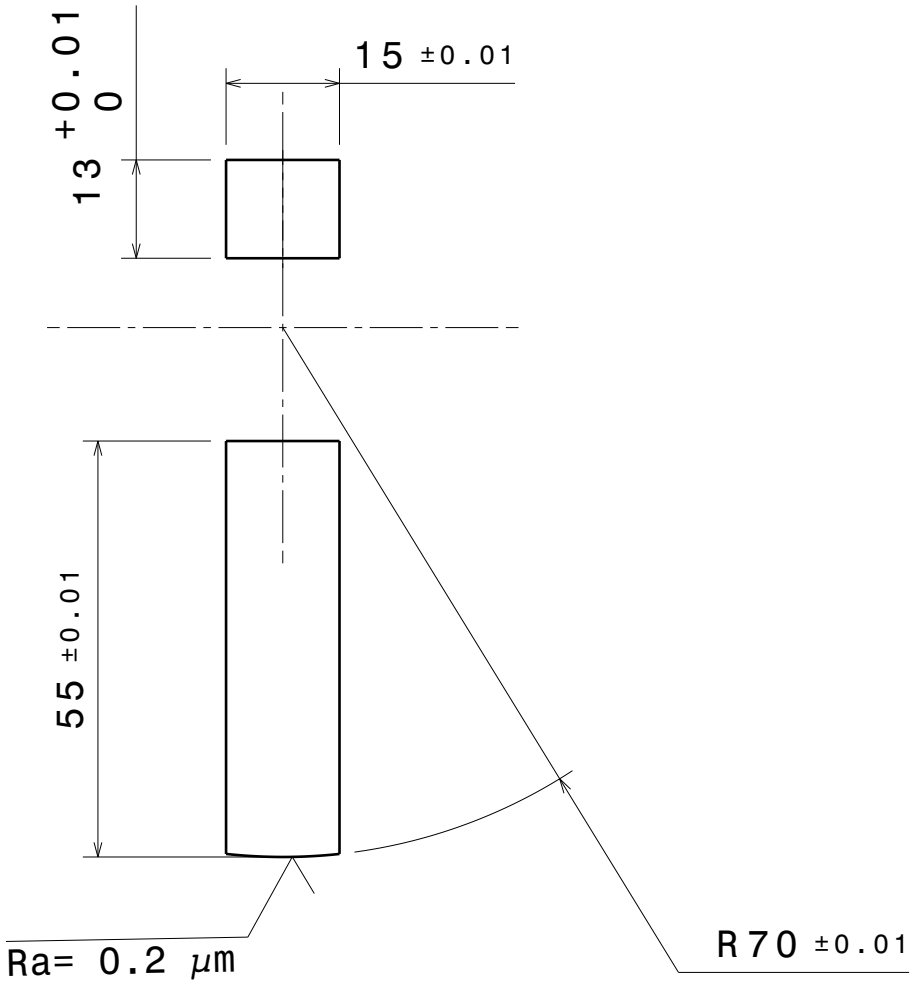

Item	Qde	Denominação	Material	Tratamento	Observações
31	-	Fretting Pad 13x15	Al 7075-T651	-	-

UnB | Faculdade de Tecnologia-FT | Departamento de Engenharia Mecânica-ENM

Laboratório de Ensaios Mecânicos

Testes de Fadiga sob condições de Fretting

TOLERÂNCIAS GERAIS						ESCALA	DATA	DESENHISTA	COORDENADOR
Dimensões	Fêmea	Macho	Largura	Rosca	Angulos	1:1	09/01/24	Danilo	Prof. Alex
<30	+ 0,2 + 0	+ 0 - 0,2	± 0,1	6 H	± 15'	A3	UnB	1011B29	
>30	H13	h13	Js13	6 g					

Contact surface - 5 mm

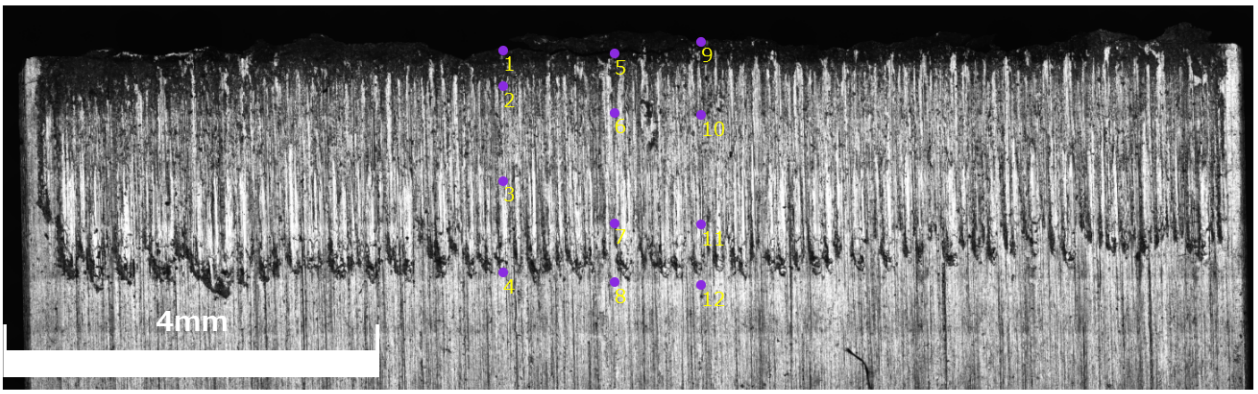

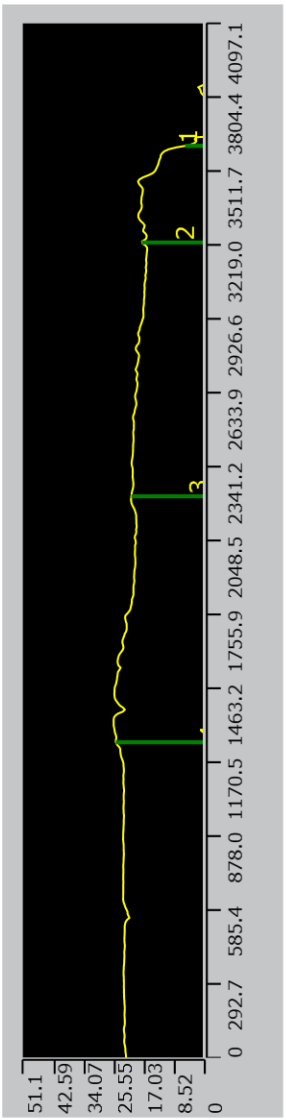

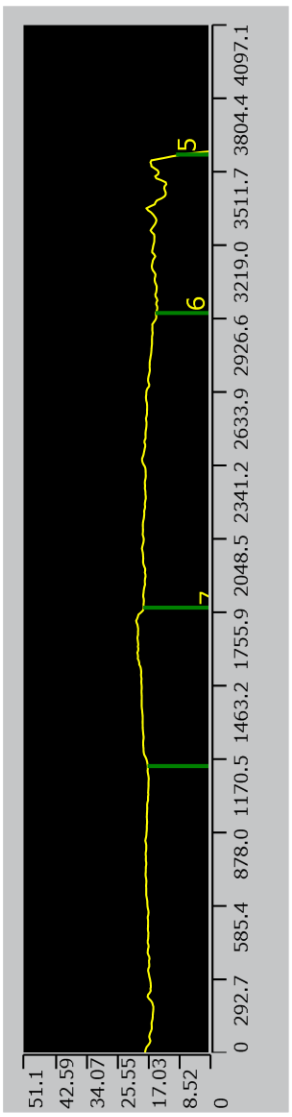

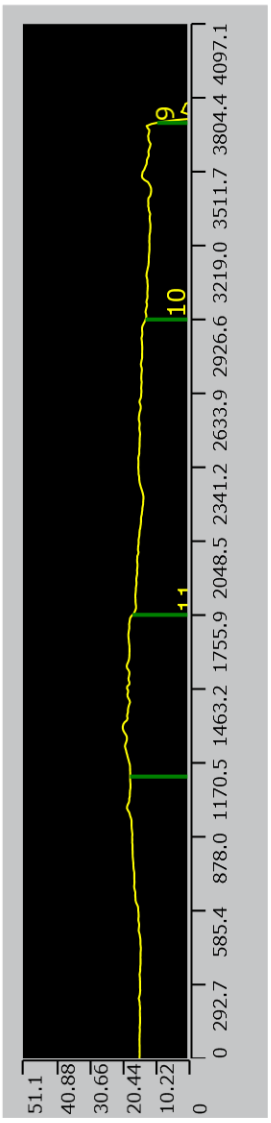

	No.	Result	Height[μm]	File name
☑	1		56.112	224749
☑	2		68.427	224749
☑	3		71.360	224749
☑	4		75.786	224749
☑	5		60.058	224749
☑	6		65.727	224749
☑	7		69.103	224749
☑	8		67.954	224749
☑	9		60.515	224749
☑	10		64.169	224749
☑	11		68.149	224749
☑	12		68.974	224749

Contact surface - 13 mm

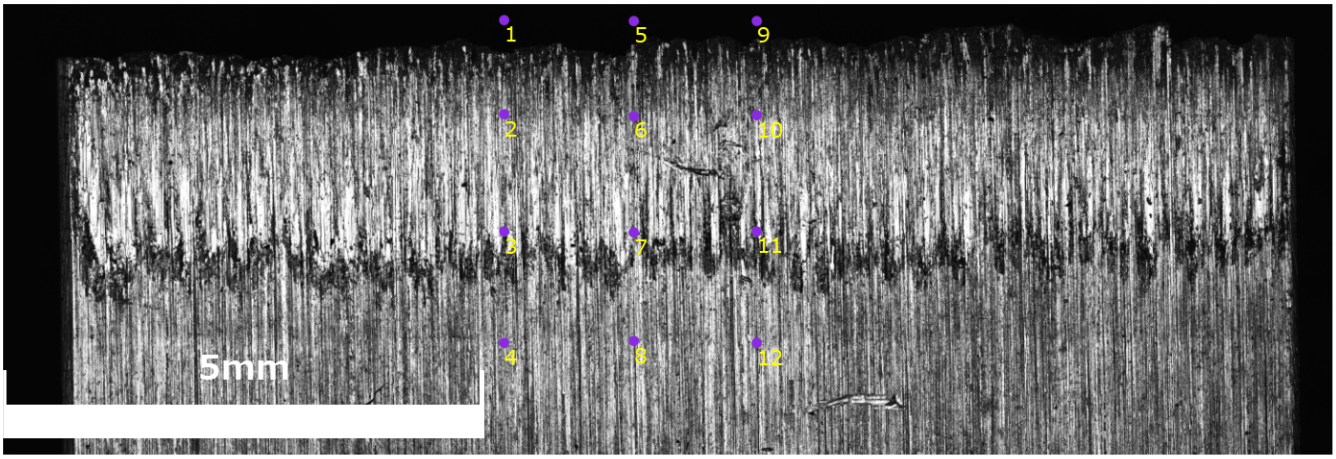

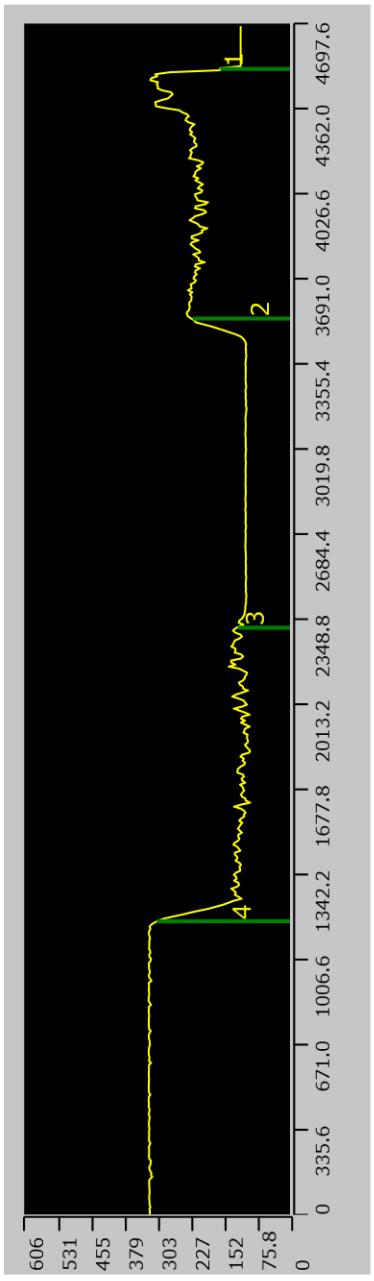

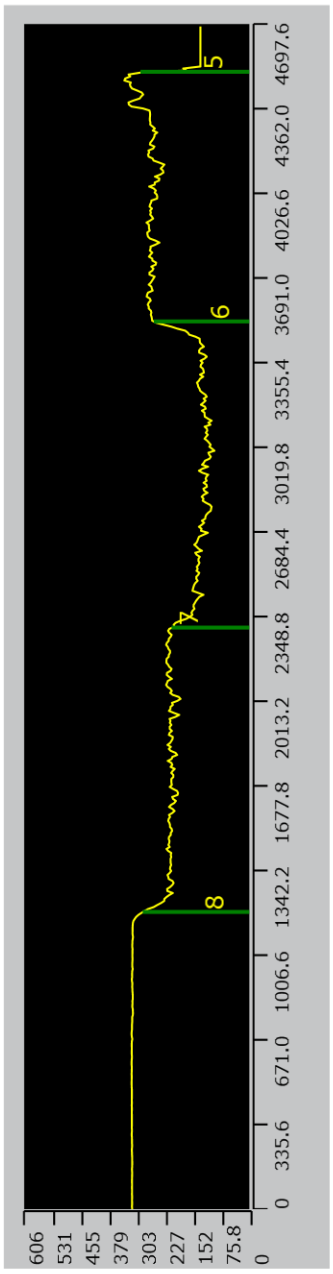

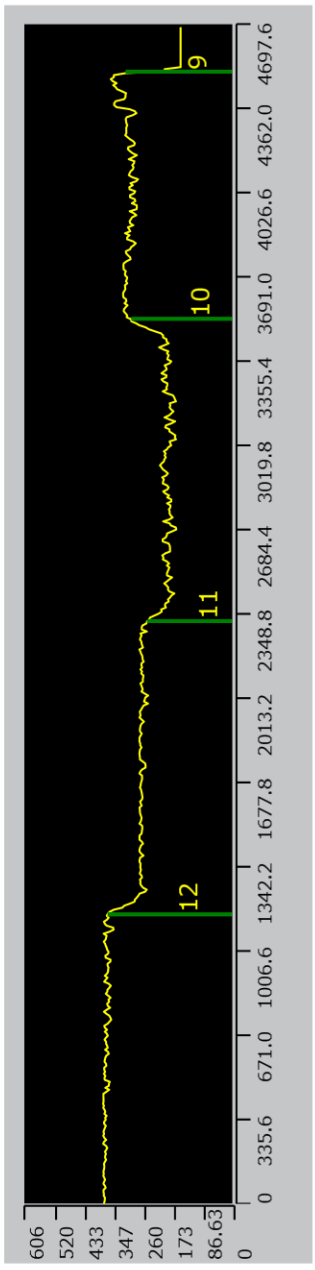

15-Apr-24

	No.	Result	Height[μm]	File name
☑	1		159.244	merge_240415_163813
☑	2		221.696	merge_240415_163813
☑	3		119.287	merge_240415_163813
☑	4		303.969	merge_240415_163813
☑	5		293.272	merge_240415_163813
☑	6		257.230	merge_240415_163813
☑	7		209.842	merge_240415_163813
☑	8		287.285	merge_240415_163813
☑	9		311.641	merge_240415_163813
☑	10		294.790	merge_240415_163813
☑	11		248.846	merge_240415_163813
☑	12		364.071	merge_240415_163813

Crack and fracture surface - 5 mm

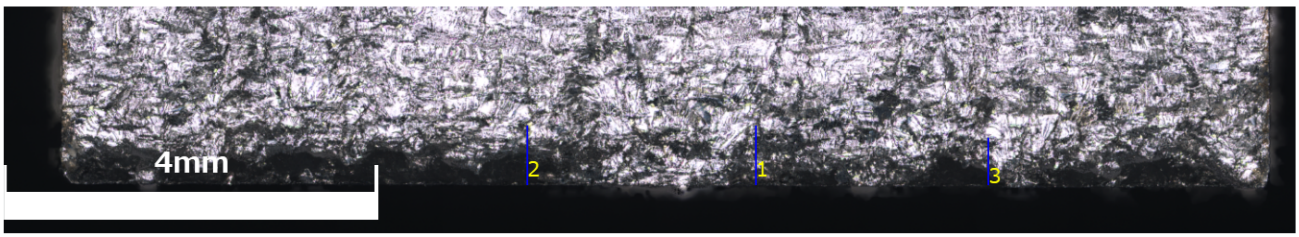

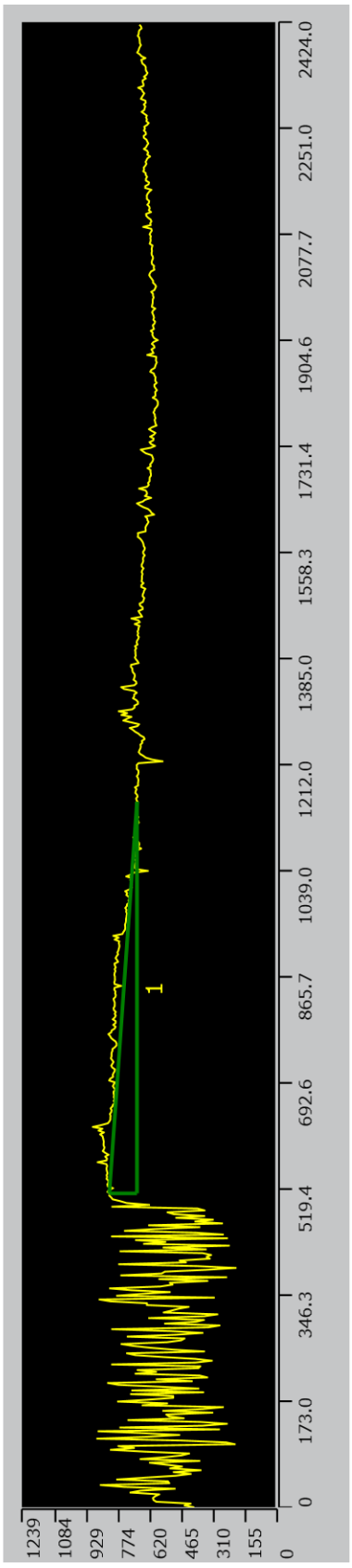

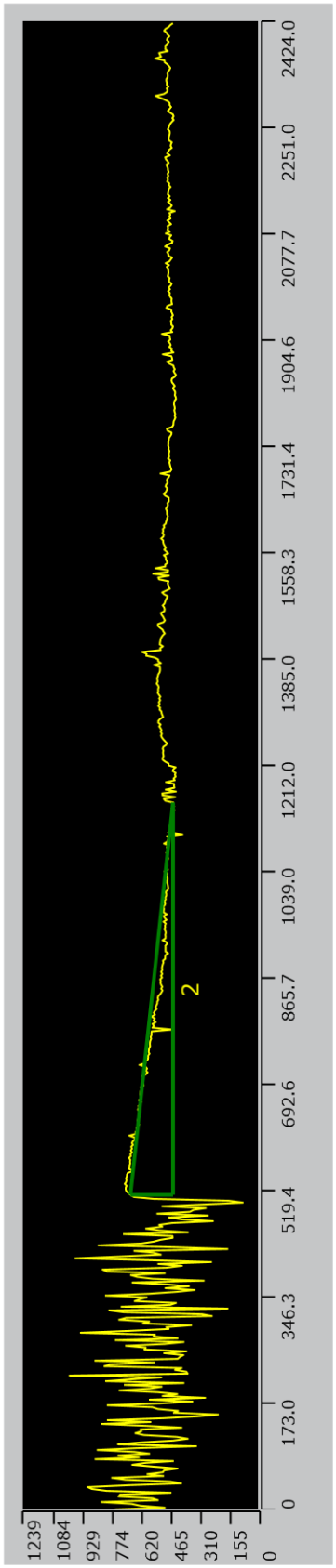

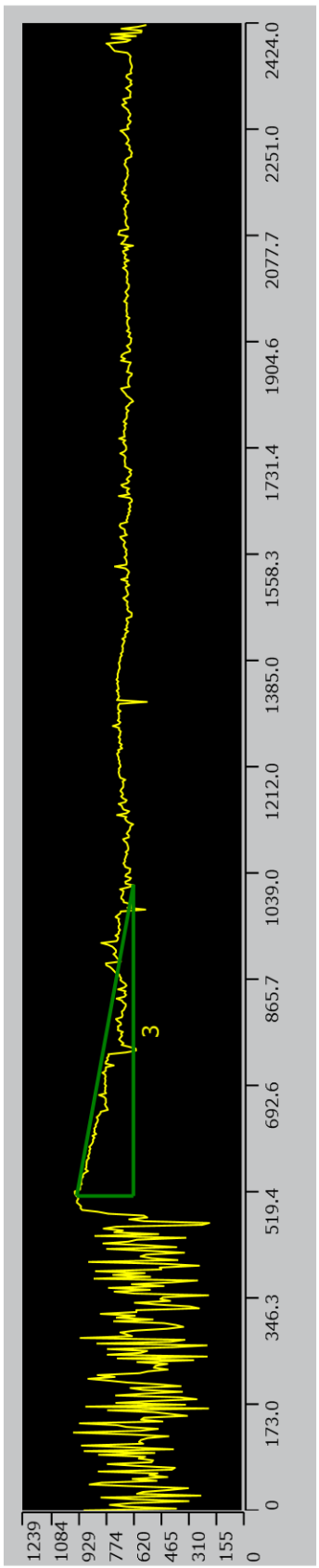

18-Apr-24

	No.	Result	Width[µm]	Height[µm]	Length[µm]	Angle[°]	File name
☑	1		638.400	135.275	652.575	11.964	dados_5mm_inici
☑	2		638.400	224.664	676.778	19.388	dados_5mm_inici
☑	3		506.400	319.933	598.997	32.284	dados_5mm_inici

Crack and fracture surface - 13 mm

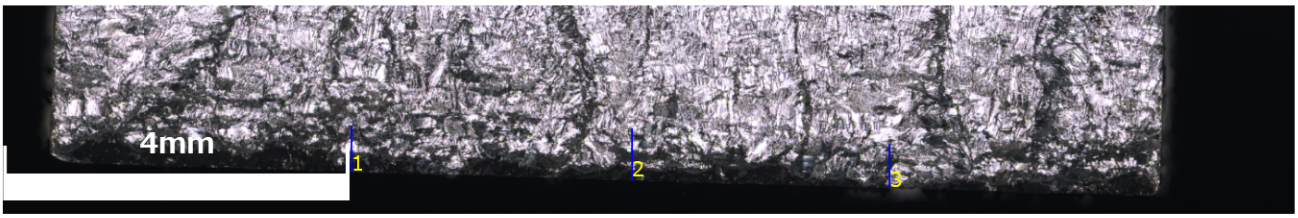

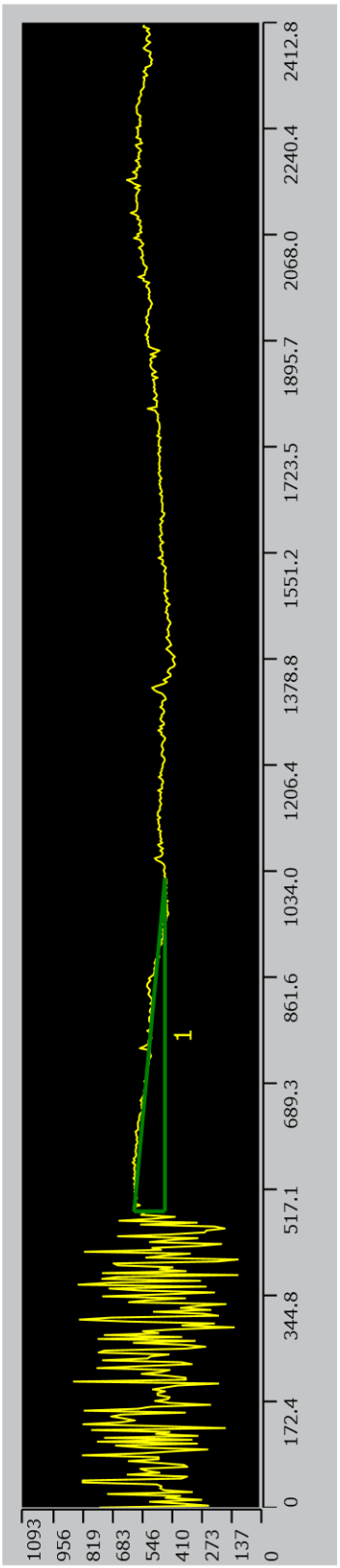

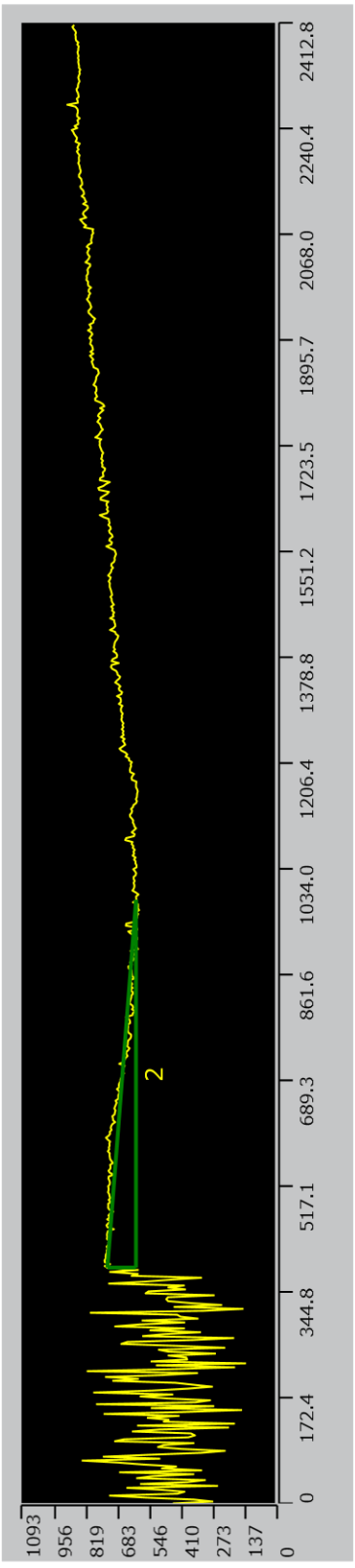

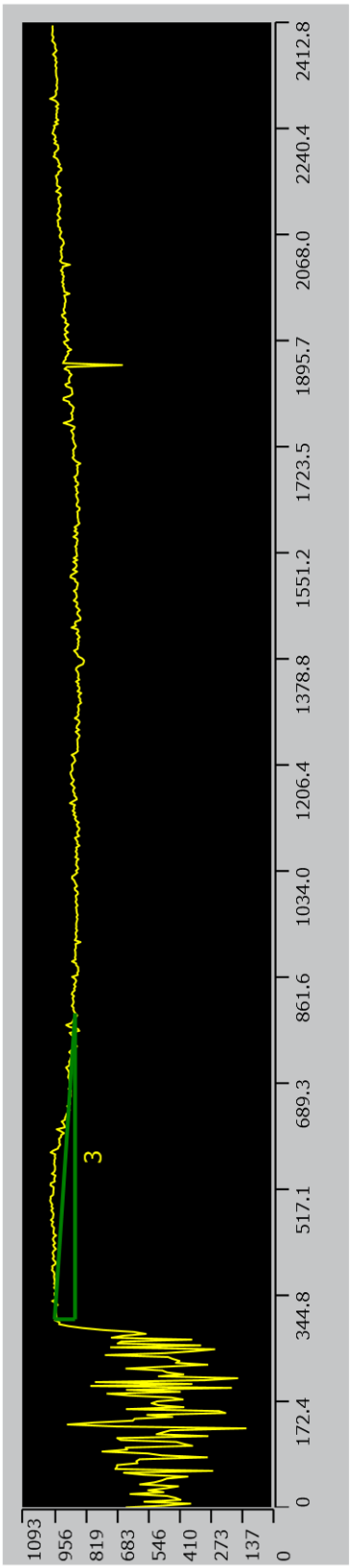

18-Apr-24

	No.	Result	Width[µm]	Height[µm]	Length[µm]	Angle[°]	File name
☑	1		540.800	141.735	559.065	14.686	dados_13mm_in
☑	2		600.600	123.497	613.165	11.619	dados_13mm_in
☑	3		496.600	89.722	504.640	10.241	dados_13mm_in